Technische Universität München
TUM School of Natural Sciences

Active Site Generation and Deactivation of the Air Electrode in High Temperature Solid Oxide Cells

Hanna Christine Türk

Vollständiger Abdruck der von der TUM School of Natural Sciences der Technischen Universität München zur Erlangung des akademischen Grades einer

Doktorin der Naturwissenschaften (Dr. rer. nat.)

genehmigten Dissertation.

Vorsitz: Priv.-Doz. Dr. Friedrich Esch

Prüfende der Dissertation:

1. Prof. Dr. Karsten Reuter
2. Prof. Dr. Johannes A. Lercher
3. Priv.-Doz. Dr. Jutta Rogal

Die Dissertation wurde am 13.10.2022 bei der Technischen Universität München eingereicht und durch die TUM School of Natural Sciences am 10.11.2022 angenommen.

$KHCO_3$

für Papa

Abstract

Electrode degradation currently limits the wide-spread commercial adoption of highly efficient solid oxide cell based energy storage systems. While the phenomenon has been reported and studied excessively, the structure of the active site of the relevant oxygen evolution reaction located at the triple phase boundary in electrolysis mode is elusive. This prevents the detailed analysis the actual degradation mechanism, which is crucial for the systematic development of mitigation and prevention strategies.

In this work, the fundamental structure of the triple phase boundary and its underlying complexion at the solid/solid interface are uncovered by physics based simulations. The simulations uncover a new deactivation pathway by cation segregation trough the complexion. The findings are supported by experimental data, whose analysis is aided by a newly developed, robust workflow to detect minute concentrational changes of electron microscope images. To enable the access to the active sites' electronic structure, three neural network based generative models for inverse material design are assessed and adequate metrics for model training and comparison developed.

Zusammenfassung

Die kommerzielle Verwendung von Festoxidzellen als hoch effektive Energiespeicher wird aktuell durch die schnelle Zersetzung der Luftelektrode limitiert. Trotz ausgiebiger Beobachtung und Beschreibung dieses Phänomens ist die relevante Struktur des aktiven Zentrums der Sauerstoffbildungsreaktion an der Dreiphasengrenze im Elektrolysebetrieb ungeklärt. Dies verhindert eine genaue Analyse des Zersetzungsmechanismus, welcher notwendig ist für die systematische Entwicklung einer Strategie zur Vermeidung dieser Deaktivierung.

Die fundamentale Struktur der Dreiphasengrenze sowie der ihr zugrundeliegenden Komplexion der Festkörpergrenzfläche werden in dieser Arbeit mit physikalischen Modellen simuliert. Es ergibt sich ein neuer Reaktionspfad für die Deaktivierung durch Kationensegregation durch die Komplexion. Diese Ergebnisse werden gestützt durch experimentelle Messungen, für deren Auswertung eine neue, robuste Methode entwickelt wird. Diese ermöglicht die Auflösung kleinster Konzentrationsunterschiede in den Elektronenmikroskopiebildern. Desweiteren werden, um Zugriff auf die Elektronenstruktur des aktiven Zentrum zu erhalten, drei generative Modelle basierend auf künstlichen neuronalen Netzen für inverses Materialdesign verglichen und eine passende Metrik für deren Training und Vergleich entwickelt.

Abbreviations

DFT density functional theory 2, 13–18

EC electrolysis cell 3
EDX energy-dispersive X-ray spectroscopy 2, 16, 29, 31, 37
EELS electron energy loss spectroscopy 2, 16, 29

FC fuel cell 3
FF force field 13, 17–19

GAN generative adversarial network 33, 37

HER hydrogen evolution reaction 3
HOR hydrogen oxidation reaction 3
HR-STEM high-resolution scanning transmission electron microscopy 2, 29
HT-SOC high temperature solid oxide cell 3, 6

IGF intergranular glassy films 11

LSM lanthanum strontium manganite 2, 29

MC Monte Carlo 2, 21–23, 28, 31
MD molecular dynamics 2, 19, 20, 24, 31
ML machine learning 24, 27
MSD mean square displacement 20

NMF non-negative matrix factorization 31
NN neural network 24, 25, 27

OER oxygen evolution reaction 3, 8, 28, 29
ORR oxygen reduction reaction 3

RL reinforcement learning 33

SAF surface amorphous film 11
SOC solid oxide cell 1–3, 5–8, 35, 37, 38
SOEC solid oxide electrolysis cell 8, 22
SOFC solid oxide fuel cell 8
STEM scanning transmission electron microscopy 29

TPB triple phase boundary 8, 29, 31

VAE variational autoencoder 33
VE valence electron 15

YSZ yttria stabilized zirconia 2, 6, 7, 29, 31

Contents

1. Introduction

The change of the world's climate induces high investments in renewable energy technologies as carbon free, alternative energy sources[1–3]. While from an environmental perspective the usage of such sustainable energy production is highly desirable, many renewable energy sources such as wind, solar or wave power plants have an intermittent energy production which is dependent on the environment. The resulting variability and limited predictability renders their energy production times hardly flexible, requiring dynamic energy consumption[4] and a balancing system for efficient mid-term energy storage, which is able to store excess energy in times of overproduction and feed back in times of energy deficiency[1,5]. At the moment, this balance between supply and demand is mostly provided by the combustion of conventional fuels or usage of nuclear power[6]. However, with increasing usage of renewable energy technologies a way for environmentally friendly energy storage is required.

Hydrogen made from electrolysis of water is a promising solution, as it can provide mid- and long-term chemical storage capacity[5,7]. Stored energy in the form of such produced green hydrogen can flexibly be converted back to electric energy in fuel cells in times of demand. This does not only offer the desperately needed solution for power grid stabilization, but can also help to increase the market value and investment in renewable energy sources[8], thus catalyzing the transition towards more sustainable energy sources. Furthermore, hydrogen can serve as direct alternative to conventional fuels because of its high energy contents, zero greenhouse gas emissions, and low environmental impacts[9]. Its wide-spread adoption offers the evolution towards a more hydrogen based economy[7,10,11], as is illustrated in Figure 1.

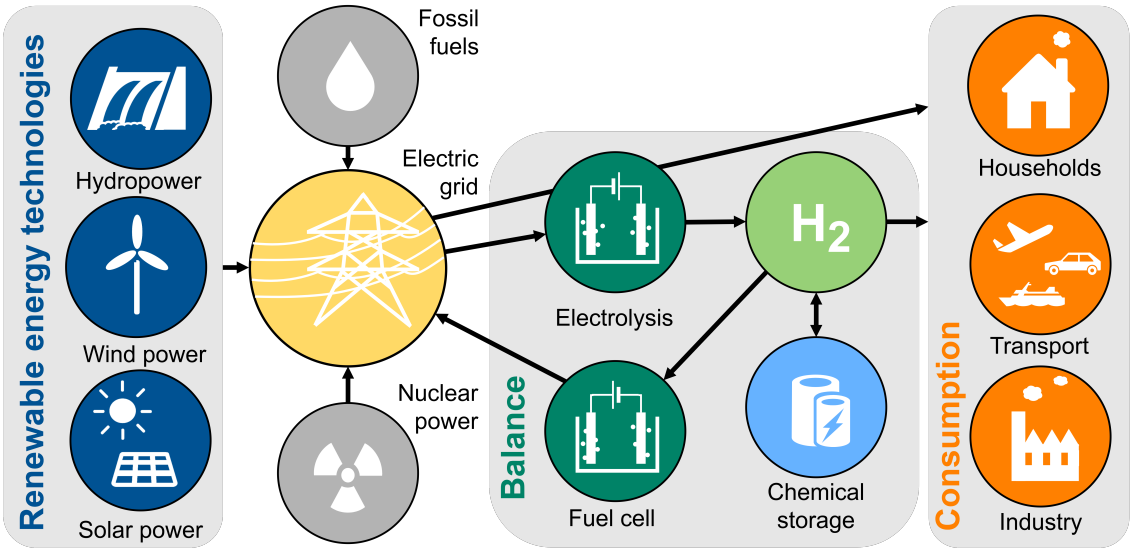

Figure 1 Scheme of a hydrogen based stabilization of the electrical grid.

Solid oxide cells (SOCs) are a promising candidate for reversible conversion of electrical power to hydrogen[12–15]. Their potential is based on the use of affordable raw materials[15], while showing low sensitivity to impurities in the fuel, good scalability, potential for dynamic

operation and high conversion efficiency[16,17]. In fact, their commonly high operating temperatures result in such favorable thermodynamics and reaction kinetics, that the cells yield an unrivaled efficiency for energy conversion[15,18].

However, their wide-spread adoption is still limited by the short lifetime of these electrochemical cells. Problematic is the fast degradation of the air electrode under electrolysis mode. Even though a plethora of deactivation mechanisms[19] and their mitigation[20] has been proposed, the performance of an operated cell continues to decrease faster than desired. This renders the use of SOCs still uneconomical. Understanding of processes on the atomistic level is necessary for successful identification and suppression of the problem[20–22].

In this work, the close collaboration of theoretical studies, employing density functional theory (DFT), molecular dynamics (MD) and Monte Carlo (MC) simulations, and high-resolution scanning transmission electron microscopy (HR-STEM) based experiments, including electron energy loss spectroscopy (EELS) and energy-dispersive X-ray spectroscopy (EDX), tackles the demystification of the air electrode's active region. For the first time, the fundamental structure of the interface between the common electrolyte yttria stabilized zirconia (YSZ, $(Y_2O_3)_{0.08}(ZrO_2)_{0.92}$) and the air electrode material lanthanum strontium manganite (LSM, $(La_{0.8}Sr_{0.2})_{0.95}MnO_{3-\delta}$) is elucidated at an atomistic level[23,24]. The discovered complexion[25,26] at the solid/solid interface reveals distinctly different properties from the surrounding bulk phases and opens a new design space to tune cell performance via interfacial engineering.

A subsequent investigation of a thermally aged electrode indicates the temporal stability and evolution of the complexion. For this, the limits of the spatial resolution of EDX are pushed to the sub-nano level, by detection of differences in mean concentrations with statistical Welch t-tests. Together with MD simulations along and across the complexion, a new cation segregation pathway within the cell is unveiled, which can explain several previous observations that accompany cell deactivation.

In order to make the complexion region accessible for electronic structure calculations, the performance of generative models is explored and compared in a comprehensive study of Elpasolite crystals. The findings do not only open the field of generating structure ensembles of small, periodic cells suitable for DFT calculations from larger simulation cells, but furthermore will enable inverse design of the complexion region in the future.

Before the major findings of the published papers are summarized, an overview of the theoretical concepts and employed methods is given.

2. Solid Oxide Cells

Solid oxide cells (SOCs) are among the most efficient technologies for reversible conversion of electrical power to fuel, commonly hydrogen, methane, syngas, or synthetic fuels[13–15,20,27]. The cells can be operated in two modes. In fuel cell (FC) mode, electrical energy is generated by oxidizing a fuel in two controlled half-reactions that are spatially separated on different electrodes. In electrolysis cell (EC) mode, fuel is generated from electrical power by applying an electric potential between the electrodes, which reduces the gas (commonly steam or steam/gas mixtures) fed into the cell.

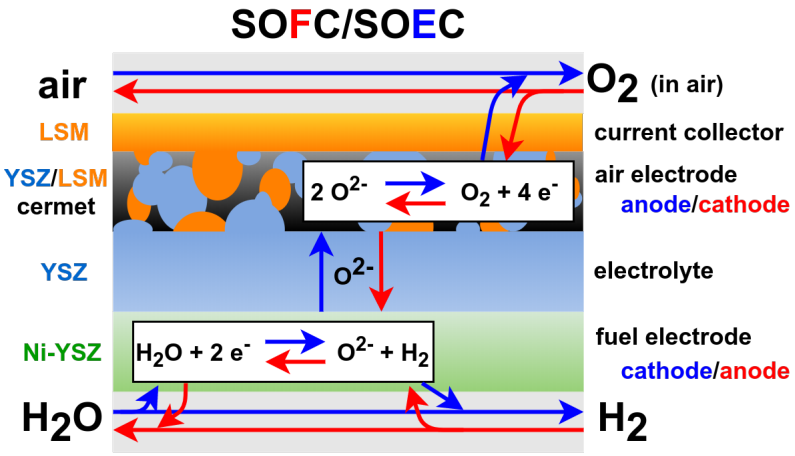

Figure 2 Scheme of the atomic transports and reactions in a planar solid oxide cell. Particle flow pathways and electrode classifications in fuel cell mode are given in red, for electrolysis mode in blue. Typical materials for the cell components are given on the left. Adapted from [23].

A schematic overview of a typical hydrogen SOC is shown in Figure 2. The gas-tight electrolyte is sandwiched between the two porous electrodes, which are connected to the gas channels that transport and supply reactants. For the two operation modes of the cell, fuel cell and electrolysis, particle flow and reaction directions are indicated with arrows of different colors. In fuel cell mode (red), electric energy is generated from fuel, here hydrogen, and oxygen. In this mode, a hydrogen oxidation reaction (HOR) takes place at the fuel electrode (anode), and an oxygen reduction reaction (ORR) at the air electrode (cathode).

In a solid oxide electrolysis cell (blue), water is split into its elemental components under an applied potential. Here, the reactions and ionic transport are taking place in opposite direction from the fuel cell mode, changing also the role of the respective electrodes. The hydrogen electrode takes the role of the cathode, hosting the reduction of protons to molecular hydrogen in the hydrogen evolution reaction (HER). At the air electrode, oxygen ions are oxidized in the oxygen evolution reaction (OER), thus making it the anode.

SOCs exist for intermediate (773–1073 K) and high temperature (1073-1273 K) operation[28]. Economically, especially high temperature solid oxide cells (HT-SOCs) are attractive as they reach energy conversion efficiencies of up to 65–85% in FC mode[18,20,29,30], and even better efficiency in EC mode as the electric energy to be stored can partially be compensated by

low-cost thermal energy[20]. The reason for this are benefits from favorable thermodynamics and reaction kinetics at elevated temperature[15], which result in lower overpotentials and thus a lower loss of power during conversion[31]. This is explained further in the following section.

2.1. Overpotentials

In an electrochemical cell, a reaction is spatially separated into two half-reactions, each at its own electrode. Differences in electrochemical potential between each of the two charge separating half-reactions thereby determines the obtainable electric potential from the entire reaction. The maximum electrical potential that can be generated in an electrochemical reaction is limited by the laws of thermodynamics[27], and defined by the magnitude of the difference of the electrochemical potential between the electrodes.

The electrochemical potential of an electrode is a reaction intrinsic property originating from the occurring charge separation. Standardized measurement and comparison of many electrochemical half-reactions against the standard hydrogen electrode enable easy access to the electrochemical potential between two electrodes via the electrochemical series. The potential difference obtained from this series yields the ideal thermodynamic potential E° between two electrodes based on their respective reactions under ideal conditions, i.e. without dilution effects or transport and kinetic limitations.

However, in reality, these cell limitations cause potential losses that lower the obtained usable potential. Any such variance of the cell potential from the thermodynamically feasible potential is called overpotential. Main causes for overpotentials in solid oxide cells are[27,32]

- activation losses, arising from the slow kinetics of the charge transfer reactions at the electrodes,
- diffusion losses, evoked by mass transport limitations of the reactants to the electrode active sites and
- ohmic losses, generated by the cell internal resistance due to its individual components and their contacts.

Hence, during cell operation, the cell voltage V obtained (FC mode) or needed (electrolysis mode) to drive the reaction is

$$V = E^\circ - iR - \eta_A - \eta_F \quad , \tag{2.1}$$

with the current i passing through the cell, the internal electric resistance R of the cell (resulting in ohmic loss) and the voltage losses η_A and η_F of air and fuel electrode. The voltage losses at the electrodes include the diffusion and activation losses, i.g. gas diffusion, ionic migration, gas/solid interactions, polarization, and kinetic losses[28]. As overpotentials cause the formation of heat instead of electric power and thus cause the loss of electric energy to less valuable thermal heat, it is desirable to minimize them as much as possible.

One mitigation possibility for overpotentials is based on careful cell design. This includes, besides the selection of materials with optimal properties for the desired task, cell engineering that reduces mass transport ways, e.g. optimized gas flow and thin electrolytes. Appropriate design choices can greatly reduce ohmic and diffusion losses[33].

Cell performance can further be optimized by the reduction of the activation loss. This loss is caused by the kinetics induced slowness of the reactions at the electrode surface in the presence of reacting species. Specifically, it arises from the charge transfer between the electrode and the electrolyte interfaces[32].

The influence of the activation overpotential η_{act} on the obtained electric current density j is described by the Butler–Volmer equation[32]

$$j = j_0 \left(\underbrace{e^{\alpha \frac{nF\eta_{\mathrm{act}}}{RT}}}_{j_1} - \underbrace{e^{-(1-\alpha)\frac{nF\eta_{\mathrm{act}}}{RT}}}_{j_2} \right) \quad . \tag{2.2}$$

Besides the activation overpotential η_{act}, the current density j is dependent on the exchange current density j_0, temperature T and the number of electrons n involved in the reaction[27]. F is the Faraday constant. The transfer coefficient α relates to the symmetry of the activation barrier.

From the Butler-Volmer equation it can be seen, that the obtained current density can be separated into two partial current densities, belonging to the forward (j_1) and reverse (j_2) reaction. The individual contributions of the two terms to the Butler-Volmer equation is illustrated in Figure 3a. It shows that a higher overpotential requires a higher current density, which directly translates to a higher loss of electric energy.

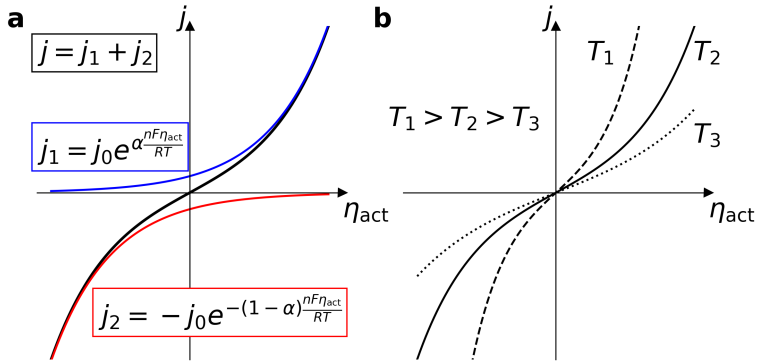

Figure 3 a) Contributions to the Butler-Volmer equation and resulting kinetics and b) the dependence of the current density j on temperature.

Figure 3b shows the influence of temperature on the relation between current density and activation overpotential. At higher temperature, a lower overpotential is required in order to drive the cell with the same current as a cell at decreased temperature. Reason for this is the higher probability to overcome the activation barrier of a system with higher temperature and thus thermal energy, which results in faster kinetics. Hence, the operation of SOCs at elevated temperatures increases the reaction rates at the electrodes and thus reduces the

overpotential required to obtain a certain current density[13]. Overall, this leads to a decrease of irreversible losses associated with ohmic resistance and activation overpotential[33,34]. The resulting higher conversion efficiency and lower loss of electrical power makes high temperature operation of SOCs desirable.

2.2. State-of-the-art Cell Components

High stability at high temperature and applied potentials is an essential requirement for all cell components. Additionally, depending on the specific task of the cell component, the materials have to fulfill further properties, e.g. necessary particle conductivity and catalytic activity for the respective reaction. The requirements of the individual cell components and an overview of the state-of-the-art materials is given in the following.

2.2.1. Electrolyte

The essential role of the electrolyte in a solid oxide cell is to spatially separate the two half-reactions occurring on the electrodes. At the same time, it provides a connection between the two half-reactions, by conducting the produced oxygen ions from the active site of one electrode to the other electrode's, where it is the educt for the other half-reaction. A high ion conductivity between the electrodes is desired, as it results in a lower ohmic overpotential for ion transport through this cell component. Thus, this property is crucial for cell performance. In general, this ohmic loss is lowered by making the electrolyte layer as thin as possible while still preventing short circuiting[12].
Besides the functional necessity of ion conduction, materials for the electrolyte have to fulfill three other requirements. Next to being dense and gas-tight, so that no gases can diffuse between the different electrode gas channels, a low electronic conductivity is required to suppress short circuiting. Furthermore, long term chemical stability at the cell operating temperature is desirable, as well as at the highly oxidizing and reducing conditions, which the electrolyte is exposed to on the sides of the electrodes[12,28].
State-of-the-art for the electrolyte is yttria stabilized zirconia (YSZ), which is the only known material that sufficiently balances these electrical, thermal, and mechanical requirements at elevated temperatures[20]. This material has different properties and applications depending on the amount of yttria doping. With 4 mol. % yttria doping (4YSZ, or often also confusingly denoted 8% $YO_{1.5}$), it is an excellent thermal insulator used for thermal barrier coatings for aircraft engines and land-based gas turbines[35,36]. Around 8 mol. % doping of yttria (8YSZ), the oxygen ion conductivity of the material peaks[37–40], making it the optimal amount of doping for the SOC electrolyte application. Despite its comparably low oxygen ion conductivity in comparison to other materials, its availability, low electronic conductivity and stability under SOC reaction conditions makes it undisputably the electrolyte of choice for HT-SOCs[12].

2.2.2. Fuel Electrode

Necessary requirements for the fuel electrode are high porosity to allow sufficient gas diffusion, a similar thermal expansion coefficient as the electrolyte for mechanical stability under dynamic operation and high stability at the cell operation temperature and the required applied potentials.
Good catalytic properties can be found in most noble metals, of which Ni offers a relatively cheap option with high catalytic activity[12]. Initial problems with this fuel electrode material, e.g. the higher thermal expansion coefficient and a coarsening of the microstructure due to metal aggregation through grain growth, have been mitigated by sintering a Ni-YSZ composite[12,28]. This advance made it the most common material for fuel electrodes[41,42].

2.2.3. Air Electrode

The air electrode is currently the Achilles' heel of SOCs, as it gradually deactivates during cell operation in electrolysis mode. A wide variety of electrode materials have been proposed[43], however, each having their own drawbacks and degradation problems. As for the fuel electrode, the requirements for the air electrode are a porous material with matching thermal expansion coefficient to the electrolyte and stability at cell operation conditions.
These properties are present in many different types of doped and double perovskite oxides[43]. Proposed materials include (among others) manganites, ferrites, cobaltites, cuprites, titanite, molybdenites and their mixtures, e.g. $La_{1-x}Sr_xMnO_{3-\delta}$ (LSM)[20,44], $La_{1-x}Sr_xCo_{1-y}Fe_yO_{3-\delta}$ (LSCF)[12,45],$SrTi_{1-x}Fe_xO_{3-\delta}$ (STF)[46,47], $SrFe_{1-y}Mo_yO_{3-\delta}$ (SFM)[48], $PrBa_{0.8}Ca_{0.2}Co_2O_{5-\delta}$ (PBCC)[49], $La_{1-x}Sr_xGa_yNi_{1-y}O_{3-\delta}$ (LSGN)[50], and $La_{1-x}Sr_xCu_{1-y}Fe_yO_{3-\delta}$ (LSCuF)[51].
However, the compliance of the requirements and catalytic activity vary depending on doping concentrations and cell operating conditions. Furthermore, some of these perovskites react with the electrolyte material YSZ, requiring a protective coating between the electrode and the electrolyte[20].
For high temperature applications, YSZ/LSM ceramic/metal (cermet) composite is the state-of-the-art material, as it features high electronic conductivity and similar thermal expansion coefficient as YSZ and does not require a protective coating[19,52–54].

2.3. Lifetime Limitations

High temperature operation of SOCs is preferable, as it yields very high energy conversion efficiency, due to the low overpotential losses evoked. However, at high temperature, cell deactivation over time due to material degradation becomes a severe problem[13,20,55], drastically limiting the lifetime and thus economic viability of the cells.
It has been estimated, that in order to sufficiently compensate material and fabrication cost, the operation time of a solid oxide cell stack should be at least five to eight years[56,57]. This translates to a cell stack lifetime of at least 40,000 h, corresponding to a cell degradation rate

lower than 0.5% per 1000 h of operation. While SOFC are already quite close to this goal with a degradation rate of 0.5-0.6% per 1000 h[44,58], operation in electrolysis mode is vastly limited. High temperature SOECs have a lifetime of the cells to about 2,000-5,000 h[28,59], translating to about 2% performance loss per 1000 h at best.

Cell lifetime has been shown to increase, when the cell operation alternates between the two modes[19,60–62]. However, even then electrode delamination was observed, and degradation in electrolysis mode is generally recognized to be irreversible[14]. In order to prevent this deactivation and thus extend the lifespan of the cells, an understanding of the fundamental reactions and the atomic structures in a SOC, its components and active sites is necessary[20].

For SOECs, cell deactivation has been reported to be caused by degradation of the fuel electrode (cathode)[21,53,56,59,63,64], mainly caused by nickel agglomeration and poisoning, and the electrolyte[56,59], due to side reactions and restructuring.

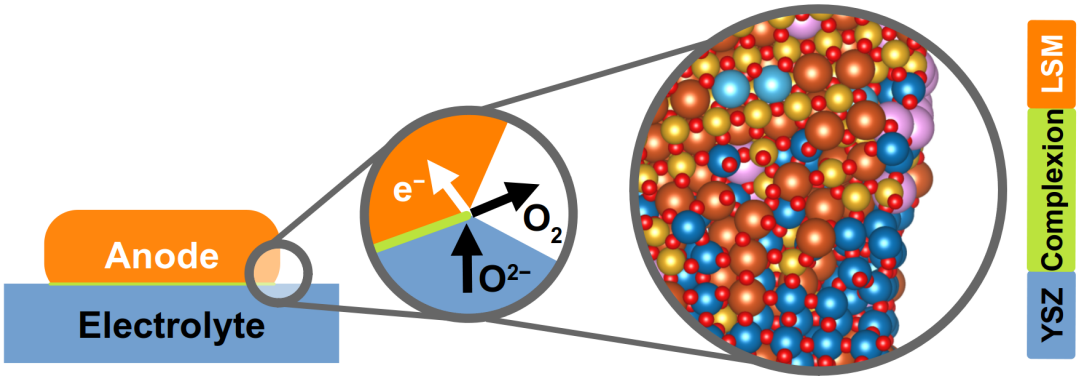

Figure 4 Scheme of the triple phase boundary located at the interface of electrolyte, anode and gas phase in SOECs. The particle flow in the respective phases is illustrated for the OER. Its atomic structure was obtained from simulation.

However, the undisputed main reason for the severe lifetime restrictions of SOECs is the degradation of the air electrode (anode). The active site of this electrode is at the triple phase boundary (TPB), where electrolyte, electrode and gas phase meet. Figure 4 illustrates the position of the TPB and the reactant flow during the OER. On the right, an atomistic view of the TPB and the classification of the regions obtained from simulations during this work is given.

In general, it is known that SOCs feature higher losses under anodic polarization compared to the cathodic polarization mode[62,65]. Reason for this are ionic and electronic transfer bottlenecks arising from compositional or structural inhomogeneities, which have been found to lead to potential jumps. In electrolysis mode, these potential jumps do not only amplify the occurring overpotentials for the OER, but furthermore lead to very localized extreme potentials[66].

Thus, faster degradation under anodic polarization is not surprising. However, in order to extend the lifetime of the cells as much as possible, the arising deactivation effects have to be mitigated as much as possible. Multiple mechanisms for the degradation of the TPB have been proposed, which for YSZ/LSM cermets include[19,43]

- microstructural coarsening

        - nanocluster formation of e.g. LSM, which leads to weakening of the YSZ/LSM contact[62,67]

- changes in surface chemistry
    - cation segregation (Sr and Mn)[20]
- reactions between phases
    - formation of electrically insulating layers of $La_2Zr_2O_7$ and $SrZrO_3$ at the contact region, which are known to form when sintering the two materials at high temperature[20,63,68–72]
- delamination
    - high internal oxygen partial pressure under anodic potential[13,73–75] leading to blasting of the contact between the two materials and thus loss of catalytically active regions
- active site poisoning
    - reactions of segregated cations with volatile surface components such as Cr, S and B agglomerating as inert species on the active site[20] and
    - spatial active site blockage by overgrowth with secondary phases[55,76].

While the exact reason for cell deactivation is unknown and might even include coaction of multiple of these processes, it is worth noting that cation surface segregation is related to many of the proposed deactivation causes. Cation migration can partly be prevented by A-site nonstoichiometry, which has been shown to mitigate the formation of secondary phases[77–79]. Furthermore, specific anode and microstructure design[80,81], as well as infiltration with nanoparticles[82] have been proposed to prevent high oxygen partial pressure[54] and anodic polarization[83], which are believed to cause further segregation. Even though these mitigation strategies have shown promising results, the underlying atomistic mechanism is nevertheless elusive. Elucidation of this process has been termed crucial, as knowledge of the mechanism enables the design and development of more targeted mitigation strategies[20].

3. Solid/Solid Interfaces and Complexions

Solid/solid interfaces play a major role for the properties of many solids, as the internal grain boundaries influence chemical and electrochemical stability, electron conductivity and enhance or inhibit ion diffusion. They thus critically define a material's performance and functionality, as well as its behavior in chemical reactions and catalysis[84–86].

The detailed form of a specific interface is often highly complex and its properties are therefore strongly dependent on the material, its crystal structure, doping, surface orientation and treatment. Especially for solid/solid interfaces, a great variety of interfacial models and interpretations exist, reaching from crystalline solid solutions[87] via relatively crystalline interfaces with subgrain boundaries[88] to rather amorphous intergranular glassy films (IGFs)[86] and surface amorphous films (SAFs)[26]. As many non-crystalline, 2-D interfaces are characterized by common compositional properties, the latter two have been unified under the term complexion[25,89].

Complexions are neither fully crystalline nor amorphous and thus exhibit compositions and thermodynamic stability differing from the crystal bulk. Furthermore, they feature distinct structural and compositional gradients, as well as a self-limiting equilibrium thickness of about 1 nm, as they are stabilized by the confining bulk phases and thus thermodynamically-limited. This means also, that complexions cannot be isolated, as they are not 3-D stable[26].

These characteristics yield very different local properties compared to the bulk phases of the respective materials. Changes in microscopic properties such as amorphization and lower density lead to distinctly different chemical environments compared to the bulk. These can severely influence a materials macroscopic properties, such as the stability of the material and its electronic and ionic conductivity.

Dillon and Harmer[25] proposed the classification of complexions into six different categories, depending on the numbers of atomic layers they span and their kinetic behavior. They proposed the creation of complexion diagrams, which analogous to a phase diagram show the state of a complexion for a material depending on doping and temperature. Besides these two points, the thickness of a complexion can be influenced by the crystal structure, pressure, crystal orientations (lattice mismatch), material pretreatment and impurities[26], and varies from one material to the next. Nevertheless, as stated before, the macroscopic properties of a material depend much on the thickness and form of its comprised complexions, making their assessment of high interest.

The concept of complexions is not limited to grain boundaries between solids; they have also been found for crystal terminations bordering other phases, which have undergone surface reconstruction[90]. For active surfaces, the understanding of such surface reconstructions is essential, as the formed complexion can alter the form of the reactive site and thus the reaction mechanism.

In practice, the occurrence of a complexion enables vast possibilities for material property design due to their multifaceted forms and characteristics dependent on environmental and

preparation conditions. This offers many adjustment prospects of their structural and therewith physical properties via interfacial engineering, e.g. by material pretreatement, sinter protocol, material doping and coatings[26,89].

4. Theoretical Description of the Atomic Scale

All information of a particular state of any chemical system can be fully described by its wave function[91]. The wave function Ψ is thus a central quantity in conventional quantum chemistry. From the wave function, every measurable observable can be calculated by its corresponding operator $\hat{F}$. For the energy E, this operator is called Hamiltonian $\hat{H}$, giving the famous Schrödinger equation

$$H\Psi = E\Psi \quad . \tag{4.1}$$

For a many-body system, the Hamiltonian takes the energy of all particles and their interactions into account. For a multi-atom system, the relevant energy contributions are the kinetic energy of the electrons T_e and nuclei T_n, as well as all electron-electron V_ee, nucleus-nucleus V_nn and nucleus-electron V_ne interactions.

$$\hat{H} = \hat{T}_\mathrm{e} + \hat{T}_\mathrm{n} + \hat{V}_\mathrm{ee} + \hat{V}_\mathrm{nn} + \hat{V}_\mathrm{ne} \tag{4.2}$$

This formula can be simplified by application of the Born-Oppenheimer approximation, which rests on the insight that the heavy nuclei move so much slower compared to the electrons, that their potential acting on the electrons can be considered fixed. Hence, the kinetic energy of the nuclei can be approximated to be zero and the interaction of the nuclei with each other to be constant, and thus negligible when dealing with energy differences (as is the case in computational chemistry). This renders the non-relativistic electronic Hamiltonian $\hat{H}_\mathrm{el}$

$$\hat{H}_\mathrm{el} = \hat{T}_\mathrm{e} + \hat{V}_\mathrm{ee} + \hat{V}_\mathrm{ne} \quad . \tag{4.3}$$

The complexity of the evaluation of the electronic Hamiltonian depends, due to the presence of pair-wise interaction terms, on the number of particles in the system which is included in the systems wave function. However, the wave function is an experimentally non-measurable, complex quantity depending on $4N$ variables, consisting of three spatial and one spin variable for each of the N electrons[91]. This makes assessment of properties of many-body systems highly complex, if not impossible.

In computational chemistry, a variety of wave function-based methods that aim to simplify the problem exist, which approximate the wave function more or less accurately e.g. Hartree-Fock, Møller-Plesset pertubation theory and Coupled Cluster expansion[92].

However, the either low accuracy or high computational cost and complexity of wave function based methods provoked the rise of alternative, cheaper approaches to describe chemical systems. In the following, a short introduction of the basic concepts of the two methods employed in this work, density functional theory (DFT) and force fields (FFs), is given. Both methods are commonly used in modern computational chemistry, for a more detailed description of DFT and FFs, refer to [91–93] and [94].

4.1. Density Functional Theory

In density functional theory, the central quantity that describes the target system is the electron density $\rho(\vec{r})$, which captures the probability to find an electron at the relevant position $\vec{r}$. It is a real, experimentally measurable quantity and its sole dependence on the position in space reduces the variable space to three, making it a much easier and cheaper accessible quantity than the wave function.

The electron density was established as a basic variable by Hohenberg and Kohn with two famous theorems[95]. The first proves that the ground state electron density uniquely defines a system's external potential (except for an additive constant), and thus its Hamiltonian operator and all system properties. The second Hohenberg-Kohn theorem states that only the exact ground state density delivers the minimum of the total energy and thus, this ground state density and energy can be obtained variationally from the trial density ρ_{trial} with the energy functional E_v[91]

$$E_v[\rho_{\mathrm{trial}}] \geq E_0 \quad . \tag{4.4}$$

Note, that the functional is thereby dependent on the external potential v induced by the trial electron density.

By this means, the electron density can provide the exact solution to any system, as long as the exact functional is used. However, the exact energy functional for the electron density is unknown and thus renders the approximation of accurate functionals the greatest challenge in DFT.

A partial solution to this problem was proposed by Kohn and Sham[96], rendering DFT the fruitful computational tool it is today. They proposed approximations of the two unknown functionals originating from the electron-electron interaction and the electron kinetic energy. The first is approximated by a classical Coulomb repulsion and the latter is estimated with a fictive, reference system of non-interacting electrons. Both approaches neglect correlated electron movement and the fermionic nature of electrons.

Nevertheless, these simplifications allow for the approximation of the dominant part of both energy contributions, with only a small part of the energy being uncertain, termed exchange-correlation energy. Unfortunately, even this small, missing energy contribution can be crucial for predictions that reach chemical accuracy. However, no universally valid form of the exchange-correlation functional has been found, yet. Hence, for the remaining, unknown energy many different approximations have been developed, which have been adjusted and tested to yield good results for certain chemical environments[91].

The usage of such environment-specific functionals allowed the application of DFT in all kinds of chemical systems and problems. Its versatility combined with its extremely high efficiency in predicting relatively accurate results, makes DFT one of the most popular methods in computational chemistry.

4.1.1. Excited States and Spectroscopy

DFT is widely used for the search of the global minimum of a structure's electron density and geometry, as the ground states provide valuable information on many properties of a system. However, the ground state is not accessible directly in spectroscopic experiments. Thus to validate predictions made with DFT and to provide data comparable with experiment, the description of excited states of a chemical system are often desirable.

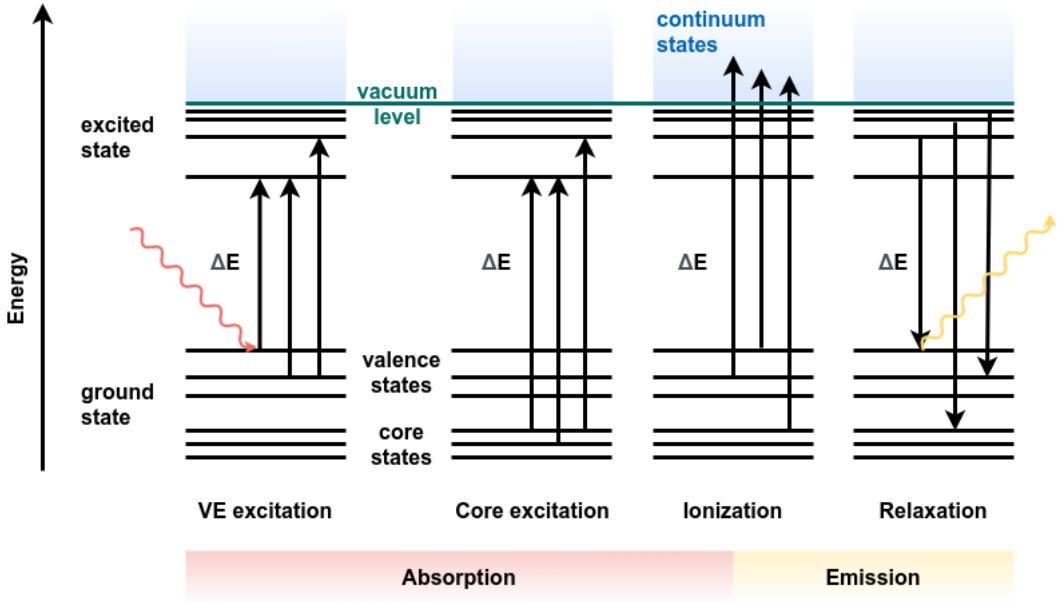

Figure 5 Scheme of electron excitation and relaxation. The different energy levels of the electrons of a system are illustrated with horizontal lines, and their transition given by straight arrows. Besides excitations from valence electron (VE, left) and core (middle left) energy levels, ionization is depicted by excitation of a system bound electron beyond the vacuum level (middle right). Relaxation of electrons from higher energy levels releases energy in the form of light (right).

Excited states are formed by promoting an electron from the ground state to a higher energy level. Figure 5 depicts single-electron excitations from and to different energy levels, namely the promotion of valence electrons (VEs) and core electrons to excited states. When enough energy is provided to an electron, the electron can be promoted beyond the vacuum level, leaving an ionized system behind. The kinetic energy of the released electron matches the provided energy minus the spent ionization potential.

Each excitation or ionization creates a hole in the ground state energy levels of the system, changing its electronic structure and therewith the system's properties. Relaxation from higher, occupied states to such an empty, energetically lower level releases energy, which is emitted in the form of a photon, as depicted on the right of Figure 5. In a single-electron picture, the energy emitted by such an electron transition to a lower energy level exactly matches the energy difference ΔE of the two levels. On the other side, the promotion of an electron to a higher energy level costs energy. This energy can be introduced into the system by interaction with other particles (ions or electrons) or the direct absorption of a photon, which exactly matches the energy difference between the ground state and the excited state.

In experiments, the measurement of a system's absorbed or emitted energy can be used to obtain its different energy levels, which provides information about the system, reaching from

its electronic conductivity to its binding states and reactivity. Experimentally, various ways to excite atoms and more complex chemical systems, as well as measuring its energy level differences have been developed[97]. In the following, the working principle of the two electron spectroscopy methods complementing this work is given.

Electron Energy Loss Spectroscopy In electron energy loss spectroscopy (EELS), the loss of energy of an electron beam transmitted through a thin sample is investigated. The fast electrons of the beam thereby loose a characteristic amount of energy due to inelastic scattering within the investigated material. The transmitted electrons are then separated according to the kinetic energy of the electrons, which creates a spectrum of scattered electron intensities having decreased kinetic energy compared to the initial electron beam[98]. In general, EELS is used for effective compositional analysis of light elements and the exploration of their crystallographic and electronic structure[98,99].

Energy-dispersive X-ray Spectroscopy Energy-dispersive X-ray spectroscopy (EDX) is a widely used, standard electron microscopy method which measures the emission of a system's characteristic X-rays after systematic excitation. The emission of X-rays is a phenomenon produced by the excitation of core electrons with incident electrons, and the subsequent filling of the resulting hole with another electron from a higher shell. The energy freed by this second electron transit is emitted in form of X-rays, featuring the characteristic energy corresponding to the difference between the two energy levels. This quantitative method enables analysis of elemental compositions, and even provides high local resolution if performed with a suitable electron microscope[99]. EDX is easier to conduct than EELS, as thicker samples are measurable. However, in comparison to EELS, lower energy resolution and peak overlap can cause problems in the analysis of the spectrum[98].

For the interpretation of experimentally measured spectra, simulations can be of great aid when assigning the observed peaks to their corresponding origin. The simulation of excited states, however, is not straightforward in DFT. The variational principle, which allows for the search of the ground state electron density, does not hold for excited states. In order to still make predictions of spectroscopic properties employing DFT, several approaches have been developed to describe excited states approximately.
An accurate approach is time-dependent DFT[100,101], which naturally includes many body effects such as spectrum broadening due to electron-hole lifetime. It has been used successfully in the past, but this method demands much higher computational cost than ground state calculations[102,103]. A computationally less demanding approach for standard DFT is to restrict the occupation of a specific core level of an atom in a supercell, rendering good results which are comparable with experiment[91]. In this approach, lifetime broadening is artificially introduced into the simulated spectra by widening with Gaussians. This allows for the direct comparison with experimentally measured spectra, and a detailed analysis of the underlying spectral properties[104].

4.2. Force Fields

As powerful as density functional theory has proven in the past, it reaches its limits for large systems with thousands or even millions of atoms, as the iterative computational procedure necessary to obtain the density becomes in-feasibly expensive. To handle such large systems in a cheaper way, classical mechanics in the form of force fields (FFs) can be used for the description of atomic interactions, trading precision for computational speed by only effectively treating the electron-mediated chemical interactions.

In force fields, atoms and their bonds are approximated as balls and springs. Potential energy and forces between the atoms are approximated by simple mechanical formulas, which are parameterized for the interaction between the different atom types. The purely classical mechanics based description no longer explicitly accounts for electrons and thus the quantum mechanical properties of the atoms, but allows for an efficient prediction of atomic interplay. This enables the access to molecular structures at a fraction of the computational cost of electronic structure methods[94]. Hence, with this approach, simulation cells containing millions of atoms become tractable.

In a crystal in which every atom has a closed valence shell and no formal covalent bonds are present, the Born model of solids[105] identifies all particle interactions as isotropic and thus, the potential between the atoms is only dependent on two-body terms. Hence, for the simulation of crystals purely ionic FFs that only consider pairwise interactions between the atoms can be sufficient. In such a Born-type FF, the interaction between the atoms are reduced to the treatment of the electrostatical interaction, caused by the charges of the ions and the van-der-Waals interaction, originating from polarization of an atom's electron cloud.

For both quantities, simple analytical expressions are available. Electrostatic interactions are described by a Coulomb potential, which treats inter-ionic repulsion or attraction arising from their charges q. Van-der-Waals dispersion and repulsion can accurately be described by a Lennard-Jones potential[92]. A simplification of it is the Buckingham potential, which correctly describes the long range decay of the interaction, however fails to correctly describe very short distances. As such short distances are often not present in an ionic crystal, computations involving a Buckingham potential can be preferable as their computational evaluation is cheaper.

The pairwise interaction between the two atoms i and j can be described by the sum of a Coulomb and a Buckingham potential potential

$$E = \underbrace{\frac{q_i q_j}{4\pi\epsilon_0 r_{ij}}}_{\text{Coulomb}} + \underbrace{A_{ij} e^{\frac{-r_{ij}}{\rho_{ij}}} - \frac{C_{ij}}{r_{ij}^6}}_{\text{Buckingham}} \quad , \tag{4.5}$$

with the Coulomb term depending on the vacuum permittivity ϵ_0, the ionic charges q of the respective atoms and their distance r_{ij}. The Buckingham potential comprises three parameters A_{ij}, C_{ij} and ρ_{ij}, which have to be determined during the creation of the force field. In this process, the parameters are optimized such that the force field is able to reproduce reference data, often experimental data or properties calculated by first principles, e.g. DFT.

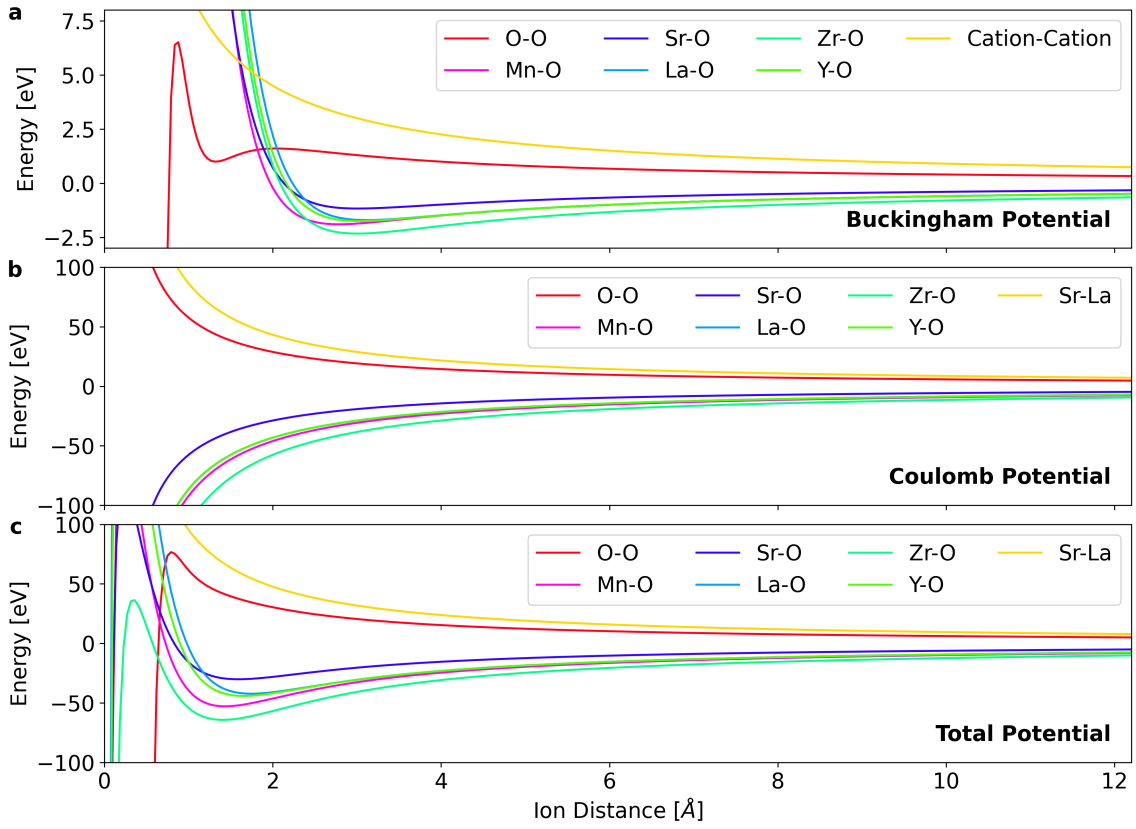

Figure 6 Force field potentials between two respective elements. a) Buckingham potentials. b) Coulomb potentials. As the cation-cation interaction is dependent on the charge of the respective cations, the interaction between Sr and La is given exemplary. c) Total potentials, i.e. the sum of Buckingham and Coulomb potentials obtained by summing Coulomb and Buckingham potentials. The trend for cation-cation interaction is given exemplary for Sr-La.

In order to exemplify the form of these potentials between different ions dependent on the distance of the ions, the potentials of the force field[23,106,107] employed in this work and its individual components are shown in Figure 6. The Buckingham potential makes bonding between certain atom types favorable, and introduces equilibrium bond distances into the system. The Coulomb potential introduces short range repulsion and attraction between ions of same and different charges, respectively. Note, that the Coulomb potential is dependent on the charge of the individual ions, and therefore the Coulombic cation-cation interaction is exemplified only for Sr-La for simplicity. Furthermore it can be seen, that for very short distances the total potential has an unphysically high attraction for some element pairs which is a result of the employed Buckingham potential. However, as these distances smaller than one Ångström are not expected to occur in crystals, this inaccuracy of the potential is dispensable for crystal simulations.

In general, classical force fields are not as accurate as DFT, and highly dependent on the properties they have been fitted against during parametrization. Thus, care must be taken when interpreting results obtained from force fields, and the physical validity cross checked when domains unknown to the force field are calculated.

Nevertheless, as mentioned above, FFs are a powerful tool to treat large molecular systems and their ensembles. Besides computationally cheap structure relaxations and energy

evaluations, FFs allow a rather cheap prediction of temporal evolution of atomic systems via molecular dynamics (MD) simulations, which are introduced in the following.

4.2.1. Molecular Dynamics and Ion Diffusion

The system of classical charged soft spheres representing atoms captured in a Born-type classical force field can be extended to contain a temporal component by the introduction of momenta to the atoms. With positions and momenta of atoms known, the evaluation of Newton's second law of motion allows simulations with step-wise position updates and thus sampling of the high dimensional phase space along a one parameter trajectory[93]. The evaluation of the atomic position evolution over time enables the investigation of time dependent physical properties such as sampling of the free energy and kinetic processes under pre-defined simulation conditions[94].

The evaluation of Newton's equation of motion includes the conservation of motion and energy in a given system of a fixed volume and number of particles over time. However, experimental conditions often imply the constancy of other physical properties, such as constant temperature and pressure, or the exchange of particles with the environment. In simulations, such different thermodynamic ensembles can be realized via introduction of particle baths, thermostats and barostats. These keep the temporal average of the desired property at a constant value, while allowing physically reasonable fluctuations.

For temperature, the size of the fluctuations under specific experimental conditions can be estimated by the variance of the kinetic energy in a real free particle system with corresponding temperature, which is described in the Maxwell-Boltzmann distribution. A certain temperature in a simulation can thus be obtained by assigning kinetic energies sampled from the respective Maxwell-Boltzmann distribution to the atoms. As this distribution is for free particles, a such initialized MD simulation for a system containing molecular bonds or closer atomic interaction needs to equilibrate for an adequate time in order to return physically meaningful results. Then, material specific properties at different temperatures and pressures can be calculated from the further simulation[93,108].

A macroscopic property A of a system corresponds to the ensemble average $\langle A \rangle_e$ over all distributed points in phase space. This equilibrium phase space density distribution can be sampled by a single trajectory, which visits ideally (if the system is not frustrated) all the points in phase space with a frequency proportional to their probability density. At infinite time, this temporal average $\langle A \rangle_t$ will be equal to the ensemble average

$$\langle A \rangle_t = \langle A \rangle_e \quad . \tag{4.6}$$

This fundamental hypothesis of statistical thermodynamics, known as ergodic hypothesis[109], allows the calculation of macroscopic quantities from one or multiple MD simulations, provided that the simulation times are long enough and/or the calculated ensemble resembles properly the investigated phase space.

For this work, a relevant material property obtained by MD is ionic diffusion. Diffusion is

caused by molecular motion in a material, which can be described macroscopically by Fick's laws. To access the mobility of the ions in a material from simulation, the mean square displacement (MSD) can be calculated from an MD trajectory[93] as

$$\mathrm{MSD} = \langle |\vec{r_i}(t) - \vec{r_i}(0)|^2 \rangle \quad . \tag{4.7}$$

The observable obtained from the simulation comprises of the temporal positions r of the atom i, from which the squared distance covered from the beginning of its observation until the time t can be calculated. As the motion of a single atom is based on jumps between lattice sites, which are rare events dependent on the individual local atom environment, the observation of many long atom trajectories is necessary to obtain the desired property from simulation based on reliable statistics.
The diffusion coefficient D can be obtained from the MSD

$$D = \frac{1}{3} \frac{\langle |\vec{r_i}(t) - \vec{r_i}(0)|^2 \rangle}{2\Delta t} \tag{4.8}$$

by taking into account the diffusion time. The dimensionality of the investigated diffusion space, here 3D, is normalized by the factor $\frac{1}{3}$. For more details on calculation of ion mobility and diffusion refer to [93, 94] and [108].

5. Generation of Novel Atomistic Structures

Chemical configuration space is high dimensional even for small systems containing only a few atoms[110–114]. However, its knowledge is highly desirable, as it provides information on favorable structures and transition pathways. As acquirement of the whole space is a often unfeasible task due to its high dimensionality, efficient and smart sampling methods are needed.
In this work, two approaches to access unknown chemical spaces have been used, whose main ideas are described in the following.

5.1. Monte Carlo Simulation

The structure of complexions between any two materials is mostly unknown, and its inherent disorder renders a modeling based on chemical intuition unrealistic. Experimentally, complexions form from interdiffusion of the ions across the grain boundary, which, due to the rareness of the relevant ion transpositions, typically occurs on time scales of minutes to days. Simulation of such long time scales with molecular dynamics is unfeasible, and thus the construction of complexions by this means impossible. However, simulating the interdiffusion process is crucial to assess accurate models of the complexion.
Monte Carlo (MC) probabilistic simulations enable the sampling of rare events by the introduction of random actions weighted by their likelihood to occur. In general, the obtained projection of the underlying distributional space can be used for space exploration or to numerically assess a quantity of interest. In computational chemistry, MC permits coarse graining of atomistic processes, which enables access to equilibrium properties and structure of a system. This renders efficient predictions of a system's evolution on longer time scales through stochastic dynamics possible and enables constructive exploration of chemical configuration spaces as well as the creation of structural ensembles. This makes MC the perfect tool to construct unknown interfacial structures.
In 1953, Metropolis *et al.* proposed an algorithm to stochastically sample a phase space, which laid out the fundamental steps still used in many MC codes today. In general, the algorithm recurrently performs three basic tasks[93,115]:

1. Select a random particle and get particle/system energy
2. Perform step and get particle/system energy
3. Accept or reject step based on a filter, which compares the energies from step 1 and 2

Here, a filter is a selection criterion, which either accepts or rejects steps rated by their probability. A schematic overview of the MC algorithm employing a Metropolis filter is given in Figure 7. This commonly used and physically motivated filter applies the Metropolis accep-

tance criterion[115] yielding the probability p

$$p = min\left(1, e^{-\frac{\Delta E}{k_B T}}\right) \tag{5.1}$$

based on the temperature T, the Boltzmann coefficient k_B and the energy difference ΔE of the initial and the perturbed system. The probability of a step is thus coupled to the energy difference generated by the step, with immediate acceptance if the step leads to a decrease in energy. Otherwise, the probability evaluation can lead to either acceptance or rejection of the proposed move, based on the size of the difference.
Sequential execution of the MC algorithm yields a probabilistic chain, in which each state of a system only depends on the previous state. This is known as a Markov Chain[94].

The validity of a property obtained by MC simulation is based on the accuracy of the model itself, as well as the relevant sampling process. One desired property of MC simulations is that the transition probability should be ergodic, meaning that every point in configuration space is reachable from any other point via only Monte Carlo steps[93]. Furthermore, to guarantee unbiased sampling, it is desirable that once an equilibrium state is reached, it is maintained.

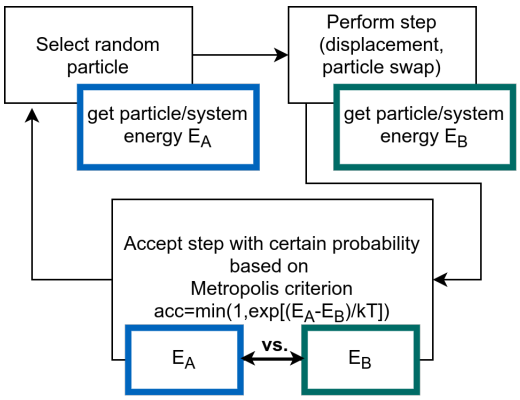

Figure 7 Scheme of the three basic steps that are repeatedly performed in a Monte Carlo simulation.

This can be ensured by making the simulation reversible, which is achieved by following the principle of *detailed balance*. It states that the transition probability π_{ij} from a state i to any other state j multiplied by the probability W_i of being in state i should equal the probability W_j of being in the initial state of the reversed transition multiplied by its transition probability π_{ji} to state i[93,94]:

$$W_i \pi_{ij} = W_j \pi_{ji} \quad . \tag{5.2}$$

In theoretical chemistry, successful MC simulations enable the prediction of many physical properties, while still offering insights on the atomistic level[93]. In this work, MC enables the assessment of the thermodynamic equilibrium structure between the two solids.

5.1.1. Complexion Construction with Monte-Carlo Simulations

SOEC anodes are manufactured by sintering a mixture of the ceramic YSZ and the metal LSM at 1500 K for one hour. To mimic this sintering process in simulations, a workflow for ionic diffusion during the sintering employing a Metropolis Monte Carlo approach was developed. An overview of the workflow is shown in Figure 8.

A step in this MC algorithm denotes the swapping of two cations and relaxing the new structure, and then accepting or rejecting this action according to the Metropolis MC criterion based on the energies of the relaxed system before and after the swap. Every 100 steps, short molecular dynamic simulations are conducted for oxygen ion diffusion and relaxation. In order to realistically mimic the experimental diffusion process, the number of cations participating in this process is cumulatively increased during the simulation, depending on their distance to the interface. Deeper local minima encountered during this simulation are overcome by parallel tempering, where multiple differently tempered simulations called 'walkers' run in parallel and occasionally exchange temperature depending on their potential energy, which increases the probability of acceptance of a step. This simulation is continued until the complexion converges to its equilibrium thickness, which refers to the point where the complexion is not growing anymore. In the simulations, the complexion thickness is determined by the thickness of the transition region of the error function fitted to the Gaussian overlaid atom positions of Mn, which was chosen arbitrarily as reference.

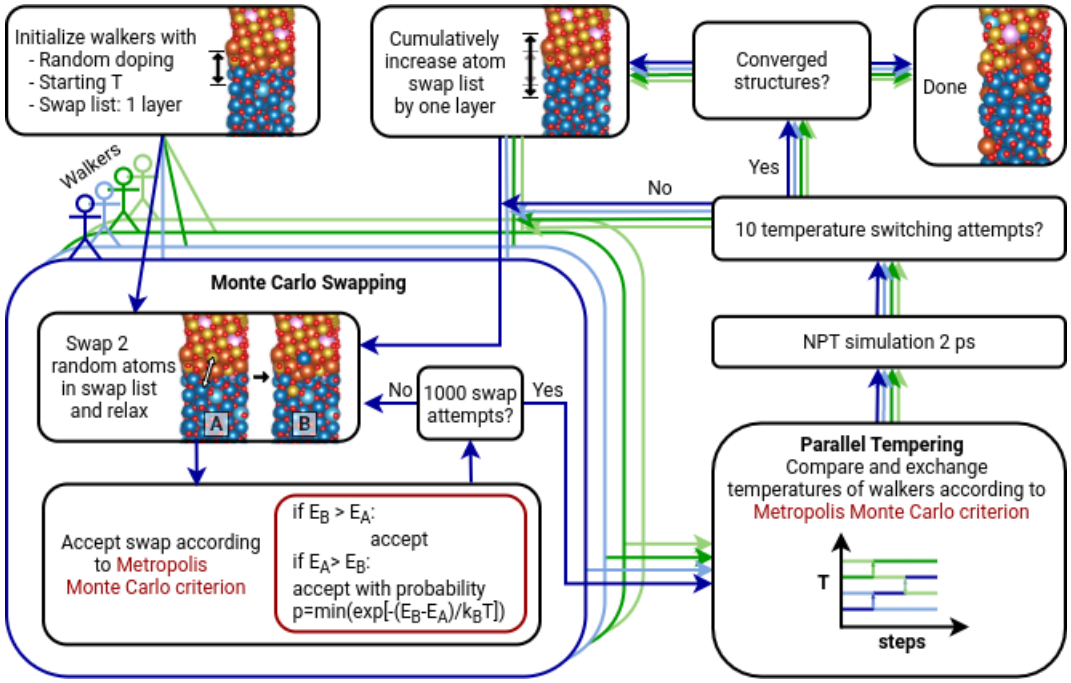

Figure 8 Scheme of the workflow of the developed MC algorithm.

Note, that the here presented Metropolis Monte Carlo is purely based on the potential energies reflecting the thermodynamics of the system. There is no kinetic information going into the process, thus no information about time scales and diffusion barriers can be obtained. The simulation shows thermodynamic strive of the system, and the equilibrium structures obtained correspond to one realization of the system at infinite time.

5.1.2. Application and Usage in this Work

The algorithm described above was used to construct an ensemble of cells with a YSZ/LSM interface. This allowed primarily to gain information on the interfacial structure and to classify it as a complexion[23]. After successful generation of the complexion, its evolution towards vacuum and ion mobilities within the complexion as obtained by MD simulations gave insights into a possible deactivation mechanism[116]. In further work, the knowledge about chemical environments in the complexion can be used for the creation of an ensemble of small, periodic cells resembling the complexion. These can be used for electronic structure calculations and active site determination. A first step to reach this goal was performed by the assessment of generative models, which are explained in the following section.

5.2. Generative Models

Generative models are a group of machine learning (ML) approaches to generate new data based on a known distribution[117,118]. The distribution is fed into the model in form of a training set, as illustrated with a blue arrow in Figure 9. During the training process, the generative model learns the underlying distribution of the training data, making it able to reproduce its fundamental features. A successfully trained generative model can then be sampled which is often performed with random noise that the model maps to new, meaningful data. This process is depicted in green in Figure 9. Ideally, the newly generated data is novel and realistic in such a high degree, that it cannot be distinguished from the training data. The quality of the newly generated data can be used to judge the training process and its precision.

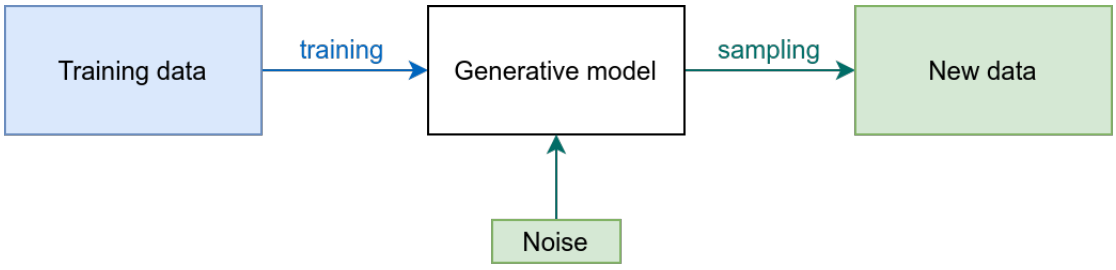

Figure 9 Scheme of the training (blue) and sampling (green) procedure of a generative model. This Figure is based on Figure 1-1 in [117].

The backbone of modern generative model approaches are neural networks (NNs), which are universal function approximators used to capture the underlying distribution of the training set[117,118]. NNs rendered generative models a powerful tool to generate realistic samples, which have successfully been used in many different applications, reaching from the creation of texts to picture, video, and audio generation[119]. In fact, the high flexibility and quality of generative models produced a plethora of implementations and applications. Overviews of possibilities are provided in [118] and [119], including the references therein.
In chemistry, generative models have successfully been used for structure prediction and in-

verse molecular design[118,120–124]. Especially inverse design is of high interest, as it allows the targeted generation of data containing desired features by simple addition of labels classifying the training data. Generative models have even been proposed to predict interfacial structures in battery materials[125], however, this approach has not been realized yet due to its high data demand including experimental measurements.

5.2.1. Artificial Neural Networks

Artificial neural networks are flexible and powerful tools, which are able to learn complex patterns and functions. They are used in many machine learning approaches and often for parametrization of generative models[118]. Their great advantage to ordinary regression models lies in their non-linearity, which is a highly important feature for data generation, as the physical source that generated the training data is often inherently non-linear[126].
Neural networks are an artificial structure that mimic the structure of a brain consistent of interconnected nodes, which are also called neurons after the biological original. A neural network is characterized by three critical components[126–128]

- its architecture, i.e. the design pattern of the connection between the neurons,
- the character of these neurons, determining their individual input and output sizes, as well as biases and activation functions, which introduce non-linearity to the model, and
- the applied learning algorithm that determines the initialization and adjustment of the weights on the connections of a neuron.

An overview of these three properties, explaining the general structure and functionality of NNs, is given in the following.

Network Architecture

A neural network consists of connected nodes, which are organized in layers defined by their connectivity. Every network has an input layer, in which data can be fed, and an output layer, which returns the results computed by the network. Optionally hidden layers can be put in between, which define the deepness of the network and enlarge its learning capacity.
Figure 10 illustrates an exemplary neural network and nomenclature of layers. Note, that this is only one realization of a possible NN, shallower and deeper networks (meaning less or more hidden layers), as well as different sizes and connectivities of the layers are also possible.
The network shown in Figure 10 is a fully connected, feedforward NN, where neurons are connected linearly to subsequent neurons. This architecture is called multiple-layer perceptron, which was first introduced by Rosenblatt[129] and is the most used neural network[127]. It is one of two general network architecture categories[128], the other being recurrent NNs, which include neurons connected to either themselves or pre-passed neurons in a feedback

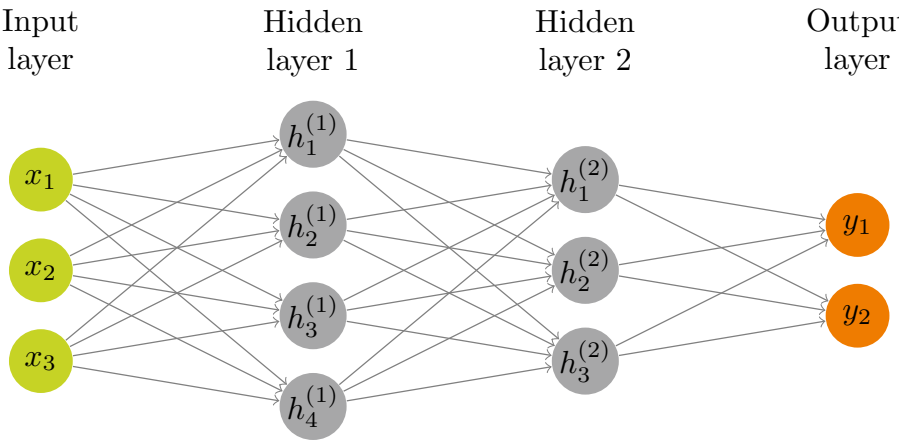

Figure 10 Exemplary neural network structure. Neurons are represented as circles and their connection illustrated by arrows. Their color relates to their affiliated layer.

loop.

The optimal network architecture, i.e. its number of layers, each layer's number of nodes and their connectivity, is dependent on the task of the network, making network design an optimization problem in itself.

Neurons

Artificial neurons are the information-processing units of neural networks. They consist of several basic elements, which together process a given input signal to an output value.

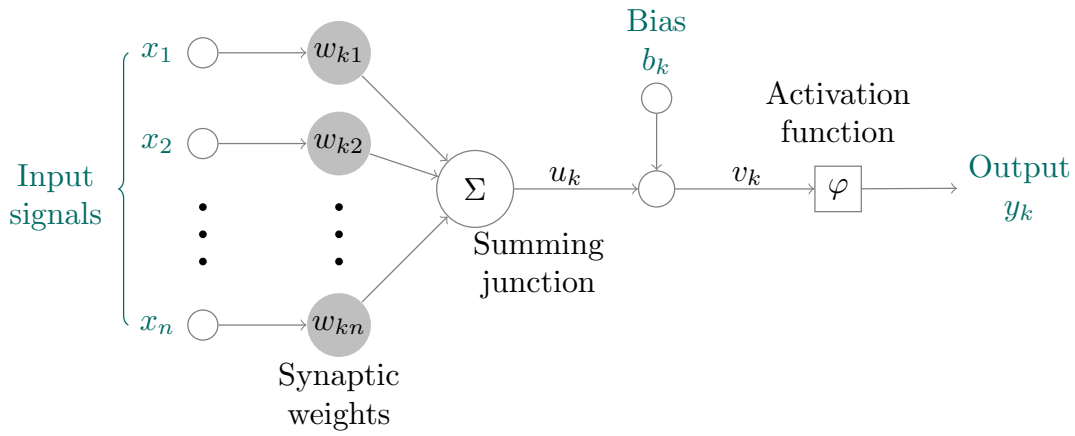

Figure 11 Model of a single neuron k of an artificial neural network. Non-linearity is introduced by the activation function φ. Figure based on Figure 5 in [126].

The basic structure of a neuron is illustrated in Figure 11. The input signals x_j passed into the neuron k are linearly combined by their respective synaptic weights w_{kj} to a single value[126]

$$u_k = \sum_{j=1}^{n} w_{kj} x_j \quad . \tag{5.3}$$

This single output u_k can optionally be altered by adding a bias b_k, which increases or lowers the net input of the subsequent activation function φ. This yields the output signal y_k of the neuron[126]

$$y_k = \varphi(u_k + b_k) \quad . \tag{5.4}$$

The functionality of neurons can be adjusted to a given task by choosing different kinds of activation functions, the usage of a bias b_k, and introduction of normalization with other nodes.

Network Training

Prediction of output from a neural network is produced via forward propagation along its neurons. The value of the output results from the size of the parameters of the network, i.e. its weights and biases. An untrained initialized network has arbitrary parameters, which produce random output. During the training process, the network parameters are adjusted to yield the desired output based on the training data.
The training procedure of a feedforward NN is usually performed by backward propagation[130]. For this, first an input from the training data is propagated through the network and its output calculated. Then, the error between this output and the desired response according to the training data is calculated by a defined loss function. This loss δE is used to adjust the network parameters via propagating backward through the network. The update of the weights is thereby performed by altering the old weight $w_{kj,\mathrm{old}}$ in the direction such that the loss function is minimized[127]. The updated weight $w_{kj,\mathrm{new}}$ is obtained as[126]

$$w_{kj,\mathrm{new}} = w_{kj,\mathrm{old}} + \Delta w_{kj} \quad , \tag{5.5}$$

with the size of the update Δw_{kj} defined as

$$\Delta w_{kj} = -\alpha \frac{\delta E_k}{\delta w_{kj}} \quad . \tag{5.6}$$

Here, the learning rate α serves as training hyperparameter and scales the size of the update.
Note, that this means that the form of the resulting NN depends completely on its initialization, which introduces a factor of randomness into the training procedure. As a result, two NNs with same architecture trained on the same data with different initialization yield a different parametrization and results and their parameters can thus can not be compared.
For successful neural network training, two further points should be considered. The first is the form of representation used for input and output of the network, where the employed ML descriptors should be able to capture all relevant features of training data. Secondly, NNs and particularly generative models are very data expensive, meaning that often a large training set containing thousands of examples is required to obtain adequate results. Furthermore, it is desirable that the training set covers as much as possible of the inquired space, as a network

generally learns the training set distribution and can thus not return meaningful results of spaces largely unknown.

5.2.2. Application in this Work

For the final determination of the active site, electronic structure computations are necessary to estimate the local electron conductivity and enable mechanistic calculations for the OER. The therefore necessary small, periodic cells of the complexion can be generated by use of a generative model, provided an adequate training set and atomic representation is used. As the chemical environment and thus the distributional space of the complexion is available from the MC simulations, the plan to train a generative model to create multiple ensembles of small atomic cells, each representing a local structure of the complexion evolving from YSZ to LSM, emerged.
Yet, we did not know which kind of generative model was best suited to fulfill this task. Thus, together with colleagues a survey of three common deep generative models, namely reinforcement learning, variational autoencoders, and generative adversarial networks, has been conducted to identify the most suitable approach for the investigated problem. Further details on this project can be found in Section 6.3 and in the respective paper[131].

6. Publications

6.1. Complexions at the Electrolyte/Electrode Interface in Solid Oxide Cells

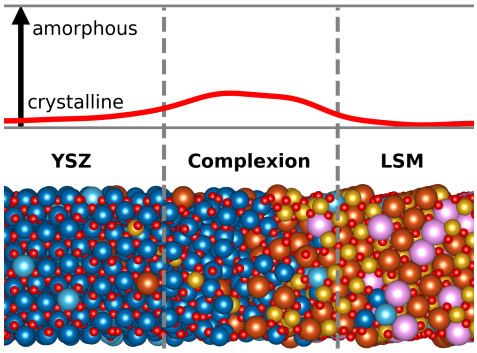

Hanna Türk*, Franz-Philipp Schmidt*, Thomas Götsch*, Frank Girgsdies, Adnan Hammud, Danail Ivanov, Izaak C. Vinke, L.G.J. (Bert) de Haart, Rüdiger-A. Eichel, Karsten Reuter, Robert Schlögl, Axel Knop-Gericke, Christoph Scheurer, and Thomas Lunkenbein,

Adv. Mater. Interfaces **2021**, *8*, 2100967.

*These authors contributed equally to the work.

Summary: In this detailed investigation, we unraveled the fundamental structure of the solid/solid interface of YSZ and LSM, employing an interplay of experimental and theoretical methods. In the first part, high-resolution scanning transmission electron microscopy (HR-STEM) was used to characterize the individual materials. The findings were supported by DFT calculations, revealing the atomic structure of the individual components. Furthermore, an in-depth understanding of the electronic structure of YSZ and LSM was obtained by electron energy loss spectroscopy (EELS), again supported by corresponding theoretical calculations.

In the second part of the study, the morphology of the anode cermet revealed the inter-mixture of the two materials by energy-dispersive X-ray spectroscopy (EDX). A close-up scanning transmission electron microscopy (STEM) image of the interface supported by structural MC simulations revealed the formation of a nanometer wide complexion, which features a higher degree of amorphization compared to the confining bulk phases and irregularly decreasing compositional gradients. With the aid of the simulations, the avoidance of the complexion area by the strontium atoms could be attributed to the larger size of the Sr^{2+} ions, which avoid the complexion due to the absence of large-sized anion polyhedra.

The finding and detailed investigation of the complexion reveals the unknown fundamental nature of the intergranular layer underlying the active site of the air electrode. This is a first step to obtain a picture of the active site at the TPB, which is necessary to determine the reaction mechanism of the OER and the deactivation pathway of the air electrode. It furthermore opens multiple possibilities for chemical interface engineering by e.g. pretreatment or doping, which can be a powerful concept to enhancing cell performance and lifetime.

Individual Contributions: I performed all calculations featured in this paper, including the DFT calculations to characterize the atomic and electronic structure of both materials. Based on the idea of Dr. Christoph Scheurer, I developed an approach to mimic the experimental cell sintering process with force field-based MC simulations. For this, I implemented a routine including MC-based ion swapping and molecular dynamic simulations for structure relaxation, which has since successfully been used by other members of our group. The comparison with experimental data, the analysis and interpretation of the calculation results were performed in close exchange with my coauthors, especially with Dr. Christoph Scheurer who introduced us to the concept and features of complexions.

6.2. Sr Surface Enrichment in Solid Oxide Cells - Approaching the Limits of EDX Analysis by Multivariate Statistical Analysis and Simulations

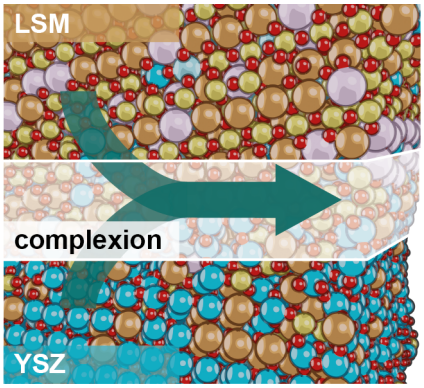

Hanna Türk, Thomas Götsch, Franz-Philipp Schmidt, Adnan Hammud, Danail Ivanov, L.G.J. (Bert) de Haart, Izaak C. Vinke, Rüdiger-A. Eichel, Robert Schlögl, Karsten Reuter, Axel Knop-Gericke, Thomas Lunkenbein, and Christoph Scheurer,

ChemCatChem **2022**, *14*, e202200300.

Summary: In this work, a mechanism for Sr segregation towards the surface via the complexion is proposed. The proposed process is supported by molecular dynamics simulations, which revealed a higher ionic conductivity across the complexion compared to the confining bulk phases. It is shown, that not only the mobility of oxygen ions in comparison to the YSZ bulk, but also the diffusivity of all cations is increased in the complexion. The evolution of the complexion towards the surface is explored with MC simulations, capturing not only for the first time the TPB, but also its long time equilibrium structure. This simulated aging process of the complexion revealed segregation of Mn and Sr to the TPB surface.
In order to confirm this finding with experiments, a robust post-processing routine including drift-correction and non-negative matrix factorization (NMF) was developed to push the resolution of the experimental data, as conventional EDX analysis reached its limit for the detection of the sparsely present doping element Sr. The new routine enables an analysis of the data on the sub-nanoscale, allowing for the detection of minor variances of elemental concentrations in LSM. Combination of the experimental and simulation findings permit the proposal of a mechanism for Sr segregation to the complexion surface via the interfacial area.

Individual Contributions: I conducted and interpreted the MC and MD simulations. Furthermore, together with Dr. Christoph Scheurer and Dr. Thomas Götsch, I developed the post-processing routine of experimental EDX images. Dr. Thomas Götsch and I discussed possible approaches for the drift correction and their implementation. Based on experimental EDX spectra of pure oxide structures obtained from Dr. Franz-Philipp Schmidt, I determined suitable initial-guess matrices for the NMF to enhance the contrast of the elemental compositions. I implemented the application of the drift correction and NMF, using hyperspy[132] and scikit-learn[133]. Furthermore, I conducted the statistical analysis (Welch t-tests) of concentration changes and interpreted the results under consultancy of Dr. Christoph Scheurer.

6.3. Assessing Deep Generative Models in Chemical Composition Space

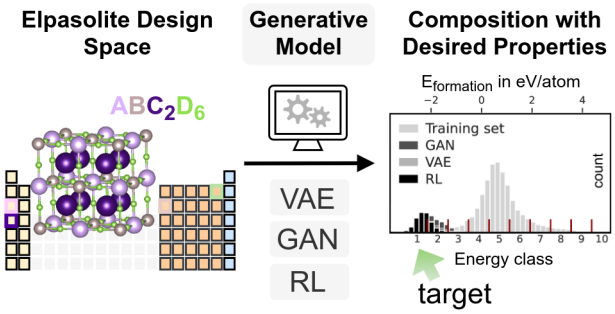

Hanna Türk*, Elisabetta Landini*, Christian Kunkel*, Johannes Margraf, and Karsten Reuter,

Chem. Mater. **2022**, *34*, 9455.

*These authors contributed equally to the work.

Summary: Three different generative models, namely variational autoencoders (VAEs), generative adversarial networks (GAN), and reinforcement learning (RL), were compared in their ability for inverse design in the defined, closed chemical space of the Elpasolite training set from Faber *et al.*[134]. The conditioned generation of new material compositions was investigated by designing metrics assessing their targeted generation and coverage of the investigated chemical space. This allowed the assessment of the performance of the different models for the attempted tasks, which does also allow the determination of proper hyperparameters. Furthermore, the importance of training set size and design was demonstrated by extension of the original data set by exploitation of its symmetry. This allowed an even more exact prediction of the formation energies, and an assessment of reasonable training set sizes compared to the investigated phase space.

The defined metrics deliver a guide for neural network design and training without the necessity of a test or validation set or extensive hyperparameter optimization. This study demonstrates, that all employed models can be tuned to yield similar results for inverse design. The performance of the individual model is rather dependent on the chosen training set and the training procedure due to the chosen hyperparameters.

Individual Contributions: I implemented and computed all results concerning the reinforcement learning. Together with Elisabetta Landini, Dr. Christian Kunkel and Dr. Johannes Margraf, I developed the metrics to define model performance used for comparison of the models, and discussed meaningful hyperparameter, conditioning, representation and loss function choices. Furthermore, I proposed the extension of the dataset by exploiting its symmetry.

6.4. Further Work

Over the course of this work, I co-authored one further paper, which is not directly part of this work and only mentioned here for completeness.

Visualizing the Atomic Structure Between YSZ and LSM: An Interface Stabilized by Complexions? Thomas Götsch, Hanna Türk, Franz-Philipp Schmidt, Izaak C. Vinke, L.G.J. (Bert) de Haart, Robert Schlögl, Karsten Reuter, Rüdiger.-A. Eichel, Axel Knop-Gericke, Christoph Scheurer, and Thomas Lunkenbein *ECS Trans.* **2021**, *103*, 1331.

This work provides a detailed picture of various complexion featuring different crystal orientations. They feature different thicknesses than the previous findings and allows a greater understanding of the form of the complexion. The role of complexions for the activity and stability of SOCs is discussed, with special focus on the influence of pyrochlore formation on cell performance.

7. Conclusion and Outlook

Cell degradation is the limiting factor hindering the wide-spread adoption of solid oxide cells for efficient reversible generation of green hydrogen. The complexity of the relevant air electrode/electrolyte interface renders the identification of the main reason for cell deactivation challenging, and resulted in a plethora of proposed deactivation causes. A lack of fundamental knowledge of the ongoing cell processes on the atomic scale prevents a strategic approach to mitigate the problem.

In this work, a more realistic picture of SOCs and their functionality was obtained by simulating the fundamental structure of the air electrode's active site at an atomistic level. In close cooperation with experiments, a complexion at the electrolyte/electrode interface was uncovered. Its investigation exposed distinctly different properties from the confining bulk phases, featuring lower density, amorphization, compositional gradients and increased ion mobility. Underlying the active site at the triple phase boundary, the complexion greatly influences its form, and thus plays a crucial role in cell activity. Its discovery opens a new design space for this area, and allows tuning of the cell performance via interfacial engineering by targeted doping, pretreatment or coating.

For the first time, generated structures of the triple phase boundary unmasked its thermodynamic equilibrium form, unveiling Sr segregation as a relevant deactivation mechanism. The proposed Sr segregation pathway through the complexion provides a consistent picture of the ongoing cell processes, which again, can be influenced by tailored interfacial engineering. In future work, timescales of this segregation process can be assessed with metadynamic simulations on Sr diffusion in the complexion, which will furthermore provide details on the relevant diffusion mechanisms.

Experimental validation of these findings has been taken to a new level by the newly developed, robust workflow for detection of nano-scale elemental agglomerations, which pushed the resolution limit of EDX, rendering the approach a useful tool for efficient and reliable analysis of experimental data. The increased amount of information derivable from the measured data by employing statistical tests expands the informative value of spatially resolved spectroscopy, which is not restricted to the material system investigated here. For SOCs, further studies employing the method on thermally aged as well as operated cells will provide a deepened understanding of deactivation processes, including structural changes and timescales.

A comparative study of three commonly used generative models allowed the determination of suitable training hyperparameters and comparison metrics. The gained knowledge here opens the door for targeted structure generation and backmapping, allowing the extraction of small periodic cells from larger simulation cells containing the desired distribution. One idea for this is the employment of a GAN[135] following the approach of Kim *et al.*[123] combined with latent space interpolation[136] and use of a classifier for ensemble generation.

Overall, the here provided fundamental concepts, developed workflows and statistical analy-

sis of experimental data are not limited to SOC applications, as they can easily be expanded to further systems and materials. For SOCs, their application led to a deepened understanding of the cell processes and resulted in a new degradation mechanism. This builds a solid foundation for many further investigations on the theoretical and experimental side, which will in combination elucidate the reason for deactivation of the cells. This will allow the strategic development of mitigation strategies which can ultimately increase the lifetime of the SOCs.

Acknowledgements/Danksagung

Mein erster Dank gilt meinem Doktorvater Karsten, für die tolle Aufnahme in die Gruppe, die ich mir nicht besser hätte wünschen können. Und für die viele Unterstützung, Beratung und sehr, sehr schnellen Antworten jederzeit. Während meiner Zeit in der Gruppe habe ich unglaublich viel gelernt und viele tolle Erfahrungen und Erinnerungen gesammelt, von unseren Gruppenworkshops, Konferenzenbesuchen und Segeltörns bis hin zu zahllosen Festen und Feiern.

Sehr großer Dank gilt auch Christoph, den besten Betreuer den ich mir für mich vorstellen kann! Danke vor allem für das viele Wissen, dass du mit mir geteilt hast, für dein Vertrauen und die viele Freiheit, durch die ich so viel für mich erforschen und basteln konnte. Und natürlich auch deine viele Zeitzonen-unabhängige Betreuung, Geduld, Zeit, Anregungen und Diskussionen mit mir.

Ich danke auch meinen experimentelle Kollaborateure, allen voran Thomas Lunkenbein und Thomas Götsch, Franz, Axel, Bert und Ico für die gute Zusammenarbeit, viel Austausch und gute Ergänzungen.

Sehr viel Dank gilt den Mitgliedern unseres generativen Readathon Teams, Christian, Elisabetta und Hannes, für unglaublich viele gute Ideen, Erklärungen und Disskusionen.

Ebenso großer Dank gilt Jutta Rogal und Mark Tuckerman für meinen Forschungsaufenthalt an der New York University, die Integration in eure Gruppe und die vielen guten wissenschaftliche Anregungen und Austausche während und nach meinem Aufenthalt.

Desweiteren danke an unseren IT support und dem IT Admin Team, Christoph, Simeon, Simon Wengert, Martin, David, Zausi, Matthias, Mitch, Christian, χristoph und Steffen, für viel schnelle Hilfe und Unterstützung. Und Ruth und Julia, für bürokratischen Support bei jeder Art von Problemen.

Danke auch an meine vielen tollen Kollegen, von denen viele sehr gute Freunde geworden. Für viele schöne Verteidigungsfeiern, Vino Wednesdays (gute Idee, Thorben), Beer Thursdays, Weihnachtsfeiern mit Kickertunieren und Pekingente, Nerd Nights (mit low budget science fiction), (Geburtstags-)Grillfeste, Spieleabende, Cocktailabende, viele Tee-, Kuchen- und Eispausen ($\cdot\cdot$ $\cdot\cdot$ $\cdots$) und den Oktoberfestbesuch, an die ich mich hoffentlich immer erinnern werde. Und für den vielen Spaß bei unseren gemeinsamen Reisen, zu unseren Gruppenworkshops an den Strand in Sperlonga, ins eiskalte Utrecht mit Radtour und Beertasting, zum Ski fahren nach Bad Gastein, nach Bibow in Schwerin mit Klettergarten und nach Polen mit Volleyballfeld und Spa. Und unsere anschließenden Wochenendtrips nach Amsterdam und Hamburg, zur Summerschool nach Barcelona in der Business class und zum ML=MC Workshop in Lausanne.

Besonderer Dank geht an Frederic für viele Diskussionen in unserem stark begrünten Mystery Office und auch außerhalb (inclusive Kochrezepten und Bouldertipps). Und sina für schöne Schwätzchen und Kaffeepausen, Zimmergenossenschaften und die wunderschöne Zeit in den USA. David für unser gemeinsames Stellung halten in Gebäude U, gegenseitige

Unterstützung und unsere vielen, auch mal längeren Teepausen, Carsten für viele Bartouren und Saunabesuche, und Christian, für sehr viele gute Unterhaltungen, sogar manchmal nicht über die Arbeit. Und natürlich Koko, für unsere vielen schönen Abende, viel gutes Essen und die tolle Zeit in Wien.
Danke auch an unsere sportbegeisterten Volleyballer (Nico, Simon, Sina, Frederic, Thorbetta, Zausi..), Boulderer und unser eisernes Laufteam, den Random Walkers mit Sina, Simon Wengert, Frederic, Cristina und Thorben, trotz des frühen Aufstehens manchmal und unserem Pech beim Losen. Und danke Jakob T., Simiam, Cristina, Nico, Zausi, Thorben, Simeon, Sina, Simon, Martin, Elisabetta, Jakob F., Chiara, Julius, Matthias, Hendrik, Vanessa, Sebastian und den vielen restlichen Kollegen für viel hilfreiche Diskussionen in zahllosen Dingen und viele gute Unterhaltungen.
Zuletzt will ich noch Jonas danken, viel Unterstützung und Wärme während der gesamten Zeit, und meinen Eltern, die immer für mich da sind und mir alles möglich machen.

Berlin, 22. September 2022

Bibliography

[1] T. Spiegel, *J. Sustain. Dev. Energy Water Environ. Syst.* **2018**, *6*, 784–799.

[2] A. Qazi, F. Hussain, N. A. Rahim, G. Hardaker, D. Alghazzawi, K. Shaban, K. Haruna, *IEEE Access* **2019**, *7*, 63837–63851.

[3] P. A. Østergaard, N. Duic, Y. Noorollahi, H. Mikulcic, S. Kalogirou, *Renew. Energy* **2020**, *146*, 2430–2437.

[4] K. F. Kalz, R. Kraehnert, M. Dvoyashkin, R. Dittmeyer, R. Gläser, U. Krewer, K. Reuter, J. D. Grunwaldt, *ChemCatChem* **2017**, *9*, 17–29.

[5] A. S. Brouwer, M. Van Den Broek, A. Seebregts, A. Faaij, *Renew. Sustain. Energy Rev.* **2014**, *33*, 443–466.

[6] I. Pierre, F. Bauer, R. Blasko, N. Dahlback, M. Dumpelmann, K. Kainurinne, S. Luedge, P. Opdenacker, I. Pescador Chamorro, D. Romano, F. Schoonacker, G. Weisrock, *Renew. Action Plan* **2011**, 52.

[7] S. van Renssen, *Nat. Clim. Chang.* **2020**, *10*, 799–801.

[8] O. Ruhnau, *Appl. Energy* **2022**, *307*, 118194.

[9] S. Farrukh, X. Fan, K. Mustafa, A. Hussain, M. Ayoub, M. Younas, *Nanotechnology and the Generation of Sustainable Hydrogen. Green Energy and Technology.* Springer, Cham, **2021**, p. 1.

[10] P. Hennicke, M. Fischedick, *Energy Policy* **2006**, *34*, 1260–1270.

[11] J. L. Silveira, *Sustainable Hydrogen Production Processes. Green Energy and Technology*, Springer, Cham, **2017**, pp. 175–176.

[12] M. Ni, M. K. H. Leung, D. Y. C. Leung, *Int. J. Hydrog. Energy* **2008**, *33*, 2337–2354.

[13] S. R. Foit, I. C. Vinke, L. G. J. D. Haart, R. A. Eichel, L. G. de Haart, R. A. Eichel, *Angew. Chem. Int. Ed.* **2017**, *56*, 5402–5411.

[14] Y. Song, X. Zhang, K. Xie, G. Wang, X. Bao, *Adv. Mater.* **2019**, *31*.

[15] A. Hauch, R. Küngas, P. Blennow, A. B. Hansen, J. B. Hansen, B. V. Mathiesen, M. B. Mogensen, *Science* **2020**, *370*, eaba6118.

[16] C. Sun, R. Hui, J. Roller, *J. Solid State Electrochem.* **2010**, *14*, 1125–1144.

[17] B. Königshofer, M. Höber, G. Nusev, P. Boškoski, C. Hochenauer, V. Subotić, *J. Power Sources* **2022**, *523*, 230982.

[18] R. M. Ormerod, *Chem. Soc. Rev.* **2003**, *32*, 17.

[19] M. S. Khan, X. Xu, R. Knibbe, Z. Zhu, *Renew. Sustain. Energy Rev.* **2021**, *143*, 110918.

[20] K. Chen, S. P. Jiang, *Electrochem. Energy Rev.* **2020**, *3*, 730–765.

[21] L. Kröll, L. G. J. D. Haart, I. Vinke, R. Eichel, *Phys. Rev. Appl.* **2017**, *044007*, 1–22.

[22] S. He, S. P. Jiang, *Prog. Nat. Sci. Mater. Int.* **2021**, *31*, 341–372.

[23] H. Türk, F.-P. Schmidt, T. Götsch, F. Girgsdies, A. Hammud, D. Ivanov, I. C. Vinke, L. G. J. (B.) de Haart, R. Eichel, K. Reuter, R. Schlögl, A. Knop-Gericke, C. Scheurer, T. Lunkenbein, *Adv. Mater. Interfaces* **2021**, *8*, 2100967.

[24] T. Götsch, H. Türk, F.-P. Schmidt, I. C. Vinke, L. G. J. (B.) de Haart, R. Schlögl, K. Reuter, R.-A. Eichel, A. Knop-Gericke, C. Scheurer, T. Lunkenbein, *ECS Trans.* **2021**, *103*, 1331–1337.

[25] S. J. Dillon, M. Tang, W. C. Carter, M. P. Harmer, *Acta Mater.* **2007**, *55*, 6208–6218.

[26] J. Luo, *Energy Storage Mater.* **2019**, *21*, 50–60.

[27] R. O'Hayre, S.-W. Cha, W. G. Colella, F. B. Prinz, *Fuel cell fundamentals*, 3rd, John Wiley & Sons, Inc., Hoboken, New Jersey, **2016**, pp. 315–335.

[28] J. T. Irvine, P. Conner, *Solid Oxide Fuels Cells: Facts and Figures*, Springer-Verlag London, **2012**, p. 4.

[29] P. Kurzweil, *Brennstoffzellentechnik*, 2nd ed., Springer Vieweg, **2013**, p. 175.

[30] H. C. Maru, S. C. Singhal, C. Stone, D. Wheeler, 1 – 10 kW Stationary combined heat and power systems status and technical potential, tech. rep., National Renewable Energy Laboratory, USA, **2010**, p. 13.

[31] M. A. Laguna-Bercero, *J. Power Sources* **2012**, *203*, 4–16.

[32] A. Hammou, *Adv. Electrochem. Sci. Eng.* **2008**, *2*, 88–139.

[33] D. H. Jeon, *Energy* **2019**, *188*, 116050.

[34] Q. Cai, E. Luna-Ortiz, C. S. Adjiman, N. P. Brandon, *Fuel Cells* **2010**, *10*, 1114–1128.

[35] L. B. Chen, *Surf. Rev. Lett.* **2006**, *13*, 535–544.

[36] C. Carbogno, C. G. Levi, C. G. Van De Walle, M. Scheffler, *Phys. Rev. B - Condens. Matter Mater. Phys.* **2014**, *90*, 1–5.

[37] Y. Arachi, H. Sakai, O. Yamamoto, Y. Takeda, N. Imanishai, *Solid State Ion.* **1999**, *121*, 133–139.

[38] R. Pornprasertsuk, P. Ramanarayanan, C. B. Musgrave, F. B. Prinz, *J. Appl. Phys.* **2005**, *98*, 103513.

[39] M. Kilo, C. Argirusis, G. Borchardta, R. A. Jackson, *Phys. Chem. Chem. Phys.* **2003**, *5*, 2219–2224.

[40] C. Ahamer, A. K. Opitz, G. M. Rupp, J. Fleig, *J. Electrochem. Soc.* **2017**, *164*, F790–F803.

[41] M. Boaro, A. S. Aricò, *Advances in Medium and High Temperature Solid Oxide Fuel Cell Technology*, Springer, **2017**, 163ff.

[42] M. B. Mogensen, *Curr. Opin. Electrochem.* **2020**, *21*, 265–273.

[43] N. H. Perry, T. Ishihara, *Materials* **2016**, *9*, 858.

[44] L. Wang, T. Maxisch, G. Ceder, *Phys. Rev. B* **2006**, *73*, 195107.

[45] D. Oh, D. Gostovic, E. D. Wachsman, *J. Mater. Res.* **2012**, *27*, 1992–1999.

[46] W. Jung, H. L. Tuller, *Energy Environ. Sci.* **2012**, *5*, 5370–5378.

[47] S. L. Zhang, H. Wang, M. Y. Lu, A. P. Zhang, L. V. Mogni, Q. Liu, C. X. Li, C. J. Li, S. A. Barnett, *Energy Environ. Sci.* **2018**, *11*, 1870–1879.

[48] Q. Liu, C. Yang, X. Dong, F. Chen, *Int. J. Hydrogen Energy* **2010**, *35*, 10039–10044.

[49] Y. Chen, S. Yoo, Y. Choi, J. H. Kim, Y. Ding, K. Pei, R. Murphy, Y. Zhang, B. Zhao, W. Zhang, H. Chen, Y. Chen, W. Yuan, C. Yang, M. Liu, *Energy Environ. Sci.* **2018**, *11*, 2458–2466.

[50] N. H. Perry, S. R. Bishop, H. L. Tuller, *J. Mater. Chem. A* **2014**, *2*, 18906–18916.

[51] O. A. Marina, L. R. Pederson, M. C. Williams, G. W. Coffey, K. D. Meinhardt, C. D. Nguyen, E. C. Thomsen, *J. Electrochem. Soc.* **2007**, *154*, B452.

[52] S. P. Jiang, *J. Mater. Sci.* **2008**, *43*, 6799–6833.

[53] A. Hauch, S. D. Ebbesen, S. H. Jensen, M. Mogensen, *J. Electrochem. Soc.* **2008**, *155*, B1184.

[54] Y. Wang, W. Li, L. Ma, W. Li, X. Liu, *J. Mater. Sci. Technol.* **2020**, *55*, 35–55.

[55] M. S. Sohal, J. E. O'Brien, C. M. Stoots, V. I. Sharma, B. Yildiz, A. Virkar, *J. Fuel Cell Sci. Tech.* **2012**, *9*, 011017.

[56] R. Knibbe, A. Hauch, S. D. Ebbesen, M. Mogensen, J. Hjelm, A. Hauch, J. Hjelm, S. D. Ebbesen, M. Mogensen, R. Knibbe, S. D. Ebbesen, M. Mogensen, J. Hjelm, *Green* **2011**, *1*, 141–169.

[57] N. H. Menzler, D. Sebold, O. Guillon, *J. Power Sources* **2018**, *374*, 69–76.

[58] L. Blum, L. G. de Haart, J. Malzbender, N. Margaritis, N. H. Menzler, *Energy Technol.* **2016**, *4*, 939–942.

[59] P. Moçoteguy, A. Brisse, *Int. J. Hydrog. Energy* **2013**, *38*, 15887–15902.

[60] G. A. Hughes, K. Yakal-Kremski, S. A. Barnett, *Phys. Chem. Chem. Phys.* **2013**, *15*, 17257–17262.

[61] G. A. Hughes, J. G. Railsback, K. J. Yakal-Kremski, D. M. Butts, S. A. Barnett, *Faraday Discuss.* **2015**, *182*, 365–377.

[62] K. Chen, S. P. Jiang, *J. Electrochem. Soc.* **2016**, *163*, F3070–F3083.

[63] D. The, S. Grieshammer, M. Schroeder, M. Martin, M. Al Daroukh, F. Tietz, J. Schefold, A. Brisse, *J. Power Sources* **2015**, *275*, 901–911.

[64] A. Cadi-Essadek, A. Roldan, N. H. de Leeuw, *Fuel Cells* **2017**, *17*, 125–131.

[65] O. A. Marina, L. R. Pederson, M. C. Williams, G. W. Coffey, K. D. Meinhardt, C. D. Nguyen, E. C. Thomsen, *J. Electrochem. Soc.* **2007**, *154*, B452.

[66] Y. Dong, Z. Zhang, A. Alvarez, I. W. Chen, *Acta Mater.* **2020**, *199*, 264–277.

[67] K. Chen, S. P. Jiang, *Int. J. Hydrogen Energy* **2011**, *36*, 10541–10549.

[68] J. A. Labrincha, J. R. Frade, F. M. Marques, *J. Mater. Sci.* **1993**, *28*, 3809.

[69] K. Yang, J. H. Shen, K. Y. Yang, I. M. Hung, K. Z. Fung, M. C. Wang, *J. Power Sources* **2006**, *159*, 63.

[70] Y. Huang, J. M. Vohs, R. J. Gorte, *J. Electrochem. Soc.* **2006**, *153*, A951.

[71] A. Chen, J. R. Smith, K. L. Duncan, R. T. DeHoff, K. S. Jones, E. D. Wachsman, *J. Electrochem. Soc.* **2010**, *157*, B1624.

[72] M. Keane, M. K. Mahapatra, A. Verma, P. Singh, *Int. J. Hydrogen Energy* **2012**, *37*, 16776–16785.

[73] A. Momma, T. Kato, Y. Kaga, S. Nagata, *J. Ceram. Soc. Japan* **1997**, *105*, 369–373.

[74] M. Mogensen, T. Jacobsen, *ECS Trans.* **2008**, *13*, 259.

[75] S. N. Rashkeev, M. V. Glazoff, *Int. J. Hydrogen Energy* **2012**, *37*, 1280–1291.

[76] A. Neumann, M. N. H., I. Vinke, H. Lippert, *ECS Trans.* **2009**, *25*, 2889–2898.

[77] S. P. Jiang, *J. Mater. Sci.* **2008**, *43*, 6799–6833.

[78] G. Chen, Y. Gao, Y. Luo, R. Guo, *Ceram. Int.* **2017**, *43*, 1304–1309.

[79] J. Liu, Y. Yu, T. Yang, O. Ozmen, H. Finklea, E. M. Sabolsky, H. Abernathy, P. R. Ohodnicki, G. A. Hackett, *ECS Trans.* **2017**, *78*, 689–699.

[80] M. S. Khan, X. Xu, J. Zhao, R. Knibbe, Z. Zhu, *J. Power Sources* **2017**, *359*, 104–110.

[81] T. Wu, W. Zhang, Y. Li, Y. Zheng, B. Yu, J. Chen, X. Sun, *Adv. Energy Mater.* **2018**, *8*, 1802203.

[82] Y. Song, X. Zhang, Y. Zhou, Q. Jiang, F. Guan, H. Lv, G. Wang, X. Bao, *Energy Storage Mater.* **2018**, *13*, 207–214.

[83] J. Kim, H. I. Ji, H. P. Dasari, D. Shin, H. Song, J. H. Lee, B. K. Kim, H. J. Je, H. W. Lee, K. J. Yoon, *Int. J. Hydrogen Energy* **2013**, *38*, 1225–1235.

[84] S. Bai, W. Jiang, Z. Li, Y. Xiong, *ChemNanoMat* **2015**, *1*, 223–239.

[85] K. X. Wang, X. H. Li, J. S. Chen, *Adv. Mater.* **2015**, *27*, 527–545.

[86] A. Subramaniam, C. T. Koch, R. M. Cannon, M. Rühle, *Mater. Sci. Eng. A* **2006**, *422*, 3–18.

[87] M. Backhaus-Ricoult, *Solid State Ion.* **2006**, *177*, 2195–2200.

[88] W. Bollmann, *Crystal Defects and Crystalline Interfaces*, Springer-Verlag Berlin Heidelberg GmbH, **1972**, p. 247.

[89] P. R. Cantwell, T. Frolov, T. J. Rupert, A. R. Krause, C. J. Marvel, G. S. Rohrer, J. M. Rickman, M. P. Harmer, *Annu. Rev. Mater. Res.* **2020**, *50*, 465–492.

[90] J. Timmermann, F. Kraushofer, N. Resch, P. Li, Y. Wang, Z. Mao, M. Riva, Y. Lee, C. Staacke, M. Schmid, C. Scheurer, G. S. Parkinson, U. Diebold, K. Reuter, *Phys. Rev. Lett.* **2020**, *125*, 206101.

[91] W. Koch, M. C. Holthausen, *A Chemist ' s Guide to Density Functional Theory*, 2nd ed., Wiley-VCH Verlag GmbH, **2001**.

[92] C. J. Cramer, *Essentials of Computational Chemistry Theories and Models*, 2nd ed., John Wiley & Sons Ltd, **2004**.

[93] D. Frenkel, B. Smit, *Understanding Molecular Simulation*, 1st ed., Academic Press, **2002**, pp. 63–89.

[94] M. E. Tuckerman, *Statistical Mechanics: Theory and Molecular Simulation*, Oxford University Press, **2010**, pp. 1–368.

[95] P. Hohenberg, W. Kohn, *Phys. Rev.* **1964**, *136*, 864–871.

[96] W. Kohn, L. Sham, *Phys. Rev.* **1965**, *140*, A1133–A1138.

[97] M. F. Vitha, *Spectroscopy: Principles and Instrumentation*, 1st ed., John Wiley & Sons, Inc. 1, **2019**, pp. 1–25.

[98] R. Egerton, *Electron Energy-Loss Spectroscopy in the Electron Microscope*, Springer US, Boston, MA, **2011**, pp. 3–24.

[99] D. Shindo, T. Oikawa, *Analytical Electron Microscopy for Materials Science*, Spinger-Verlag Tokyo, **2002**, pp. 43–81.

[100] M. Stener, G. Fronzoni, M. de Simone, *Chem. Phys. Lett.* **2003**, *373*, 115–123.

[101] M. E. Casida, M. Huix-Rotllant, *Annu. Rev. Phys. Chem.* **2012**, *63*, 287–323.

[102] M. A. L. Marques, N. T. Maitra, F. M. S. Nogueira, E. K. U. Gross, A. Rubio, *Fundamentals of Time-Dependent DFT*, Springer-Verlag Berlin Heidelberg, **2012**, p. 56.

[103] G. S. Michelitsch, PhD thesis, *Ab Initio simulation of core-level spectroscopies and correlated materials*, Technische Universität München, München, **2019**.

[104] R. J. Nicholls, A. J. Morris, C. J. Pickard, J. R. Yates, *J. Phys. Conf. Ser.* **2012**, *371*, 2–6.

[105] M. Born, K. Huang, *Dynamical theory of crystal lattices*, Oxford University Press, Oxford, UK, **1954**.

[106] H. W. Brinkman, W. J. Briels, H. Verweij, *Chem. Phys. Lett.* **1995**, *247*, 386.

[107] M. S. Islam, M. Cherry, C. R. A. Catlow, *J. Solid State Chem.* **1996**, *124*, 230.

[108] H. H. Heenen, PhD thesis, *Multiscale Modeling of Disorder in Solid-State Battery Materials*, Technische Universität München, München, **2018**.

[109] Y. N. Kaznessis, *Statistical Thermodynamics and Stochastic Kinetics - An Introduction for Engineers*, Cambridge University Press, **2011**, pp. 83–124.

[110] P. Kirkpatrick, C. Ellis, *Nature* **2004**, *432*, 823.

[111] P. G. Polishchuk, T. I. Madzhidov, A. Varnek, *J. Comput. Aided. Mol. Des.* **2013**, *27*, 675–679.

[112] G. M. Maggiora, J. Bajorath, *J. Comput. Aided. Mol. Des.* **2014**, *28*, 795–802.

[113] B. Huang, O. A. von Lilienfeld, *arXiv Prepr. arXiv2012.07502* **2020**, 1–44.

[114] A. Chen, X. Zhang, Z. Zhou, *InfoMat* **2020**, *2*, 553–576.

[115] N. Metropolis, A. W. Rosenbluth, M. N. Rosenbluth, A. H. Teller, E. Teller, *J. Chem. Phys.* **1953**, *21*, 1087–1092.

[116] H. Türk, T. Götsch, F.-P. Schmidt, A. Hammud, D. Ivanov, L. (B.) de Haart, I. Vinke, R.-A. Eichel, R. Schlögl, K. Reuter, A. Knop-Gericke, T. Lunkenbein, C. Scheurer, *ChemCatChem* **2022**, *14*, e202200300.

[117] D. Foster, *Generative Deep Learning*, 1st ed., O'Reilly Media, **2019**, pp. 3–31.

[118] J. M. Tomczak, *Deep Generative Modeling*, 1st ed., Springer imprint, **2022**.

[119] M. Brundage, S. Avin, J. Clark, H. Toner, P. Eckersley, B. Garfinkel, A. Dafoe, P. Scharre, T. Zeitzoff, B. Filar, H. Anderson, H. Roff, G. C. Allen, J. Steinhardt, C. Flynn, S. Ó. hÉigeartaigh, S. Beard, H. Belfield, S. Farquhar, C. Lyle, R. Crootof, O. Evans, M. Page, J. Bryson, R. Yampolskiy, D. Amodei, *arXiv:1802.07228* **2018**, 1–65.

[120] B. Sanchez-Lengeling, A. Aspuru-Guzik, *Science* **2018**, *361*, 360–365.

[121] A. Aspuru-Guzik, K. Persson, *Materials Acceleration Platform - Accelerating Advanced Energy Materials Discovery by Integrating High-Throughput Methods with Artificial Intelligence. Mission Innovation: Innovation Challenge 6*, **2018**.

[122] J. Noh, J. Kim, H. S. Stein, B. Sanchez-Lengeling, J. M. Gregoire, A. Aspuru-Guzik, Y. Jung, *Matter* **2019**, *1*, 1370–1384.

[123] B. Kim, S. Lee, J. Kim, *Sci. Adv.* **2020**, *6*, 1–8.

[124] Z. Ren, S. I. P. Tian, J. Noh, F. Oviedo, G. Xing, J. Li, Q. Liang, R. Zhu, A. G. Aberle, S. Sun, X. Wang, Y. Liu, Q. Li, S. Jayavelu, K. Hippalgaonkar, Y. Jung, T. Buonassisi, *Matter* **2022**, *5*, 314–335.

[125] A. Bhowmik, I. E. Castelli, J. M. Garcia-Lastra, P. B. Jørgensen, O. Winther, T. Vegge, *Energy Storage Mater.* **2019**, *21*, 446–456.

[126] S. Haykin, *Neural Networks and Learning Machines*, 3rd ed., Pearson Education, **2019**, pp. 2–12.

[127] D. Livingstone, *Artificial Neural Networks*, 1st ed., Humana Press, **2008**, pp. 21–44.

[128] S. Bhattacharyya, V. Snasel, A. E. Hassanien, S. Saha, B. K. Tripathy, *Deep learning*, 1st ed., Walter de Gruyter GmbH, Berlin/Boston, **2020**, pp. 3–15.

[129] F. Rosenblatt, Principles of neurodynamics: perceptrons and the theory of brain mechanisms, tech. rep., Cornell Aeronautical Laboratory, inc., **1961**.

[130] D. E. Rumelhart, J. L. McClelland, *Parallel Distributed Processing*, 1st ed., MIT Press, **1986**.

[131] H. Türk, E. Landini, C. Kunkel, J. T. Margraf, K. Reuter, *Chem. Mater.* **2022**, *34*, 9455–9467.

[132] Hyperspy: DOI 10.5281/zenodo.592838.

[133] F. Pedregosa, G. Varoquaux, A. Gramfort, V. Michel, B. Thirion, O. Grisel, M. Blondel, P. Prettenhofer, R. Weiss, V. Dubourg, J. Vanderplas, A. Passos, D. Cournapeau, M. Brucher, M. Perrot, E. Duchesnay, *J. Mach. Learn. Res.* **2011**, *12*, 2825–2830.

[134] F. A. Faber, A. Lindmaa, O. A. von Lilienfeld, R. Armiento, *Phys. Rev. Lett.* **2016**, *117*, 135502.

[135] I. Goodfellow, J. Pouget-Abadie, M. Mirza, B. Xu, D. Warde-Farley, S. Ozair, A. Courville, Y. Bengio, *Commun. ACM* **2014**, *63*, 139–144.

[136] T. White, *arXiv preprint arXiv:1609:04468v3* **2016**, 1–11.

List of Figures

Appendix

Paper 1

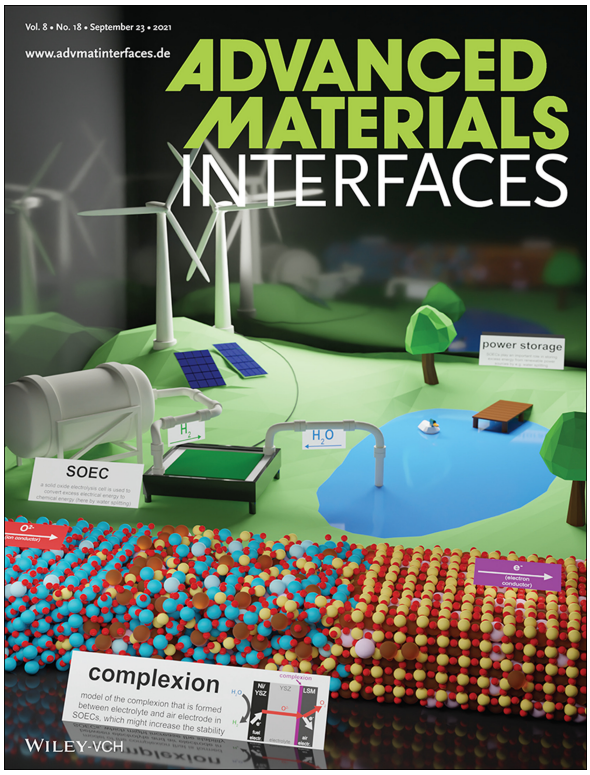

Complexions at the Electrolyte/Electrode Interface in Solid Oxide Cells

Hanna Türk*, Franz-Philipp Schmidt*, Thomas Götsch*, Frank Girgsdies, Adnan Hammud, Danail Ivanov, Izaak C. Vinke, L.G.J. (Bert) de Haart, Rüdiger-A. Eichel, Karsten Reuter, Robert Schlögl, Axel Knop-Gericke, Christoph Scheurer, and Thomas Lunkenbein

Adv. Mater. Interfaces **2021**, *8*, 2100967.

*These authors contributed equally to the work.

RESEARCH ARTICLE

ADVANCED MATERIALS INTERFACES
www.advmatinterfaces.de

Complexions at the Electrolyte/Electrode Interface in Solid Oxide Cells

Hanna Türk, Franz-Philipp Schmidt, Thomas Götsch, Frank Girgsdies, Adnan Hammud, Danail Ivanov, Izaak C. Vinke, L.G.J. (Bert) de Haart, Rüdiger-A. Eichel, Karsten Reuter, Robert Schlögl, Axel Knop-Gericke, Christoph Scheurer, and Thomas Lunkenbein*

Rapid deactivation presently limits a wide spread use of high-temperature solid oxide cells (SOCs) as otherwise highly efficient chemical energy converters. With deactivation triggered by the ongoing conversion reactions, an atomic-scale understanding of the active triple-phase boundary between electrolyte, electrode, and gas phase is essential to increase cell performance. Here, a multi-method approach is used comprising transmission electron microscopy and first-principles calculations and molecular simulations to untangle the atomic arrangement of the prototypical SOC interface between a lanthanum strontium manganite (LSM) anode and a yttria-stabilized zirconia (YSZ) electrolyte in the as-prepared state after sintering. An interlayer of self-limited width with partial amorphization and strong compositional gradient is identified, thus exhibiting the characteristics of a complexion that is stabilized by the confinement between two bulk phases. This offers a new perspective to understand the function of SOCs at the atomic scale. Moreover, it opens up a hitherto unrealized design space to tune the conversion efficiency.

1. Introduction

The intermittent output of renewable energy sources such as wind or solar power requires an efficient way for the mid-term storage of excess electrical energy. Solid oxide fuel and electrolysis cells (SOFCs, SOECs) offer the prospect of high performance devices,[1,2] reaching more than 80% efficiency,[3] while, at the same time, providing mid- to long-term chemical storage capability.

As shown in **Figure 1**a, these cells typically consist of an oxygen-ion-conducting ceramic electrolyte such as yttria-stabilized zirconia (YSZ, $(Y_2O_3)_x(ZrO_2)_{1-x}$) and a Ni/YSZ fuel electrode. A perovskite like lanthanum strontium manganite (LSM, $(La,Sr)MnO_{3-\delta}$) acts as air electrode where it is typically mixed with YSZ.[3–5] The electrolyzer cell converts electrical to chemical energy e.g. by splitting water into H_2 and O_2, which can be stored. The reversed operation in fuel cell mode enables the back-transformation of chemical energy to electricity by oxidizing H_2 with O_2 to form H_2O. This bifunctionality of solid oxide cells is depicted in Figure 1a. The key to the high efficiency of these cells is the elevated operation temperature, which typically exceeds 1000 K. However, commercial operation is not yet practical as the cells suffer from degradation even under steady state conditions.[6] This needs to be mitigated to render a widespread adoption of SOECs and SOFCs feasible and overcome intermittent power availability.[7] Predominant degradation occurs at the anode of the electrolyzer cells, where the oxygen evolution reaction (OER) shows a higher kinetic limitation compared to the processes taking place at the cathode.[8,9]

H. Türk, K. Reuter, C. Scheurer
Chair for Theoretical Chemistry and Catalysis Research Center
Department of Chemistry, Technische Universität München
Lichtenbergstraße 4, 85748 Garching, Germany
H. Türk, K. Reuter, C. Scheurer
Theory Department
Fritz-Haber-Institut der Max-Planck-Gesellschaft
Faradayweg 4–6, 14195 Berlin, Germany

The ORCID identification number(s) for the author(s) of this article can be found under https://doi.org/10.1002/admi.202100967.

DOI: 10.1002/admi.202100967

F.-P. Schmidt, T. Götsch, F. Girgsdies, A. Hammud, D. Ivanov, R. Schlögl, A. Knop-Gericke, T. Lunkenbein
Department of Inorganic Chemistry
Fritz-Haber-Institut der Max-Planck-Gesellschaft
Faradayweg 4–6, 14195 Berlin, Germany
E-mail: goetsch@fhi-berlin.mpg.de
F.-P. Schmidt, R. Schlögl, A. Knop-Gericke
Department of Heterogeneous Reactions
Max Planck Institute for Chemical Energy Conversion
Stiftstraße 34–36, 45470 Mülheim an der Ruhr, Germany
I. C. Vinke, L.G.J. (B.) de Haart, R.-A. Eichel
Fundamental Electrochemistry (IEK-9), Institute of Energy and Climate Research
Forschungszentrum Jülich GmbH
52425 Jülich, Germany
R.-A. Eichel
Institute of Physical Chemistry
RWTH Aachen University
52056 Aachen, Germany

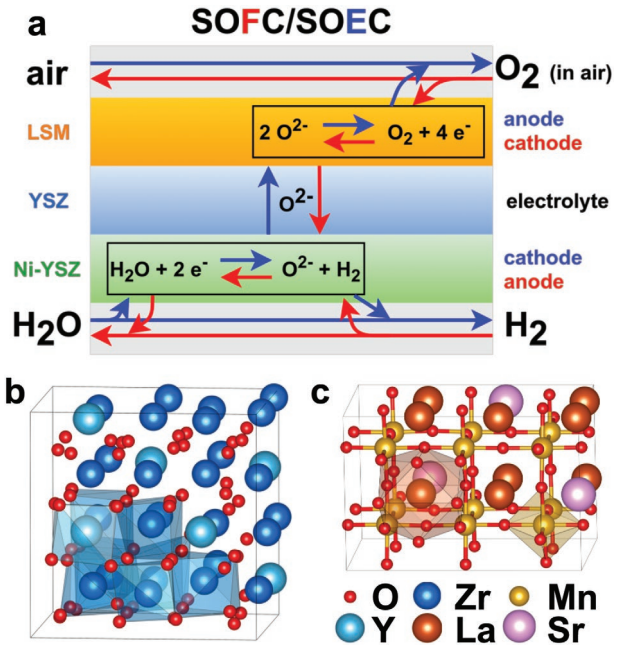

Figure 1. a) Schematic representation of the bifunctionality of solid oxide cells. The reaction pathways for fuel cell (red) and electrolysis operation mode (blue) are indicated by different colors. Unit cells of b) 10YSZ (YSZ with 10mol% Y_2O_3, $(Y_2O_3)_{0.1}(ZrO_2)_{0.9}$) and c) LSM25 (LSM with 25at% of Sr in the cuboctahedral A site of the general ABO_3 perovskite, $La_{0.75}Sr_{0.25}MnO_3$) for one probable doping distribution, relaxed using density functional theory (DFT). The deviations from the experimentally used concentrations are necessary to obtain cell sizes suitable for DFT. The elements are labelled by color and atomic-radii-dependent spheres as defined in the legend. Polyhedra were added to each structure indicating coordination environments.

For a purely electron-conducting air electrode such as LSM, the triple phase boundary (TPB) between YSZ, gas phase and LSM is considered to be the active site.[4] In this assembly, YSZ provides O^{2-}, whereas the formed molecular oxygen will escape to the gas phase and LSM is used for current collection. Thus, an understanding of the degradation processes can be achieved by investigating the morphological and chemical changes of the TPB, such as reduction of the number of TPBs by delamination, or chemical reactions at the electrolyte/electrode interface.

Multiple studies have investigated the macroscopic properties of the YSZ/LSM interface, focusing on the influence of the preparation method, oxygen content, polarization and aging on resistance,[10,11] reaction kinetics[12] and the formation of inactive pyrochlore layers.[13,14] On the mesoscale, the formation of micropores and ring-shaped contact craters of YSZ and long range Mn and La segregation have been described.[15–18] However, when considering the atomic scale, published works discuss controversially the nature of the interface. Backhaus-Ricoult et al. proposed the formation of a solid solution on the zirconia side,[19–21] and Chen et al. reported nano precipitates as well as an amorphous film at the LSM/YSZ grain boundary after operation.[22] He et al., on the other hand, described a semi-coherent interface between YSZ and LSM with neither an amorphous phase nor a solid solution and the formation of an "intimate interface".[17,18] The clarification of the interfacial nanostructure is essential to answer many questions that are crucial for the overall cell performance concerning interfacial properties, microstructure and stability.[23] A lack of theoretical support for a comprehensive structural analysis has rendered the detailed structure at the interface of YSZ with an LSM grain underneath the TPB, and even more so the TPB's structure itself, elusive. Density functional theory (DFT) investigations of this complex interface, for instance, are rare and focus on defect formation as well as doping of perfect crystals and surfaces.[24] The assumption of an idealized, atomically thin, truly two-dimensional (2D) interface region makes the TPB a one-dimensional line with minimal active surface. Additionally, the transport of oxygen ions from YSZ to the catalytically active LSM, as well as the elementary steps of the reaction at the TPB, including oxygen exchange with the gas phase, remain unclear when considering neighboring pure LSM and YSZ phases with bulk properties.[25–27] From detailed studies of intergranular interface regions in alloys and functional ceramic materials, a more diverse picture has emerged over the last decade, which comprises a variety of interface types. These range systematically from single layer, highly ordered interfaces, via double, triple, and multiple layer types with high residual order to fully disordered intergranular films (IGF) with a truly amorphous interphase between neighboring grains. The interfacial structural types in this classification system have been termed complexions.[28–32] Complexions are not stable as a bulk three-dimensional (3D) phase. They can exist, though, as thermodynamically stable, quasi 2D interfacial structures of finite, self-limiting width between adjacent bulk phases and exhibit reproducibly distinct physical and chemical properties. A surface cutting through a YSZ ‖ complexion ‖ LSM region or evolving like a spandrel from such an underlying complexion could present a TPB of finite width with mixed ionic/electronic conductivity (MIEC), explaining the propensity for oxygen exchange with the gas phase.

In the first part of this study, we use transmission electron microscopy (TEM) on the experimental side, and DFT on the theoretical side to characterize the structural properties of the SOEC anode material and electrolyte at the nano and atomic scale. For this purpose, an as-prepared half cell consisting of an LSM + YSZ air electrode, which reflects the anode of the electrolyzer, on top of an 8YSZ (ZrO_2 with 8mol% Y_2O_3) electrolyte is investigated after sintering in air at 1423 K for 1 h. As current collector, pure LSM20 ($(La_{0.8}Sr_{0.2})_{0.95}MnO_{3-\delta}$) is used. The results are interpreted with the aid of DFT calculations, allowing to establish a detailed picture of the electronic structure and state of the materials (see Figure 1b,c for the cubic crystal structures as obtained by theory). Based on the understanding gained from the material characterization, the interface of LSM and YSZ is examined in the final part using energy-dispersive X-ray spectroscopy (EDX), giving insights into the composition of the active phase, supported by force-field-based MC simulations. These, together with high-resolution scanning TEM (HR-STEM), are used to elucidate the structural configuration of the formed complexion at the atomic level.

2. Results and Discussion

2.1. Crystallography of LSM

As evidenced by X-ray diffraction (XRD) data shown in Figures S1 and S2, Supporting Information, LSM crystallizes in

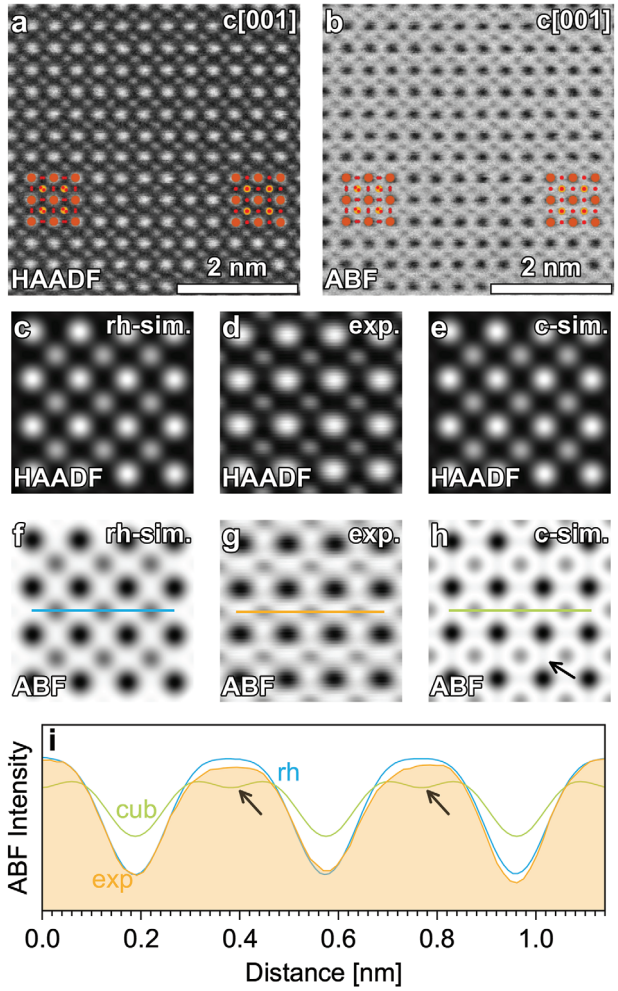

Figure 2. Bulk HAADF (a) and ABF (b) HR-STEM images of LSM in c[001] zone axis (corresponding to rh[241]). The crystal structures of rhombohedral (left) and cubic (right) perovskites are overlaid on the images (La: orange, Mn: yellow, O: red), see Figure S3, Supporting Information. Experimental average over 1034 frames in a 14 nm × 14 nm region by template matching (d, g) in comparison to simulated images for the rhombohedral (c, f) and cubic (e, h) perovskite. i) The experimental line profile (in c[100] direction across the Mn sites) of the ABF-STEM image agrees very well with the simulated intensity based on the rhombohedral structure. The dip due to the O atoms (black arrows), which is visible in the cubic case only, cannot be observed.

the rhombohedral perovskite structure (ABO_3) at room temperature. However, under operation conditions (i.e., 1000–1200 K), this structure has been shown to become pseudocubic,[33,34] and at the typical sintering temperature of around 1400 K, a fully cubic perovskite is formed.[35] The rhombohedral structure can be conceived as a distorted cubic lattice where the [BO_6] octahedra are tilted around the threefold rotation axis.[36] This results in a displacement of the oxygen sites while the positions of the cations are unaffected. The structure is further analyzed in **Figure 2**. In the rhombohedral rh[241] viewing direction, which is equivalent to c[001] for the cubic perovskite, the oxygen atoms between the La sites split from single columns into two distinct locations. This is indicated by the red oxygen atoms in the structural insets of Figure 2a,b (left inset: rhombohedral, right inset: cubic), as well as in Figure S3, Supporting Information in more detail. However, while the raw high-angle annular dark field STEM (HAADF-STEM) and annular bright field STEM (ABF-STEM) images in Figure 2a,b (most intense atoms: La, less intense: Mn), respectively, are generally adequate for investigating potential cation displacements and distortions, they exhibit an insufficient signal-to-noise ratio for determining the positions of the O sites. Thus, an average over 1034 unit cells within each image (14 nm × 14 nm) was formed by template matching and rigid registration (see Figure S4, Supporting Information for more details). The results of this procedure are given in Figure 2d (HAADF-STEM) and Figure 2g (ABF-STEM). For comparison, simulated STEM images with matching beam and microscope aberration parameters (see the Methods section) are displayed in Figure 2c,f (rhombohedral), as well as Figure 2e,h (cubic). The cubic ABF-STEM image simulation (Figure 2h) hints at some contrast stemming from the O columns (black arrow), which is not the case for the rhombohedral ABF-STEM image (Figure 2f). The experimental average in Figure 2g resembles more the rhombohedral simulation compared to the cubic simulation. This is corroborated by the horizontal line scans along the [100] direction through the Mn sites in Figure 2i. Whereas the cubic case (green line) shows a clear dip at the expected positions of the O atoms (marked by arrows), the rhombohedral simulation (blue) and the experimental intensity profile (orange shaded region) do not. This points towards a rhombohedral rather than a cubic structure for LSM. Although this averaging procedure might hide local contributions of single cubic unit cells inside a matrix of rhombohedral cells, this approach serves as a good way of determining the crystallographic phase on the nanometer scale from HR-STEM images. For instance, it has been reported that oxygen vacancies, which might be formed during OER operation, stabilize cubic phases of perovskites.[37] Thus, while the resulting local crystallographic deviations would not be visible in bulk XRD data, the HR-STEM unit cell averaging approach would excel.

2.2. The YSZ/LSM Interface

The electrolyte/electrode interface constitutes an integral part within SOECs and SOFCs and its composition may influence the structure at the adjacent TPB and thus the performance. An in-depth view on the elemental spread across the YSZ/LSM interface is therefore crucial. In the following, the focus is put on the YSZ/LSM interface of a sintered SOEC before operation, which was investigated by a combined approach involving EDX, MC and HR-STEM.

2.2.1. Inter-Diffusion at the YSZ/LSM Interface

Figure 3a displays an overview HAADF-STEM image recorded on a cross-sectional lamella of the electrolyte/electrode interface, prepared by a focused ion beam (FIB) inside an SEM. Simultaneously to the HAADF-STEM image, an EDX spectrum image was acquired. The elemental Mn and Zr distributions (based on the Mn-K and Zr-K line intensities) are shown in Figure 3b. The EDX maps at low magnification clearly

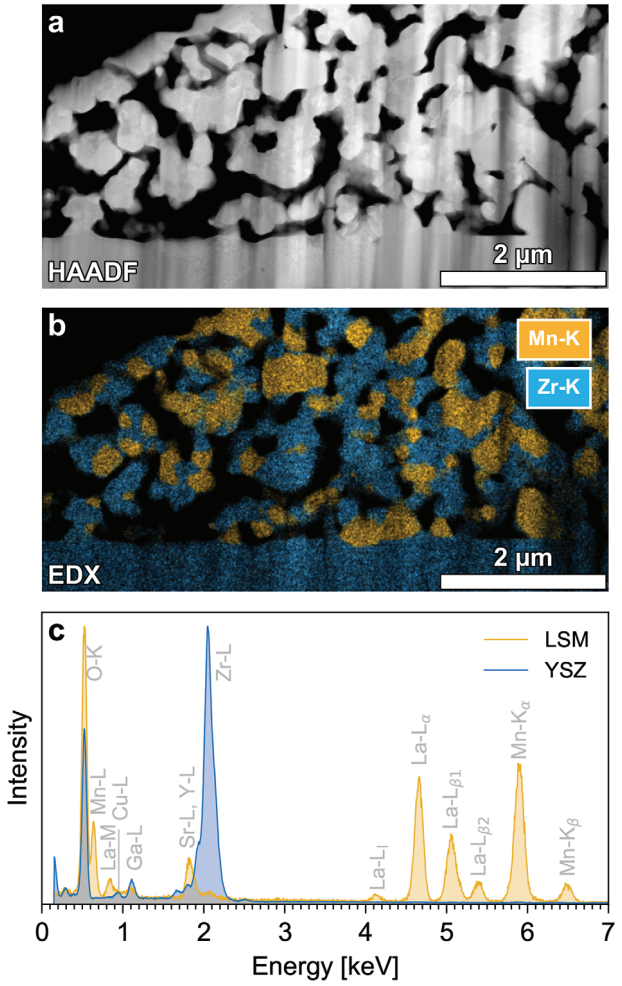

Figure 3. Morphology and elemental distribution in the screen-printed half cell after sintering (before operation). a) HAADF-STEM image of the interface between the 8YSZ electrolyte and the LSM + 8YSZ air electrode. b) Overlaid Mn-K and Zr-K intensity maps (EDX) from the region shown in (a). c) EDX spectra sampled from YSZ and LSM regions.

show well separated phases in the size range of approximately 0.5–1 µm, which are highlighted by the blue (Zr) and yellow (Mn) colors in Figure 3b. The respective spectra for the Zr-rich and Mn-rich phases are displayed in Figure 3c using the same color code as in the elemental distribution map in Figure 3b. The EDX spectra show signals of all expected elements that are present in LSM and YSZ. Intensity that stems from the Cu-L line arises from the copper lift-out grid on which the lamella is mounted. The Ga-L line is an artifact that stems from the FIB sample preparation.

The results from a high magnification EDX study are provided by **Figure 4**: Figure 4a shows a dark field STEM (DF-STEM) electron micrograph in which the LSM phase is on top of YSZ (see Figures S11 and S12, Supporting Information). The latter is oriented along the [110] axis in viewing direction, which results in Laue reflections in the Fourier plane, identified as 111, 112, and 002 (Figure 4a, red circles in the corresponding FFT image).[38] The elemental maps shown in Figure 4b include La, Sr, and Mn (reddish colors) and Y and Zr (blueish colors), in superimposed (left) and separated (middle and right) representation. At the grain boundary, elements from LSM intermix with elements from YSZ and an extended compositionally unique region (as indicated by white dashed lines and grey arrows, Figure 4b). These experimental findings were corroborated by MC simulations (see the Methods section for details). Values for the width of the intergranular layer derived from experiment and simulation are presented in Figure 4c. They agree very well except for La, which is discussed below. Further note that, in the case of Y, the amount of doping is too small for the size-limited simulation cell to obtain a fully reliable line profile. Supplementary details on the EDX quantification are presented in Figures S13 and S14, Supporting Information for experiment and simulation, respectively.

A more detailed view on the elemental distribution across the interface is given in Figure 4d by the corresponding elemental line profiles: the left panel shows the EDX signal across the interface for La, Sr, Mn, Y, and Zr. From these line profiles, an average inter-diffusion width of 1.25 nm was identified, indicated by grey arrows and the vertical lines. The middle panel in Figure 4d shows the simulated results, which, with an 1.34 nm average diffusion layer, are again qualitatively close to the experimental curves. As opposed to the experiment, a broadening of the La distribution close to the interface was observed in the simulation. This can be attributed to the high swapping probability of La with other atoms seen in the simulations. This happens especially often with Y (see Figure S15, Supporting Information), which leads to a distribution of La atoms beyond the interdiffusion region. As the employed MC approach samples thermodynamic probabilities, it is likely that the diffusion of large La cations into the regular oxygen lattice of YSZ is kinetically hindered and thus not seen as dominantly in the experiment.

The widths given in Figure 4c are represented by σ, the standard deviation of the normal cumulative distribution function used to fit the elemental profiles. Some additional long range diffusion of Mn into the YSZ region up to 35 nm was observed at different LSM/YSZ interfaces (Figure S16, Supporting Information), explaining the residual signal in the experimental profile in Figure 4d. This is in agreement with other works where Mn was shown to be prone to diffusion into the YSZ bulk.[17] Together with the structural characterization results in the next sections, the recurring compositional variations and matching widths at different locations (see Figure S17, Supporting Information) indicate that this distinct interfacial region can be classified as a complexion. Complexions are characterized by, for example, structural and compositional gradients, partial amorphization, and thermodynamic self-limitation.[31] The abundance of complexions found by TEM suggests that at all YSZ/LSM interfaces in the sample, a complexion is formed. Preliminary results of MC simulations at lower temperatures further indicate that the found complexion is an equilibrium structure, which is stable down to 300 K.

However, not all elements are present in this complexion: a systematic shift of 0.8 nm in the Sr signal (pink line) with respect to the other elements was found in the experimental as well as the simulated distributions. Consequently, it is the only element not contributing to the intergranular region, additionally acting as proof that the observed inter-diffusion is not the result of a sample preparation artifact since this would

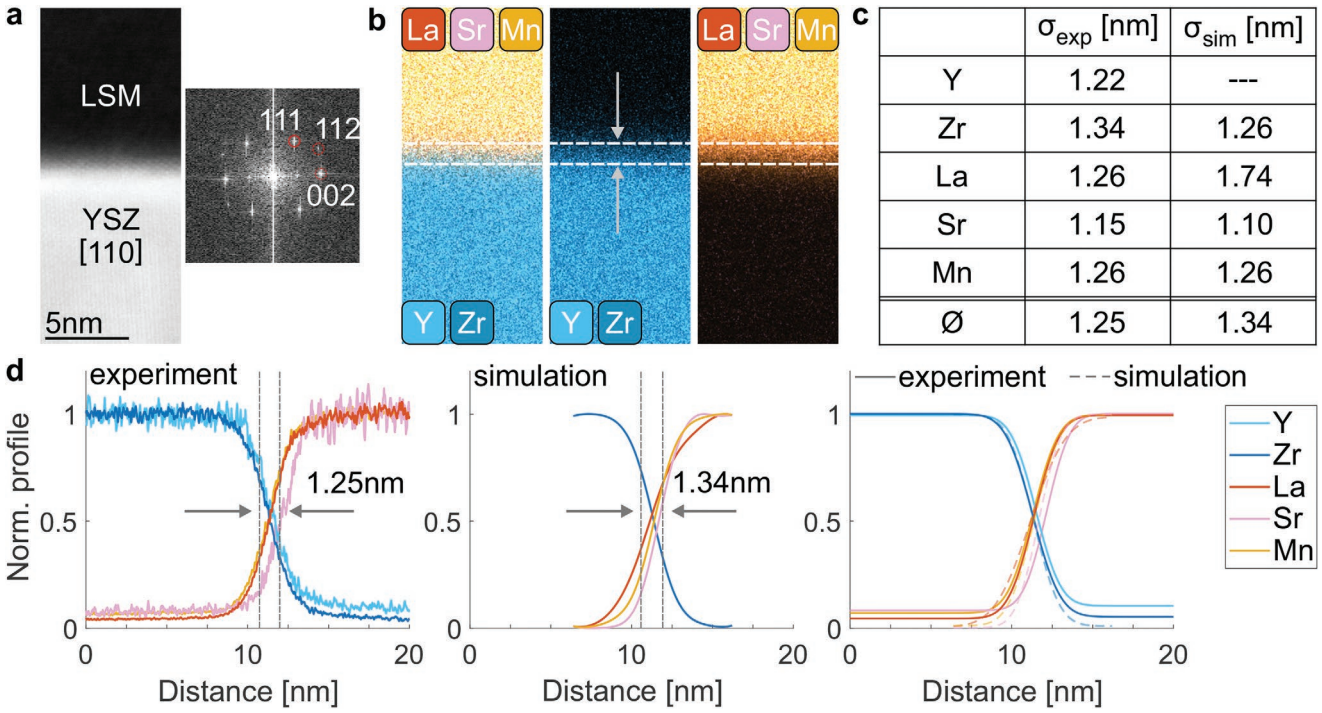

	σ_{exp} [nm]	σ_{sim} [nm]
Y	1.22	---
Zr	1.34	1.26
La	1.26	1.74
Sr	1.15	1.10
Mn	1.26	1.26
Ø	1.25	1.34

Figure 4. Inter-diffusion at the YSZ/LSM interface: a) DF-STEM image of YSZ/LSM interface, with YSZ oriented in a [110] zone axis (left), and corresponding Fourier-transformed image with reflexes highlighted by red circles, used for determining the [110] orientation of YSZ (right). b) EDX maps of elements as indicated by the insets, with LSM on top of YSZ. The dashed lines highlight the mixed LSM + YSZ inter-diffusion region. c) Experimental and simulated elemental spread across the YSZ/LSM interface. d) Experimental line profiles extracted from the EDX maps in (b) (left), simulated line profiles (middle), and comparison of fits (right) from experiment (solid) and simulation (dashed). The indicated values of 1.25 nm (experiment) and 1.34 nm (simulation) are the arithmetic mean of the values given in (c), with sigma being the standard deviation of the normal distribution function. Note the significant shift of Sr of approximately 0.8 nm with respect to all other elements.

be expected to lead to a uniform distribution of all elements. The absence of Sr at the YSZ/LSM interface has been reported before for a lower Sr doping.[20] However, no explanation for this observation could be given so far. The swapping probability as obtained by MC (compare Figure S15, Supporting Information) unveils that Sr, the largest cation within both oxides,[39] preferentially occupies large cuboctahedral sites (A-sites in the perovskite structure) of LSM. This suggests that, in contrast to the perovskite, a breakdown of large-sized anion polyhedra occurs at the inter-diffusion region, effectively forming a barrier for Sr that leads to a not fully stochastic distribution of ions.

This is supported by a more detailed analysis of the interfacial region, which indeed indicates a change of the cation coordination number in the complexion (compare Figure S18, Supporting Information). The reason for this is presumably the deformation of the [ZrO_8] oxygen cubes in YSZ to octahedra via a bicapped antiprism, as demonstrated in Figure S19, Supporting Information. This goes hand in hand with a decrease of the number of neighboring polyhedra for all cation environments and a change of the polyhedra connections (compare Figures S20 and S21, Supporting Information). The structure of the complexion is analyzed in further detail in the following.

2.2.2. Structure of the YSZ/LSM Interface

The complexion was further investigated structurally by atomically resolved HR-STEM. The high-resolution BF-STEM micrograph (Figure 5a, refer to Figure S23, Supporting Information for the corresponding HAADF-STEM image) displays the same YSZ/LSM electrolyte/electrode grain boundary that was investigated by STEM-EDX in Figure 4. YSZ is oriented along the [110] zone axis, as evidenced by the diamond-shaped distribution of Zr atoms. The corresponding projection of the YSZ crystal structure is presented in Figure S3, Supporting Information. The image is oriented such that the [001] axis is horizontal and the [$1\bar{1}0$] orientation points vertically towards the interface. A more detailed analysis is given in Figure S24, Supporting information, where the inset shows the template-matching-assisted average of several YSZ unit cells. The analysis clearly reveals the locations of O sites and the missing distortion of the oxygen lattice that would be characteristic for tetragonal zirconia.[38,40] This further corroborates the cubic structure as determined by XRD measurements (Figure S1c, Supporting Information). LSM appears in a high-index zone axis ([$\bar{1}35$], **Figure 5**a). Distinct atomic columns are absent, but lattice fringes attributed to {310} and {$2\bar{1}1$} planes can be observed.

In Figure 5b, spatially resolved 1D Fast Fourier Transforms (FFTs) along the [001] direction of YSZ are plotted, which were obtained from the BF-STEM image that is presented in Figure 5a (see Methods section for more details). While the x axis is in Fourier space (k, sampled along the [001] direction), the y axis of the FFT plot describes real space and is shared with the adjacent HR-STEM image. This semi-reciprocal plot shows strong signals in the YSZ phase (Figure 5b, bottom)

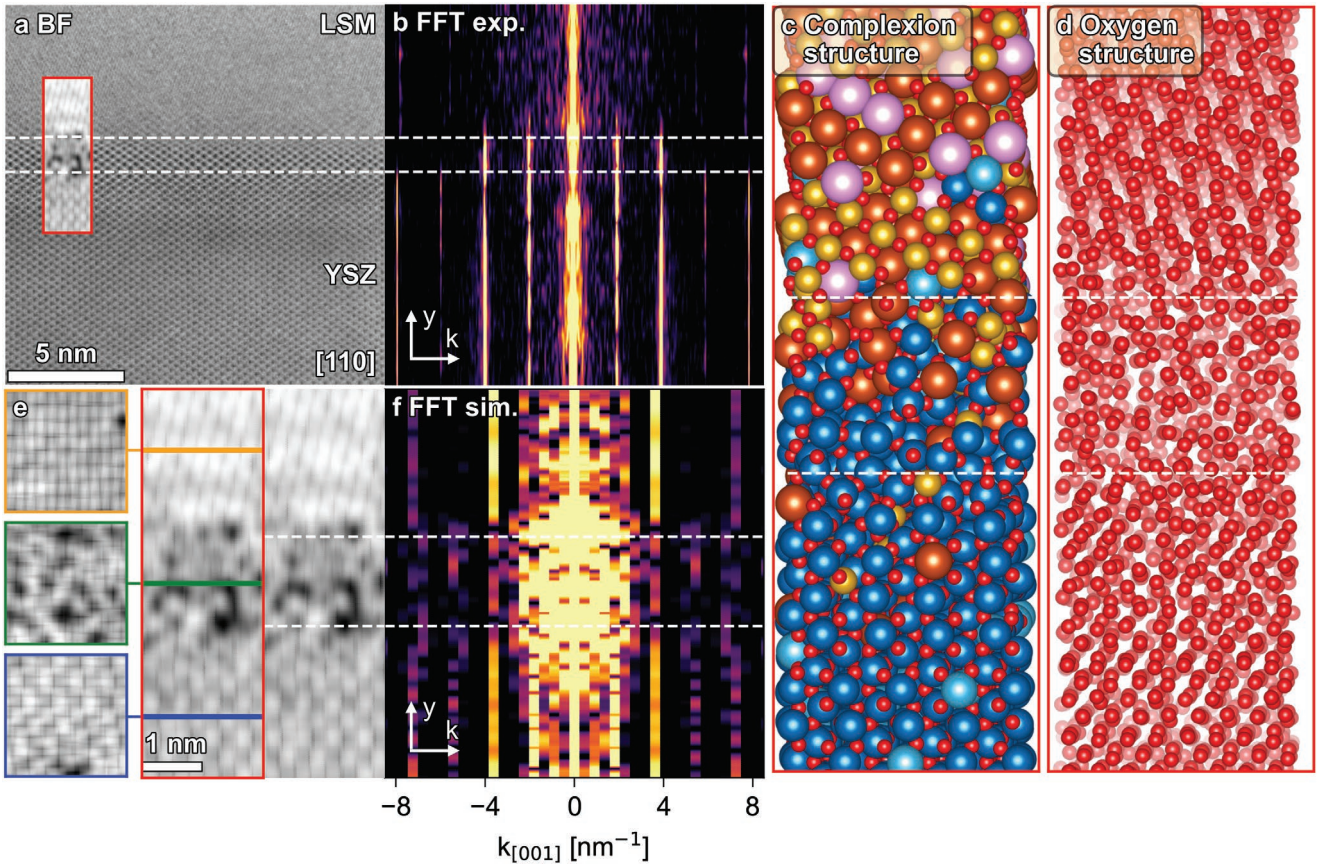

Figure 5. a) High-resolution BF-STEM image of the YSZ/LSM grain boundary with a superimposed cation density from the MC simulation (inset) in [110] zone axis. The white dashed lines enclose the area that is considered to belong to the complexion, based on the analysis in Figure S22, Supporting Information. b) Semi-reciprocal plot, that is, the spatially resolved Fourier Transform along the [001] direction (the *y* axis corresponds to the real space [$\bar{1}$10] axis of the micrographs and the *x* axis is shared with (f). c) View of the inset of (a) at atomic scale with La (bronze), Sr (pink), Mn (yellow), Zr (dark blue), Y (light blue), and O (red). d) Oxygen ions of the structure shown in (c). e) Cation density of the simulated interface (right, enlarged version of the inset in (a) and one repetition to show periodicity) with cuts through LSM (left, orange), the complexion (green) and YSZ (blue) that are orthogonal to the paper plane (and parallel to the interface plane). f) Corresponding Fourier Transform of the simulated 3D density with a representation analogous to (b).

and weaker reflections in the LSM phase (Figure 5b, top) due to the less resolved features owing to the high-index zone axis. However, approaching the YSZ/LSM grain boundary, the YSZ signals at high *k* values (about 6 and 8 nm^{-1}) disappear (Figure 5b, middle, dashed white lines), and only the peaks at 2 and 4 nm^{-1} remain, as also evident from the line profiles presented in Figure S22, Supporting Information. The loss of signals at high *k* can be understood as the loss of high index reflections due to reduction of long range order in the diffusion layer. As low index reflections at low *k* remain, short range order is still present. Thus, this points toward the formation of a less ordered/slightly amorphous structure on the YSZ side of the grain boundary.

Figure 5c shows the resulting grain boundary geometry according to the MC simulations. While LSM (top) and YSZ (bottom) both possess clear crystalline order, the diffusion layer appears more disordered and forms a structurally and compositionally distinct region between the two materials, denoted as complexion.[28] The loss of translational symmetry within the complexion is also evident when observing only the oxygen ions in the structure as they define the boundaries of the involved crystal structure. This is shown in Figure 5d. In order to analyze the amorphization of this layer, the corresponding cation density is mimicked by 3D Gaussian functions, whose 2D projection is given in Figure 5e (right). Additionally, cross-sectional cuts through the cation densities of LSM (yellow), YSZ (blue) and the complexion (green) are shown to provide a complete picture of the degree of crystallinity in all three dimensions. The corresponding windowed FFT of the 3D density of the simulated cell (f) is in good agreement with the experimental FFT. For YSZ (Figure 5e, bottom), the position of the signals agree with the experimental ones, although they are slightly lower as a result of the marginally stretched cell size needed for compliance with LSM. The peaks in the upper half of the graph result from LSM with a [$\bar{1}$35] surface termination. However, the LSM grain boundary orientation seems to be different from the experiment, as the few peaks that can be spotted are shifted. Nevertheless, the simulated FFT of the complexion qualitatively agrees with the experiment, indicating that the LSM interface orientation is not crucial for the characteristics of the formed complexion. Like in the experimentally determined FFT, signals at high *k* vanish at the complexion in Figure 5f, affirming that

long range order is lost, while the signals at low *k* from YSZ persists, which ascertains that some structure is retained for short to medium distances. Hence, the cations of the formed complexion preserve the short range structure of the YSZ phase, which can distinctly be seen in the BF-STEM image (Figure 5a). The loss of long range order derives from the disturbance of the oxygen ion lattice by the doping ions Mn and La, such that, in the complexion, many anions can be found aside defined crystal positions. This uneven framework of the oxygen atoms in turn causes distortion of the cation positions, leading to a slight amorphization of the phase and the loss of large cation sites which are typical for the perovskite-structured LSM.

2.2.3. Complexion Classification

Earlier reports did not classify this transitional region as a complexion. For tetragonal 3YSZ (i.e., YSZ with 3mol% of yttria) and LSM, the interface has previously been interpreted as a nanometer-wide solid solution with strong lattice distortion on the YSZ side of the interface with particular chemistry.[19,20] The suggested formation of solid solutions, for which Y^{3+}, La^{3+} or Mn cations can be homogeneously dispersed in zirconia, should only lead to a slight relaxation of atomic positions, whereas the complexion observed here undergoes such a strong deformation that crystallographic reflections are lost. This is especially pronounced in the oxygen positions in Figure 5d. The high degree of disorder caused by the diffusion-induced doping and the resulting loss of long range order suggests that this cannot be classified as a solid solution. On the other hand, it also cannot be referred to as an interphase since, based on the amorphization of the oxygen lattice in the inter-diffusion layer, thermodynamic stability as an extended 3D phase without the confining bulk phases is highly unlikely. Additionally, the stoichiometric variations introduced by the cross-diffusion do not satisfy the definition of the term "phase". However, in addition to other properties discussed in the following, partial amorphization and compositional gradients at the interface are characteristic features of complexions.[30,31]

Thus, in contrast to the previously proposed models of the YSZ/LSM interface, the results presented here, for the first time, reveal that considering the concept of complexion formation is necessary as it does not only explain the general structural and compositional appearance, but also the strong variation of the chemical properties at the YSZ/LSM boundary compared to the respective bulk phases that have also been observed for similar interfaces.[32]

The investigated complexion is characterized by compositional and structural profiles which deviate from either of the neighboring LSM and YSZ phases distinctively. Structural changes are necessitated by the fact that the anion is the mobile species in the less rigid solid ion conductor YSZ, which forms a contact with the robust, perovskite-structured and electronically conducting LSM by structurally adjusting over a finite width. The thermodynamic driving force for this might be seen in a frustrated phase transformation where the complexion resembles a kinetically trapped intermediate or precursor state on the way to the formation of the undesired pyrochlore $La_2Zr_2O_7$, which is known to be formed if the material is sintered at too high temperatures.[41–43] Alternatively, it is also known that LSM is less prone to pyrochlore formation than, for example, cobalt- and iron-based perovskites,[44] and exhibits a higher electrocatalytic stability than those materials.[45] Both of these properties might have their origin in the presence of this complexion.

The width of a complexion is self-limited and dependent on various intrinsic and extrinsic factors such as surface orientation, temperature, pressure and applied potential.[31,46–48] It was shown here that a complexion is formed at every investigated YSZ/LSM interface during the thermal sintering process; however, their individual thicknesses vary depending on the local conditions. In fact, the disorder at the electrochemically sintered interfaces seen in the high-resolution TEM images by He et al.[17,18] may also be interpreted as a complexion, supporting our conjecture that this is a pervasive phenomenon at sintered YSZ/LSM interfaces. As evident from analysis of the disordered region in Figure S22, Supporting Information, the complexion observed in Figure 5 spans approximately four atomic layers (1.47 nm), which classifies as multilayer in Dillon-Harmer nomenclature.[28] However, in contrast to the strongly amorphous multi-layer complexions in alumina, the retained structural order in YSZ/LSM corresponds more to the bi- or trilayer structures, illustrating that complexion characteristics are also very material-specific.

In all experimentally probed sample regions, the thicknesses of all grain boundaries are similar (compare Figure S17, Supporting Information). This is in agreement with the thermodynamic control of complexion formation, whereas, in the kinetic regime of a non-self-limited layer, a significantly higher variety of complexion thicknesses would be expected. However, the thermodynamic stability of the complexion under reaction conditions remains unclear as defects, such as the distortions of the anionic lattice shown in Figure 5 can act as kinetic barriers as well. On the other hand, the thermodynamical self-limited width is also observed in the simulations (see Figure 4 and Figure S25, Supporting Information for different interface terminations), where complexion growth is limited in the approached thermodynamic minimum. Comparing the two simulations, the sensitivity of complexion properties such as width and degree of amorphization on the confining bulk lattice orientation can also be observed.

The dependence of the form of complexions on multiple parameters implies that their properties correlate with various conditions that can be controlled experimentally. Knowing the relationship between relevant complexion features and adjustable parameters thus allows the selective tuning of relevant complexion properties such that a beneficial influence of the complexion on the active phase activity can be achieved. Identifying these correlations and connecting the impact of the complexion characteristics to the TPB under working conditions requires a detailed operando study, designated to link complexion properties to cell performance. With the aid of theoretical models, a further link to intrinsic characteristics of the different complexion categories such as ionic and electronic conductivity can also be established. This ultimately compiles to the creation of a YSZ/LSM complexion phase diagram and property map that enables finding the optimal operation conditions to enhance the performance and lifetime of solid oxide cells.

Beyond the questions whether the YSZ/LSM complexion constitutes a mixed ionic/electronic conductor that can supply the reactive centers at the surface of the TPB with the charged reactants from "underneath", it is of paramount importance to establish the structure of the living catalytic TPB surface under operating conditions. A legitimate path would be to follow the general assumption of surface science that the native and active catalyst surface is derived from the underlying structure of the bulk. In the present case, it would be expressed by the structure of the YSZ/LSM complexion. However, for metal oxides, it is known that the surface structure can differ substantially from the underlying bulk.[49–51] Further modifications are induced in the surface and sub-surface layers due to varying chemical potentials of the gas phase species that are in contact with the outermost layer of this complexion at elevated temperatures. As the electric and ionic conductivity of the complexion remains unknown, it will be important to know how this 2D surface termination contributes to the appearance and function of the expected one-dimensional TPB.

These intricate new questions of structural and compositional variability along two orthogonal dimensions, i.e. vertical solid/gas and lateral YSZ/LSM, require spatially resolved operando experiments. For operando TEM experiments, atomic resolution is possible,[52] although a spatially resolved SOEC/SOFC operando investigation would require new cell developments that allow for realistic measurements. Even so, it remains questionable whether the observed atomic description of the surface structure that may be observed under operando conditions is relevant or significant. For instance, high-resolution imaging requires a high electron density. For operando experiments, it is, thus, impossible to disentangle between reaction-, electron beam-, and radical-induced surface structures, i.e. when the electron beam interacts with the gas phase.[53] This example shows that spatially resolved operando techniques alone may be of limited use and should be complemented by quasi in situ imaging approaches and theory.[54–56]

3. Conclusion

By unraveling a complexion structure at the electrolyte/electrode interface of SOECs/SOFCs at the atomic scale, we have paved the way to a more realistic picture of solid oxide cells and their functionality. Driven by significant inter-diffusion of all cations except for Sr, a break-down of the oxygen lattice (see Figure 5d and Section S4.2, Supporting Information) leads to the formation of this complexion in a sintered, yet unoperated cell, that is, a thermodynamically stable, nanometer-sized intergranular layer of reduced long-range order, which was observed by experiment and theory at all investigated interfaces.

The inclusion of finite structures such as complexions in the classically simplified model of an atomically sharp interface is an important extension with immediate impact on the appearance and performance of the active surface area. We also expect it to be a powerful concept for chemical interface engineering toward more active and long-lived cells.

Supporting Information

Supporting Information is available from the Wiley Online Library or from the author.

Acknowledgements

This work was supported by the Deutsche Forschungsgemeinschaft (DFG, German Research Foundation) under the priority programme SPP 2080 DynaKat. T. Götsch additionally acknowledges funding by the Fonds zur Förderung der wissenschaftlichen Forschung (FWF, Austrian Science Fund) via project number J4278. F.-P. Schmidt acknowledges funding by the Deutsche Forschungsgemeinschaft (DFG, German Research Foundation) – 388390466 – TRR 247. Moreover, this work was partially funded by the Deutsche Forschungsgemeinschaft (DFG, German Research Foundation) under Germany's Excellence Strategy — EXC 2089/1 — 390776260. The authors acknowledge the Helmholtz-Zentrum Berlin für Materialien und Energie for allocating beam time within proposal number 201-09080CR. Additionally, the authors thank V. Vibhu for preparation of the electrodes. Correction added on 23 August 2021, after first online publication: Projekt Deal funding statement has been added.

Open access funding enabled and organized by Projekt DEAL.

Conflict of Interest

The authors declare no conflict of interest.

Author Contributions

H.T., F.-P.S., and T.G. contributed equally to this work. H.T., F.-P.S., and T.G. have performed the main experiments/calculations and their analysis and have written the majority of the manuscript. F.G. has conducted the XRD experiments and analyses and contributed to the crystallographic discussions. A.H. and D.I. have prepared the TEM specimens and have acquired and interpreted the SEM images. I.C.V. and L.G.J.d.H. designed the electrodes and provided expertise. A.K.-G., C.S., and T.L. have supervised the experiments/simulations and discussions and have contributed in writing the manuscript. R.-A.E., K.R., and R.S. provided perspectives and acquired funding.

Data Availability Statement

The data that support the findings of this study are available from the corresponding author upon reasonable request.

Keywords

electron microscopy, electrolyte/electrode interfaces, fuel cells, molecular modeling

Received: June 10, 2021
Revised: July 9, 2021
Published online: August 21, 2021

[1] M. Ni, M. Leung, D. Leung, *Int. J. Hydrogen Energy* **2008**, *33*, 2337.
[2] Q. Cai, C. S. Adjiman, N. P. Brandon, *J. Power Sources* **2014**, *268*, 212.
[3] R. M. Ormerod, *Chem. Soc. Rev.* **2003**, *32*, 17.
[4] A. J. Jacobson, *Chem. Mater.* **2010**, *22*, 660.

[5] A. Atkinson, S. Barnett, R. J. Gorte, *Nat. Mater.* **2004**, *3*, 17.
[6] M. S. Sohal, J. E. O'Brien, C. M. Stoots, V. I. Sharma, B. Yildiz, A. Virkar, *J. Fuel Cell Sci. Tech.* **2012**, *9*, 011017.
[7] K. Chen, S. P. Jiang, *J. Electrochem. Soc.* **2016**, *163*, F3070.
[8] M. Tahir, L. Pan, F. Idrees, X. Zhang, L. Wang, J.-J. Zou, Z. L. Wang, *Nano Energy* **2017**, *37*, 136.
[9] L. Han, S. Dong, E. Wang, *Adv. Mater.* **2016**, *28*, 9266.
[10] M. C. Brant, T. Matencio, L. Dessemond, R. Z. Domingues, *Solid State Ion.* **2006**, *177*, 915.
[11] T. Matsui, Y. Mikami, H. Muroyama, K. Eguchi, *J. Power Sources* **2013**, *242*, 790.
[12] S. J. Kim, J. Y. Koo, T. Mun, M. Choi, W. Lee, *J. Mater. Chem. A* **2020**, *8*, 23313.
[13] M. Keane, M. K. Mahapatra, A. Verma, P. Singh, *Int. J. Hydrogen Energy* **2006**, *37*, 16776.
[14] Y. L. Liu, A. Hagen, R. Barfod, M. Chen, H. J. Wang, F. W. Poulsen, P. V. Hendriksen, *Solid State Ion.* **2009**, *180*, 1298.
[15] T. Horita, T. Tsunoda, K. Yamaji, N. Sakai, T. Kato, H. Yokokawa, *Solid State Ion.* **2002**, *152-153*, 439.
[16] M. Kuznecov, P. Otschik, P. Obenaus, K. Eichler, W. Schaffrath, *Solid State Ion.* **2003**, *157*, 371.
[17] S. He, K. Chen, M. Saunders, J. Li, C. Q. Cui, S. P. Jiang, *J. Electrochem. Soc.* **2017**, *164*, F1437.
[18] S. He, K. Chen, M. Saunders, Z. Quadir, S. Tao, J. T. Irvine, C. Q. Cui, S. P. Jiang, *Solid State Ion.* **2018**, *325*, 176.
[19] M. Backhaus-Ricoult, M. Badding, J. Brown, M. Carson, E. Sanford, Y. Thiaul, *Developments in Solid Oxide Fuel Cells Lithium Ion Batteries* **2005**, 21–30.
[20] M. Backhaus-Ricoult, *Solid State Ionics* **2006**, *177*, 2195.
[21] M. Backhaus-Ricoult, K. Adib, T. St Clair, B. Luerssen, L. Gregoratti, A. Barinov, *Solid State Ionics* **2008**, *179*, 891.
[22] Y. Chen, Y. Fan, S. Lee, G. Hackett, H. Abernathy, K. Gerdes, X. Song, *J. Power Sources* **2019**, *438*.
[23] S. He, S. P. Jiang, *Prog. Nat. Sci. Mater. Int.* **2021**, https://doi.org/10.1016/j.pnsc.2021.03.002.
[24] S. N. Rashkeev, M. V. Glazoff, *Int. J. Hydrogen Energy* **2012**, *37*, 1280.
[25] J. A. Kilner, R. A. De Souza, I. C. Fullarton, *Solid State Ionics* **1996**, *86-88*, 703.
[26] P. S. Manning, J. D. Sirman, J. A. Kilner, *Solid State Ionics* **1997**, *93*, 125.
[27] S. B. Adler, X. Y. Chen, J. R. Wilson, *J. Catal.* **2007**, *245*, 91.
[28] S. J. Dillon, M. Tang, W. C. Carter, M. P. Harmer, *Acta Mater.* **2007**, *55*, 6208.
[29] J. Luo, *Crit. Rev. Solid State Mater. Sci.* **2007**, *32*, 67.
[30] P. R. Cantwell, M. Tang, S. J. Dillon, J. Luo, G. S. Rohrer, M. P. Harmer, *Acta Mater.* **2014**, *62*, 1.
[31] J. Luo, *Energy Storage Mater.* **2019**, *21*, 50.
[32] J. Timmermann, F. Kraushofer, N. Resch, P. Li, Y. Wang, Z. Mao, M. Riva, Y. Lee, C. Staacke, M. Schmid, C. Scheurer, G. S. Parkinson, U. Diebold, K. Reuter, *Phys. Rev. Lett.* **2020**, *125*, 206101.
[33] J. Rodríguez-Carvajal, M. Hennion, F. Moussa, A. H. Moudden, L. Pinsard, A. Revcolevschi, *Phys. Rev. B* **1998**, *57*, R3189.
[34] X. Qiu, T. Proffen, J. F. Mitchell, S. J. Billinge, *Phys. Rev. Lett.* **2005**, *94*, 1.
[35] T. Grande, J. R. Tolchard, S. M. Selbach, *Chem. Mater.* **2012**, *24*, 338.
[36] R. J. D. Tilley, *Perovskites: Structure-Property Relationships*, John Wiley & Sons, Ltd, Chichester, UK **2016**.
[37] T. Götsch, L. Schlicker, M. F. Bekheet, A. Doran, M. Grünbacher, C. Praty, M. Tada, H. Matsui, N. Ishiguro, A. Gurlo, B. Klötzer, S. Penner, *RSC Adv.* **2018**, *8*, 3120.
[38] H. Horiuchi, A. J. Schultz, P. C. Leung, J. M. Williams, *Acta Crystallogr. Sect. B* **1984**, *40*, 367.
[39] R. D. Shannon, *Acta Cryst.* **1976**, *A32*, 751.
[40] B. Bondars, G. Heidemane, J. Grabis, K. Laschke, H. Boysen, J. Schneider, F. Frey, *J. Mater. Sci.* **1995**, *30*, 1621.
[41] K. Yang, J. H. Shen, K. Y. Yang, I. M. Hung, K. Z. Fung, M. C. Wang, *J. Power Sources* **2006**, *159*, 63.
[42] J. A. Labrincha, J. R. Frade, F. M. Marques, *J. Mater. Sci.* **1993**, *28*, 3809.
[43] A. Chen, J. R. Smith, K. L. Duncan, R. T. DeHoff, K. S. Jones, E. D. Wachsman, *J. Electrochem. Soc.* **2010**, *157*, B1624.
[44] W. Wang, Y. Huang, S. Jung, J. M. Vohs, R. J. Gorte, *J. Electrochem. Soc.* **2006**, *153*, A2066.
[45] A. Neumann, M. N. H. I. Vinke, H. Lippert, *ECS Trans.* **2009**, *25*, 2889.
[46] K. S. Vikrant, R. E. García, *npj Comput. Mater.* **2019**, *5*, 1.
[47] P. R. Cantwell, T. Frolov, T. J. Rupert, A. R. Krause, C. J. Marvel, G. S. Rohrer, J. M. Rickman, M. P. Harmer, *Annu. Rev. Mater. Res.* **2020**, *50*, 465.
[48] J. Nie, C. Hu, Q. Yan, J. Luo, *Nat. Commun.* **2021**, *12*, 1.
[49] L. Masliuk, F.-P. Schmidt, W. Hetaba, M. Plodinec, G. Auffermann, K. Hermann, D. Teschner, F. Girgsdies, A. Trunschke, R. Schlögl, T. Lunkenbein, *J. Phys. Chem. C* **2020**, *124*, 23069.
[50] X. Li, T. Lunkenbein, V. Pfeifer, M. Jastak, P. K. Nielsen, F. Girgsdies, A. Knop-Gericke, F. Rosowski, R. Schlögl, A. Trunschke, *Angew. Chemie Int. Ed.* **2016**, *55*, 4092.
[51] K. Reuter, *Catal. Letters* **2016**, *146*, 541.
[52] M. Plodinec, H. C. Nerl, F. Girgsdies, R. Schlögl, T. Lunkenbein, *ACS Catal.* **2020**, *10*, 3183.
[53] M. Boniface, M. Plodinec, R. Schlögl, T. Lunkenbein, *Top. Catal.* **2020**, *63*, 1623.
[54] L. Masliuk, M. Swoboda, G. Algara-Siller, R. Schlögl, T. Lunkenbein, *Ultramicroscopy* **2018**, *195*, 121.
[55] S. Janbroers, J. N. Louwen, H. W. Zandbergen, P. J. Kooyman, *J. Catal.* **2009**, *268*, 235.
[56] S. Stegmaier, R. Schierholz, I. Povstugar, J. Barthel, S. P. Rittmeyer, S. Yu, S. Wengert, S. Rostami, H. Kungl, K. Reuter, R. A. Eichel, C. Scheurer, *Adv. Energy Mater.* **2021**, *11*, 2100707.

Paper 2

Sr Surface Enrichment in Solid Oxide Cells - Approaching the Limits of EDX Analysis by Multivariate Statistical Analysis and Simulations

Hanna Türk, Thomas Götsch, Franz-Philipp Schmidt, Adnan Hammud, Danail Ivanov, L.G.J. (Bert) de Haart, Izaak C. Vinke, Rüdiger-A. Eichel, Robert Schlögl, Karsten Reuter, Axel Knop-Gericke, Thomas Lunkenbein, and Christoph Scheurer,

ChemCatChem **2022**, *14*, e202200300.

ChemCatChem

Research Article
doi.org/10.1002/cctc.202200300

Chemistry Europe
European Chemical Societies Publishing

www.chemcatchem.org

Special Collection

Sr Surface Enrichment in Solid Oxide Cells – Approaching the Limits of EDX Analysis by Multivariate Statistical Analysis and Simulations

Hanna Türk,[a, b] Thomas Götsch,[a] Franz-Philipp Schmidt,[a] Adnan Hammud,[a] Danail Ivanov,[a] L. G. J. (Bert) de Haart,[c] Izaak C. Vinke,[c] Rüdiger-A. Eichel,[c, d] Robert Schlögl,[a, e] Karsten Reuter,[a] Axel Knop-Gericke,[a, e] Thomas Lunkenbein,*[a] and Christoph Scheurer*[a]

In solid oxide cells, Sr segregation has been correlated with degradation. Yet, the atomistic mechanism remains unknown. Here we begin to localize the origin of Sr surface nucleation by combining force field based simulations, energy dispersive X-ray spectroscopy (EDX), and multi-variate statistical analysis. We find increased ion mobility in the complexion between yttria-stabilized zirconia and strontium-doped lanthanum manganite. Furthermore, we developed a robust and automated routine to detect localized nucleation seeds of Sr at the complexion surface. This hints at a mechanism originating at the complexion and requires in-depth studies at the atomistic level, where the developed routine can be beneficial for analyzing large hyperspectral EDX datasets.

Introduction

Solid oxide cells (SOCs), including solid oxide fuel cells (SOFCs) and solid oxide electrolysis cells (SOECs) are becoming increasingly important due to their relatively high energy conversion efficiencies of up to 85 %.[1,2] This makes solid oxide cells a valuable element to complement the modern energy infrastructure by providing chemical storage capacities for excess energy that temporarily arises due to the intermittent nature of renewable energy sources such as wind or solar power.[3]

The wide-spread adoption of these cells is currently hindered primarily by a fast degradation of the anode in electrolysis mode. This electrode is responsible for the oxygen evolution reaction (OER).[4,5] It is believed that oxygen evolution occurs at the triple phase boundary (TPB) where the oxygen-ion-conducting electrolyte (usually yttria-stabilized zirconia, YSZ), the electron-conducting electrode (often a perovskite, here lanthanum strontium manganite, LSM) and the gas phase meet.[6–8] While the location of this point is defined by indispensable properties to allow the OER to proceed, e.g. having sufficiently high oxygen ion and electron conductivity, the point itself, however, remains an elusive concept that has never been directly observed so far. Elucidating the structure of the TPB and its thermodynamic stability is crucial to identify the relevant aging process within the plethora of proposed deactivation mechanisms.[9] Besides poisoning[5] and electrode delamination caused by internal oxygen partial pressure[4,10–12] or YSZ electroreduction,[13] cation (Sr and Mn) migration is believed to play a key role in electrode deactivation. It is responsible for interfacial reactions,[14–18] nanocluster formation,[19] structural damages,[20] loss of electronic conductivity in LSM[21–24] and active site blockage by the respective oxides as well as subsequent surface reactions of the cations with volatile species.[17,22,23,25–27]

Already in the early stages of SOFC development at FZ Jülich,[28,29] an A-site deficient LSM composition was selected, because in combination with the YSZ electrolyte this composition is less susceptible to the undesired formation of a $La_2Zr_2O_7$ interlayer during sintering of the LSM electrode layer at

[a] H. Türk, Dr. T. Götsch, Dr. F.-P. Schmidt, A. Hammud, D. Ivanov, Prof. R. Schlögl, Prof. K. Reuter, Dr. A. Knop-Gericke, Dr. T. Lunkenbein, Dr. C. Scheurer
Fritz-Haber-Institut der Max-Planck-Gesellschaft
Faradayweg 4–6, 14195 Berlin (Germany)
E-mail: lunkenbein@fhi.mpg.de
scheurer@fhi.mpg.de
[b] H. Türk
Chair for Theoretical Chemistry and Catalysis Research Center
Department of Chemistry
Technische Universität München
Lichtenbergstraße 4, 85748 Garching (Germany)
[c] Dr. L. G. J. (Bert) de Haart, Dr. I. C. Vinke, Prof. R.-A. Eichel
Forschungszentrum Jülich GmbH
Institute of Energy and Climate Research
Fundamental Electrochemistry (IEK-9)
Wilhelm-Johnen-Straße, 52428 Jülich (Germany)
[d] Prof. R.-A. Eichel
RWTH Aachen University
Institute of Physical Chemistry
Landoltweg 2, 52074 Aachen (Germany)
[e] Prof. R. Schlögl, Dr. A. Knop-Gericke
Max Planck Institute for Chemical Energy Conversion
Department of Heterogeneous Reactions
Stiftstraße 34–36, 45470 Mülheim an der Ruhr (Germany)

Supporting information for this article is available on the WWW under https://doi.org/10.1002/cctc.202200300

Special Collection

This publication is part of a joint Special Collection with ChemElectroChem on "Catalysts and Reactors under Dynamic Conditions for Energy Storage and Conversion (DynaKat)". Please check our homepage for more articles in the collection.

elevated temperatures (1250 to 1350 C).[30–32] Further segregation mitigation strategies include nanoparticle infiltration[33] and anode[34] and microstructure[35] design to suppress high oxygen partial pressure[36] and anodic polarization,[20] which have been proposed to drive this phenomenon. Even though these strategies have shown promising results, cation segregation, especially of Sr, continues to impact cell performance, as the absence of fundamental understanding on the atomistic level prevents its systematic control.[37,38]

Previously,[39,40] we have shown that a so-called complexion is formed between the typical components of the cell, i.e. the YSZ electrolyte and the LSM anode. In brief, a complexion is a thermodynamically stable intergranular layer of self-limited width that is only stable in between two bulk phases.[41,42] Complexions have already been found in a variety of different functional solids.[43–48] Such a complexion can exhibit properties different from their neighboring phases. For SOCs, many of these properties are not yet identified or understood. For instance, it may be a mixed ionic and electronic conductor (MIEC),[39] which would ideally increase the size of the location of oxygen evolution from a 1-dimensional (1D) line to a 2D complexion/gas area containing the active sites if it extends unperturbed to the surface. In reality, however, the surface structure and composition of oxides differs from the underlying bulk.[49,50]

In the present study, we aim at assessing the composition of the surface termination of the complexion by combining simulation and experiment. Therefore, the manuscript is hierarchically structured and we first take a closer look at the chemical properties inside the complexion by evaluating molecular dynamics simulations to understand spatially resolved ion mobilities. We found a variation of the oxygen ion diffusion within the complexion compared to the neighboring bulk phases. Second, we investigated the cation mobility in this partially amorphous layer and predict a stable surface composition of the complexion by Monte Carlo (MC) simulations. The evolution of the elemental distribution towards the complexion surface was investigated emphasizing the role of strontium cations, which were previously found to be almost absent from the unperturbed complexion. It was found that the elemental profile associated with Sr across the complexion was shifted significantly compared to all other elements.[39] Experimentally, we employ energy-dispersive X-ray (EDX) spectrum images in a (scanning) transmission electron microscope ((S)TEM) for aged samples (150 h at 1073 K). In addition, complementary synchrotron-based X-ray photoelectron spectroscopy (XPS) measurements were performed for the aged and the pristine samples (1423 K for 1 h).

The detection of small, local (i.e. sub-nanometer) variations in the elemental distribution represents a key challenge when it comes to low concentration elements. STEM-based EDX is a well-suited technique to study such local variations due to its high spatial resolution given by the focused electron probe. However, the limited collection efficiency of the generated X-rays leads to high noise levels hindering a clear interpretation of potential changes in the elemental distribution. This can become problematic if the respective elemental concentrations drops below 5 at%, which holds also for the Sr content within the LSM used in this study ($(La_{0.8}Sr_{0.2})_{0.95}MnO_{3-\delta}$). Within the complexion,[39] the Sr content is further reduced to below 2 at%. Although there has been a huge progress within the last decade to increase the X-ray detection efficiencies, the measurement of minute variations of a small amount of an element at the sub-nm scale remains still challenging.

To overcome this dilemma we here apply a novel approach that consists of four steps: (1) We have optimized the acquisition procedure to obtain the best trade-off between high signal and low/no beam damage. (2) We performed a post-acquisition sample drift correction and (3) utilized multivariate statistical analysis (MSA)[51–56] by applying non-negative matrix factorization (NMF).[57,58] (4) Welch's t-testing was finally employed to evaluate an increase or decrease of the Sr content along the complexion towards a potential TPB.

In general, MSA is used to find inference of more than two variables in empirical datasets.[59,60] Besides many other fields, it has successfully been applied in medicine[61,62] and biology.[63] In electron microscopy, the main application of dimensionality reduction by MSA is denoising of spectra, often by principal component analysis (PCA).[64,65] However, these methods are increasingly also used to decompose hyperspectral stacks obtained from spectrum imaging in order to extract different, also overlapping, components from EDX or electron energy-loss (EEL) spectra. This can be used to map different phases that are non-trivial to distinguish spectroscopically.[66–68]

The Sr variations are additionally investigated by means of XPS, which enables the comparison of surface to sub-surface ("bulk") Sr content. It further allows the analysis of its chemical nature. However, being a spatially integrative technique with much worse lateral resolution compared to EDX and Sr segregation has also been shown for pure perovskites,[69] the sample was carefully polished in order to expose as many complexion/vacuum interfaces as possible to the X-ray beam.

Results and Discussion

Simulation

Ion diffusion

For OER, oxygen ion and electronic conductivity around the active phase is essential as it determines the availability of O^{2-} at the recombination zone. In addition, the concept of TPB may be supported by the presence of a complexion, albeit by a possible higher dimensionality. Complexions can have different properties compared to their confining bulk phases, e.g. partial amorphization and compositional gradients.[46] We focus here on the ion transport properties within the complexion which has not been investigated until now.

We performed molecular dynamics (MD) simulations to assess the ion mobility along the complexion. Figure 1 shows the extracted diffusion coefficients of all ionic species for several relevant temperatures. At each temperature, the total ion mobility is significantly increased within the complexion as

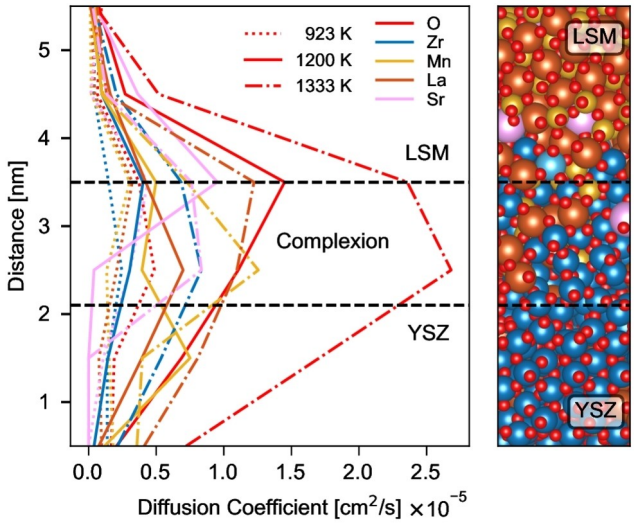

Figure 1. (left) Diffusion coefficients of different ions across the complexion at different temperatures (dotted lines: 923 K, solid: 1200 K and dash dotted: 1333 K). The dashed black lines enclose the complexion. (right) Exemplary excerpt of one complexion with its confining bulk phases. The color code of the elements is the same as for the diffusion, Y is highlighted in light blue.

compared to the bulk phases. This effect is most pronounced for the oxygen anions, suggesting a more than three-times increase of the ion mobility as compared to the adjacent YSZ bulk phase. Such an enhancement of oxygen ion conductivity has been reported before for LSM grain boundaries,[70] which was attributed to the high density of oxygen vacancies in this area. In our case the observed high oxygen ion mobility may stem from a reduced density as a consequence of the partial amorphization of the complexion. According to the simulations, the oxygen density in the complexion yields only 83.1% and 83.3% of the one of LSM and YSZ, and the total mass density is reduced to 78.4% of the LSM bulk and 98.6% of the YSZ (compare Table S1 in the SI for density values). Note that the bulk density values are, due to simulation cell size limitations, extracted only a few nanometers away from the complexion and thus can still be influenced by it. This reduced density in the complexion could open space for oxygen diffusion and facilitate ion movement. The enhancement of oxygen ion mobility might be considered an intrinsic property of grain boundaries and complexions in ion conducting host materials as long as free oxygen sites are available. The high oxygen mobility within the complexion may be important for the function of the SOEC to maintain a steady surface oxygen supply and to regulate the oxidation states of the surface metals.

Remarkably, not only the oxygen ion mobility is considerably enhanced in the area of the complexion, but also the cations become fairly mobile within the complexion. However, a high cation mobility could enhance segregation and thus lead to irreversible restructuring effects. This poses the question whether the elemental composition within the complexion as established during the sintering process is stable during the prevailing time of the operation, in particular in the vicinity of the active surface. In reality the LSM/YSZ interface is multiplied in a porous layer of approximately 25 μm thickness, which exposes several active areas to the gaseous environment.[39] In order to obtain a realistic thermodynamic equilibrium model from infinite simulation slabs, covering not only a complexion between the two adjacent oxide phases but also the exposed active surface, we cut a rectangular hole through this arrangement (see SI Figure S1). This may facilitate the exploration of compositional restructuring, which could be a reason for the fast anode degradation.

Complexion surface termination

To assess this question, we simulated sintering and thermal aging by an MC approach for an ensemble of model cells containing surfaces exposed to vacuum that cut across the complexion to study the evolution of the surface composition of the complexion at an atomistic level. The top and side views of the complexion/vacuum interface for one exemplary cell after convergence of the MC simulation are shown in Figure 2a and b. The simulations show that the Sr ions (pink) are accumulating on this surface in the vicinity of the complexion in the form of an oxide.

To quantify this effect, Figure 2c features the ensemble averaged elemental profiles along the complexion up to the vacuum interface. While oxygen and zirconium do not show a notable gradient from the complexion bulk towards the surface, Mn and Sr seem to significantly supplant La within the nanometer, which is closest to the surface. In comparison to Zr and O, this effect is the strongest for Sr, where the elemental profile is even shifted slightly towards the surface, whereas for La and Mn the profiles' points of inflection are shifted towards the bulk region of the complexion. While the general phenomenon of Mn[71–73] and Sr[7,24–26,73–77] surface segregation in LSM has been reported for various conditions and doping concentrations, Sr segregation has even been linked to cell performance.[22,23,27,38] Note that this simulation, performed without any polarization and neglecting the oxygen partial pressure, yields the same results as experiments under various experimental conditions. Hence, cation segregation seems to lead to a broad thermodynamic minimum, whose reach can only be suppressed sufficiently if the mechanism leading there is understood. The highly localized deposition on the complexion/vacuum interface, in combination with the observed high cation mobilities in this area, hints towards a segregation mechanism via the complexion.

Thus, we propose a complexion-mediated cation segregation pathway, which is illustrated for Sr in Figure 2d. Instead of migrating via the LSM bulk to the surface, where cation diffusion is severely limited,[24] cations close to the grain boundary diffuse into the complexion, which features a significantly enhanced ion mobility. The enhanced diffusion in the complexion leads to a faster thermodynamic equilibration, which, according to our simulations, includes Sr and Mn oxide formation on the complexion surface.

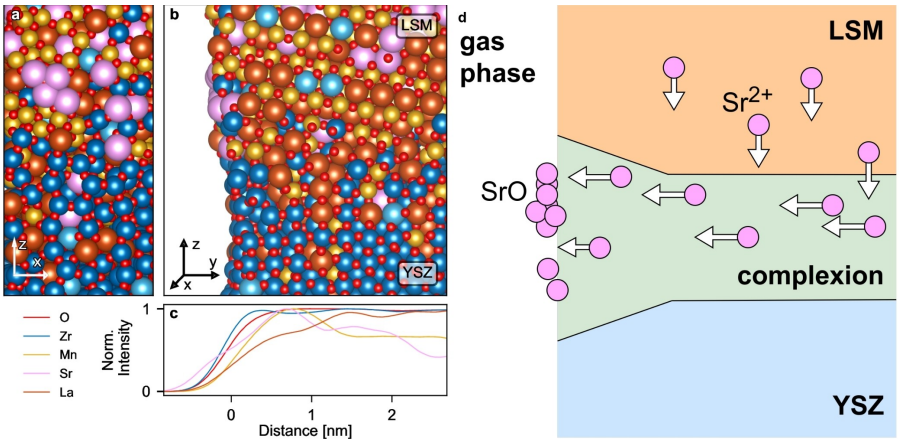

Figure 2. (a) Top view of one simulated cell showing the complexion/vacuum interface. (b) Cut through the surface shown in (a) to show complexion evolution to the surface. (c) The normalized intensity of the elemental profiles from the vacuum along the complexion obtained by overlaying the atoms ±7 Å from complexion center with 3D Gaussian functions and projection onto the y dimension. (d) Proposed cation segregation pathway to the complexion surface, illustratively shown for Sr.

In addition to the often contemplated effect of reduced electronic conductivity in LSM due to Sr bleeding, this surface oxide formation might actually result in physical blockage of active sites.[38] It may thus render Sr segregation into a potentially active zone, i.e. the surface of the complexion, a plausible source for degradation. The driving force behind this mechanism might be electrostatic and elastic interactions of the cations in the complexion, which are believed to cause Sr segregation in pure LSM,[38] and agree with our findings that Sr is almost absent within the complexion.[39] However, further studies are required to fully elucidate the mechanistic details of this pathway.

Experiments

Cation mobility

In order to validate the simulation results we analyzed the aged sample (150 h, heated up to 1173 K) by STEM-EDX. We first investigate the cation diffusion along the grain boundaries. Figure 3 shows part of the LSM/YSZ mixed electrode close to the interface of the YSZ electrolyte (for details on the cell structure see Ref. [39]). The phase separation between the LSM and YSZ phase is depicted in Figure 3a by elemental maps. Together with a bright field (BF) TEM image (left), the elemental distribution is revealed by a combined Zr/La EDX map (blue/red) and single EDX maps of Mn (yellow), La (red) and Sr (pink). As predicted by the simulations discussed above, Mn and La exhibit increased mobility trough the complexion into YSZ and its grain boundary, which is highlighted in Figure 3b. At the grain boundaries between different YSZ grains, the Mn and La signals could be detected as shown by an enhanced signal, indicating cation diffusion along these grain boundaries (see also yellow and red arrow, respectively). For Sr, in contrast, we could not detect any signal, above the noise level, outside the LSM grains. Note, that the seemingly low Sr content in Figure 3b can not be attributed to a significant spectral Sr feature applying standard analysis routines. These findings on the diffusion or lack thereof of La, Mn, and Sr cations along the grain boundaries are further corroborated by Figure S3 in the Supporting Information. However, as found by simulations, mobility for Sr is also to be expected. Therefore, two questions arise: whether this negative finding is merely due to limitations in the data analysis and whether, it is possible to detect the predicted Sr diffusion and enhancement at the complexion/vacuum interface. Note, that the Sr content is nominally only 4 at% in the LSM phase and potentially much less outside the LSM grain.

Drift correction

To answer the question which emerges from the simulation experimentally is a rather complex challenge, as size of the simulated strontium oxide nucleation seed is rather on the Ångström than nanometer scale. Investigating such small variations of elemental concentration changes requires an analysis close to the microscopic resolution and detection limit and is, therefore, extremely challenging. On top, appropriate sample preparation to uncover potential complexion/vacuum interfaces for TEM investigations introduces an additional degree of complexity.

The small width of the complexion paired with the even smaller size of its interface with the gas phase evoke the need to assess minor changes in the concentration of individual elements with very high spatial resolution. Only this would enable us to prospectively track the whole surface oxide formation process from the beginning. This would also allow the investigation of its formation mechanism in full detail, which is necessary for its direct linkage to cell performance.

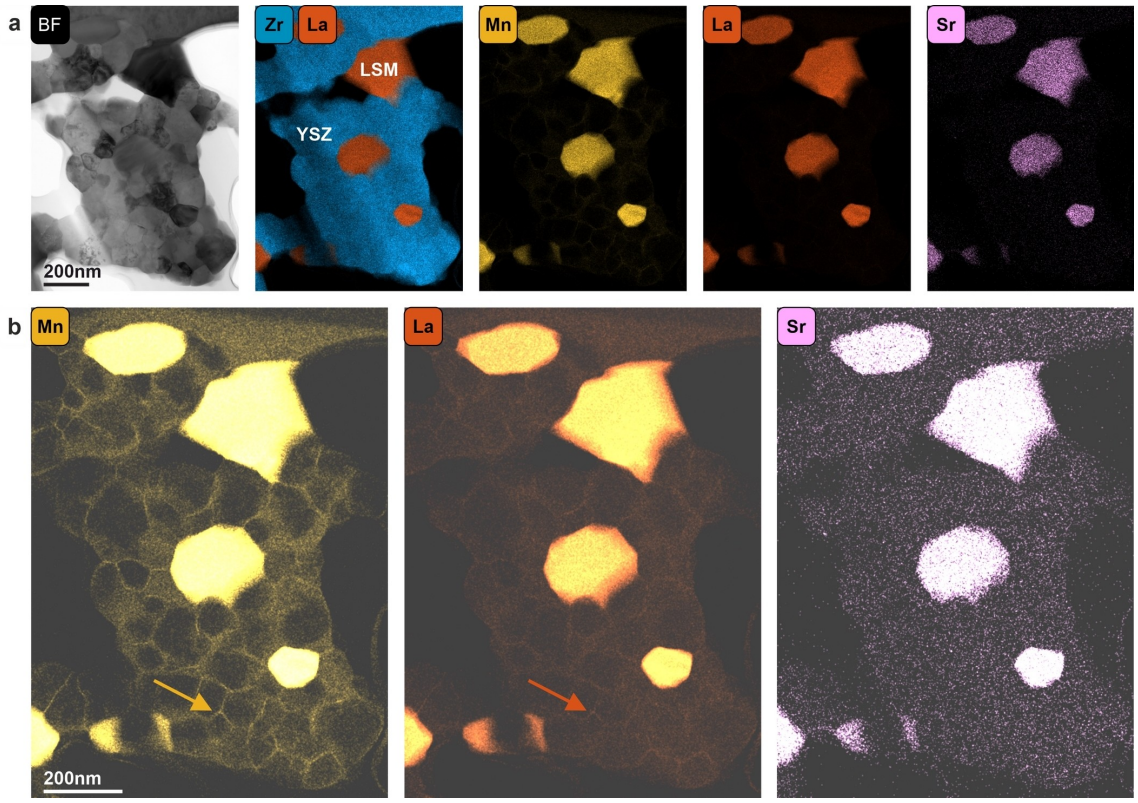

Figure 3. Cation mobility. (a) Bright field image (BF) of a mixed LSM/YSZ electrode and EDX elemental maps of zirconium and lanthanum (Zr/La), manganese (Mn), lanthanum (La) and strontium (Sr) of the corresponding region shown in BF. (b) Contrast- and brightness-adjusted maps of Mn, La and Sr highlight enhanced signal at the grain boundaries between different YSZ grains for Mn (yellow arrow) and less pronounced for La (red arrow). Sr is only resolved within the LSM grains, the low and homogeneous signal over the YSZ grains is attributed to residual background and noise contribution due the low Sr content.

To overcome the aforementioned issues, we developed a routine that is based on post-acquisition drift correction, component analysis and statistical analysis. The developed routine is demonstrated in the following. For details on the sample preparation and the optimized acquisition procedure for optimized signal detection to avoid e-beam induced artifacts which would limit any unambiguous interpretation, we refer to the Methods section.

In Figure 4a, BF images from different points in time during the acquisition of an EDX spectrum image close to the complexion/vacuum interface are displayed. Compared to the first frame, the additional images of this series exhibit significant drifts of several nanometers despite using the online drift correction of the acquisition software. Since this residual drift is much larger than the localization of the desired information, i.e. the strontium oxide accumulation, the spectrum images can hardly be used without further processing as the spectral information is blurred in an analog way. The top-left panel in Figure 4b shows the resulting image when summing up all BF images from all 175 frames in the EDX hyperspectral cube. Compared to the single snapshots, it appears very smoothed while well defined contrast changes are absent. This is further illustrated in Figure S6, where the effect is simulated on a 2D Gaussian with a full-width at half maximum of 1 nm and is shown to lead to strong delocalization and distortion.

Figure 4b also shows the results of different drift detection algorithms. Cross-correlation (top right), a standard technique used for such tasks, results in a minute improvement especially in the horizontal direction. However, it does not lead to significant improvements, even though there are sharp and significant contrast changes in the image. Thus, we employed a different approach in which 100 templates (a combination of manually and randomly placed ones, refer to Figure S4) are matched every frame, for each of the three image types that are acquired, i.e. BF, dark field (DF) and high-angle annular dark field (HAADF), resulting in 300 template matches each frame. This creates a much sharper image, which can be further improved if the image shift is not determined from all template matching results, but if an outlier check is first performed using the RANSAC algorithm.[78] This creates a summed image that is comparable to the single frames. Figure S7 highlights the effect of the RANSAC outlier removal: from the multitude of template match results (in gray), only the orange points are considered inliers. The drift detected by applying a Euclidean transform model to the RANSAC inliers follows the orange points closely (see the blue curve), whereas the one from all templates (green) deviates strongly, especially at high time values in x (horizontal direction) and already before that in y (vertical direction).

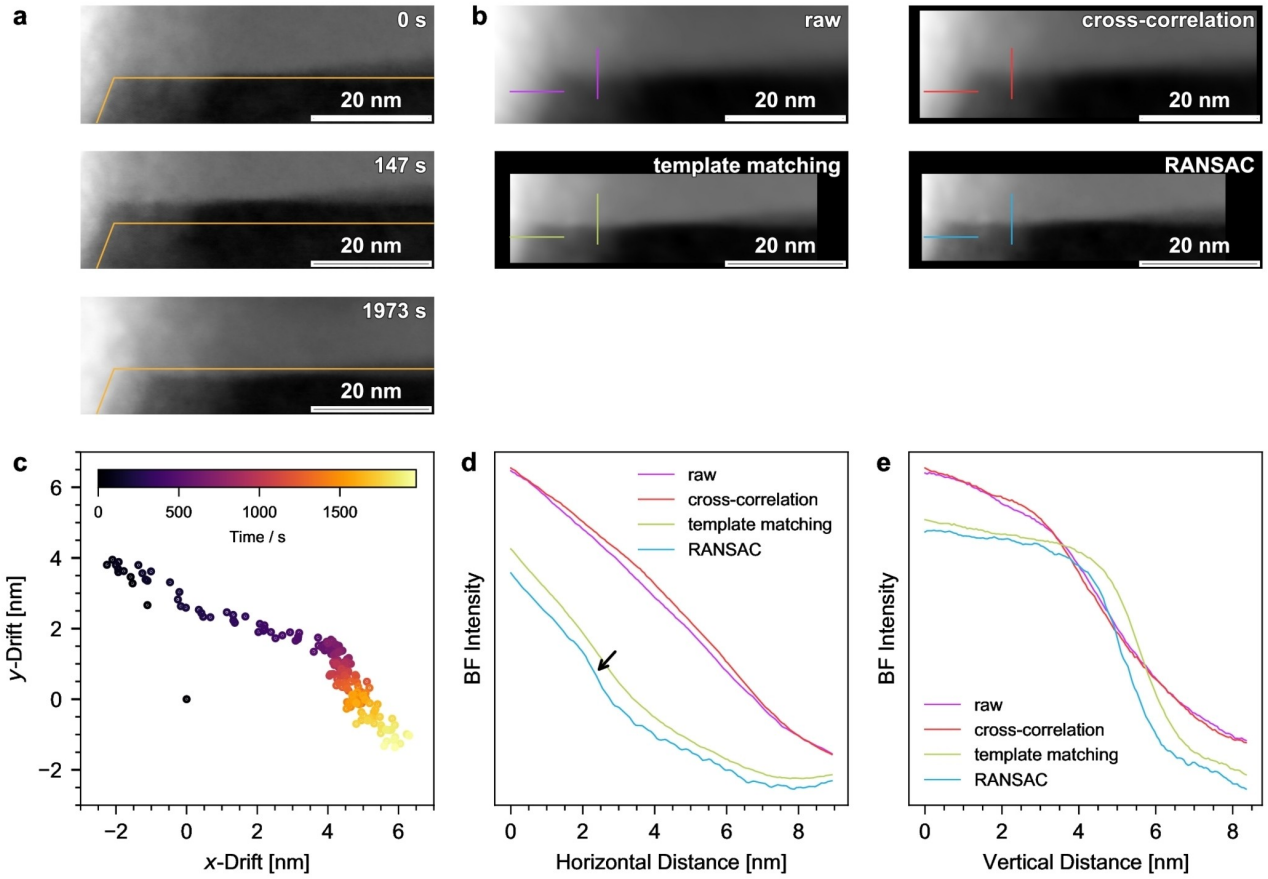

Figure 4. Post-acquisition drift correction. (a) Selected BF snapshots from different times during the spectrum image acquisition still show considerable drift with respect to the first frame at 0 s. The orange lines serve as guides to the eye to enhance the visibility of the drift still present in the raw data. (b) Comparison of the summed BF images without further correction ('raw') and after different post-acquisition drift correction algorithms. Image regions not present in every frame are masked, effectively cropping the available field of view. (c) The residual sample motion after acquisition, as measured using the RANSAC algorithm. In (d) and (e), intensity profiles along the lines indicated in b) are plotted. Neither the online drift detection ('raw'), nor cross-correlation yield adequate results and lead to very blurred contrast changes. RANSAC generates the sharpest steps and is the only technique to resolve the small step just above 2 nm in d) (see the arrow).

The temporal drift evolution from RANSAC in Figure 4c reveals that there is a fast sample motion in the beginning toward the top-left, which is in line with the images in Figure 4a, and then the sample drifts towards the lower right rather linearly, with a slight kink in the position distribution between 500 s and 1000 s. The sample drift thus spans a distance of around 8 nm in *x* and 5 nm in *y* direction, which is insufficient for detecting local information at the nanometer scale, let alone in the range of a few Ångström.

Figure S8 also shows the time-dependent drifts obtained from all methods. While RANSAC and template matching have similar trends, cross-correlation appears to be insufficient for the present images, explaining the blurred image. It should be noted that the corrected images are cropped because only pixels that are contained in every shift-corrected frame can contribute to the final image. Thus, the field-of-view is restricted. However, this is compensated by a gain in spatial resolution. This improvement can also be seen in Figure 4d and Figure 4e. In these figures, line profiles of the BF image in horizontal and vertical direction are plotted for the different drift correction types. As discussed before, cross-correlation only leads to a negligible improvement over the raw data as output from the microscope software. However, the vertical step is significantly sharper for both template-matching-based procedures, with RANSAC leading to the sharpest contrast change. Furthermore, in the horizontal profile, RANSAC is the only drift correction method that resolves the small step at around 2 nm, as indicated by the arrow in Figure 4d.

Component Analysis

The EDX data was analyzed and decomposed into individual elemental maps using two alternative, but complementary routes: (a) by standard evaluation tools and (b) by a standalone Non-Negative Matrix Factorization (NMF), which would enable automated analysis and add superior spatial resolution due to the possibility to apply additional drift correction and denois-

ing, i.e. less binning. Automated analysis is important in order to achieve a high throughput analysis, which would allow for a statistical evaluation of the sample at high spatial resolution and the tracking of nanostructural inhomogeneities at the complexion/vacuum interface. Spatial resolution is required as in the case of SOCs the Sr enrichment is an atomic scale phenomenon located at a small fraction of the sample. Results from the standard procedure are shown in Figure S9 and used as a reference for the NMF analysis. The results of the NMF analysis are shown in Figure 5. Additionally, the drift-corrected HAADF- and BF-STEM images are presented for comparison in the same figure. Complete results of the NMF are given in the SI Figures S10 and S11, as well as an analysis of the Sr signal in YSZ due to the overlap of Sr, Y and Zr spectral peaks in Figure S12.

While both methods are able to separate the EDX signal into the elemental maps, the drift corrected NMF yields sharper edges and higher contrast of intensities in comparison to the standard procedure. This allows for an improved quantitative analysis of the respective element distributions in the sample, even for the doping elements Sr and Y, which have comparably low concentration (approximately 3.8 at% in LSM and 5.1 at% in YSZ).

Comparing the elemental maps from both methods (Figure 5 and Figure S9), a prominent feature is the concentration edge in the oxygen map at the transition of YSZ to LSM obtained by both techniques. When taking a closer look at the oxygen density in the individual bulk materials, LSM is expected to have 86.8% of the oxygen number density of YSZ as calculated from experimental lattice parameters.[39] While the standard evaluation procedure yields a ratio of approximately 81%, the drift-corrected NMF data is able to capture this difference as well, yielding a ratio of 91% of the mean oxygen concentrations between LSM and YSZ (see Figure S13 in the SI for details). As opposed to the maps of the drift-corrected NMF analysis the elemental maps of the standard evaluation procedure appear more blurred at the interfaces. Overall this analysis shows that automated routines, such as drift corrected NMFs, can be used to efficiently analyze large EDX data stacks and perform high-throughput analysis in to order to understand local compositional variations of SOCs.

Statistical analysis

In order to resolve minute concentration differences of dopant species, such as Sr, with high spatial resolution, we perform Welch tests, i.e. statistical tests which are able to distinguish unequal mean values of sample distributions.[79] To demonstrate their performance, the tests were first applied to the bulk signal of the Sr elemental map. Figure 6a shows the complete relative spectral contribution of the Sr intensity map obtained by the drift-corrected NMF. The dashed black line marks the area in which the sample was found to possess a constant thickness. To the left, the sample features a wedge-like shape, becoming progressively thinner (compare SI Figure S14). Colored rectangles mark the positions of sections shown in the other subplots. For the first set of tests, the Sr map was divided into 25 equally sized areas, shown as blue rectangles in Figure 6b. The Sr concentration in each of those areas was compared to the same central Sr bulk area, marked by a dashed red boundary. Note that, as a consequence, the red-marked area is also compared to itself. A close-up of this reference area is shown in Figure 6c.

We performed two-sided Welch t-tests, meaning that the alternative hypothesis constitutes an either smaller or higher mean concentration in the respective areas of comparison. In order to conduct a Welch test comparing two areas, these areas are each sub-divided into 30 smaller regions. Each of the smaller sub-regions is 19.5 Å^2 in size, making the total compared areas 5.85 nm^2. The values within each sub-region are aggregated. From the resulting 30 cumulative intensity values, 15 were selected randomly (with replacement) and used in the test. One realization of the selected sub-regions within the compared areas resulting from this stochastic sampling process is exemplarily shown in Figure 6d for one of the blue areas and the reference area. The binning of the smaller sub-

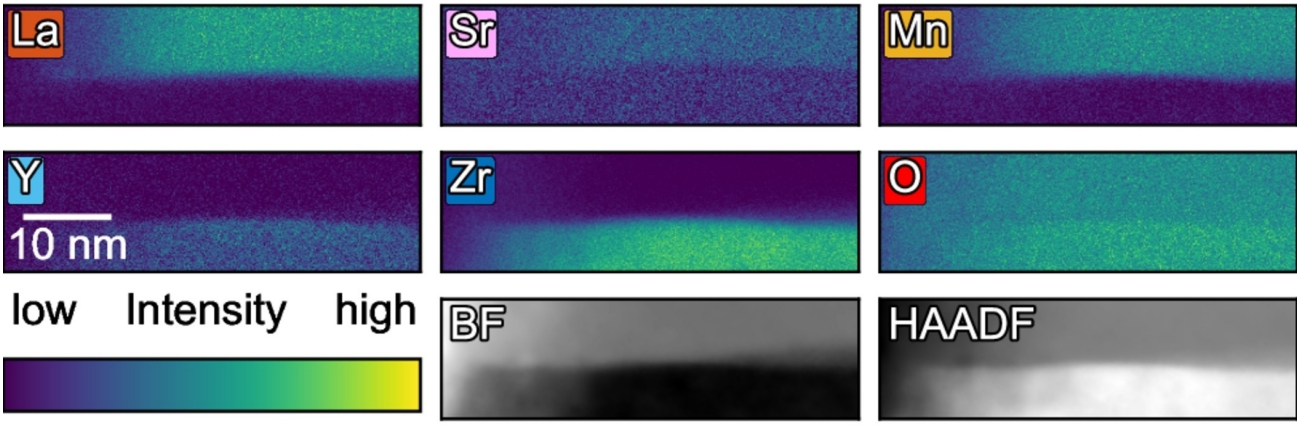

Figure 5. NMF decomposition of the EDX raw data after application of the drift correction. All elemental maps are binned (3×2 pixel bins). The binning was applied after the drift-correction and before conducting the NMF.

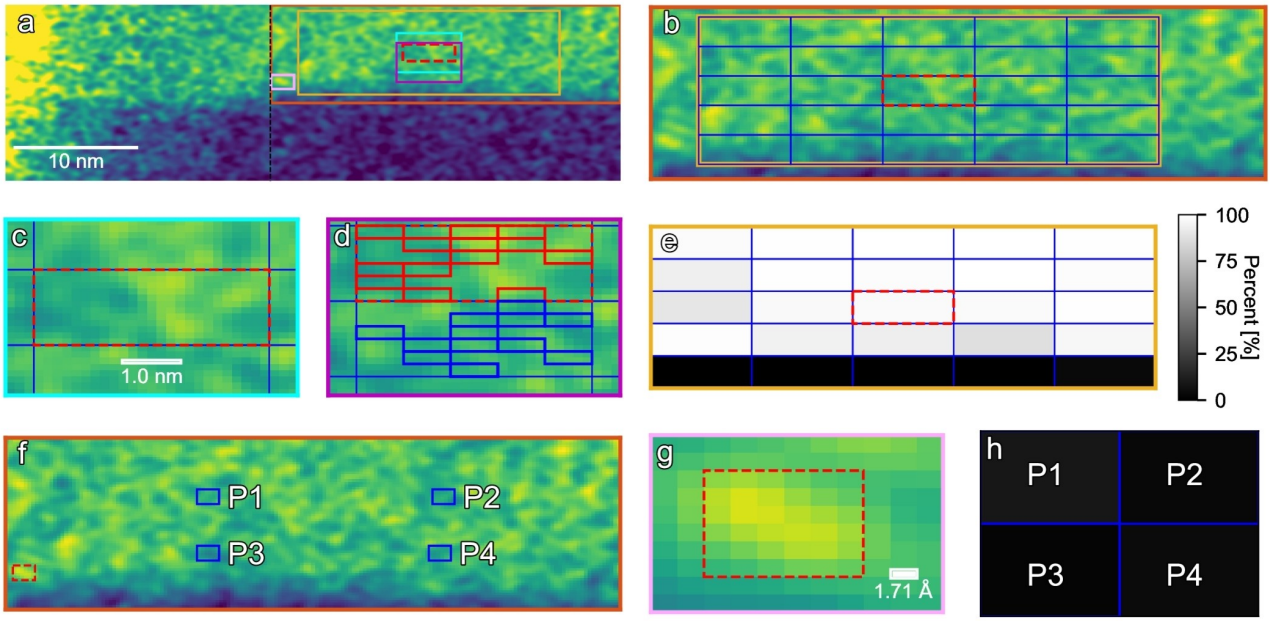

Figure 6. (a) Relative spectral contribution of the Sr EDX map obtained from the NMF broadened by a Gaussian filter to ease viewing. The colored rectangles show the positions of the following subplots: orange: b + f, cyan: c, magenta: d, pink: g. The dashed red rectangle is the reference area for the bulk Welch tests and the dashed line indicates the area where the sample has an even thickness (compare SI Figure S14). (b) Close up of the sample area with high Sr content. Random samples from the red dashed rectangle (close-up shown in (c)) are compared to random samples drawn from each individual blue rectangle in Welch tests. (d) One exemplary realization of random samples (smaller rectangles) drawn from each area (larger, confining rectangle) that are compared in a single Welch test. (e) Percentage of passed tests (see Table S2 in SI for exact numbers). (f) Location of passed one-sided Welch tests to test of higher Sr concentration (red dashed rectangle) close to the HAADF-determined surface with bulk position (blue rectangles). (g) Close-up of the area with higher Sr content. (h) Percentage of passed Welch tests, stating that the red area has a higher mean concentration than the blue areas specified in (f). The colormap is the same as used in (e).

regions improves the power of the test by yielding more normally distributed samples. True random sampling from the compared areas is important to enable a meaningful statistical evaluation.

A failure of the test indicates a high probability that the alternative hypothesis is true, with the significance of the test being reflected in the reproducibility of the results. We have here selected the settings such that the alternative hypothesis can be accepted with statistical relevance defined by a significance (P-value) lower than 0.05. A passed Welch test, on the other hand, can have two possible reasons: either the null hypothesis is really true or the chosen test settings are not able to resolve the desired property from the provided samples. It is thus only a weak indicator that the null hypothesis is true and other test settings and/or data are necessary to prove the hypothesis. Note that a hypothesis can never be proven directly, but indirect proof is possible by falsifying a suitable null hypothesis.

Even for a successful test, not all individual random Welch tests are necessarily delivering the same error-free results. As mentioned above, the reliability of the test is related to the significance, which indicates the smallest value level of α at which the null hypothesis can be rejected according to the provided samples. To further demonstrate the statistical robustness of the chosen test settings, 1000 Welch tests were performed for each comparison. The relative share of passed tests for the Sr bulk investigation is displayed in Figure 6e (see Table S2 in the SI for exact values). Within the bulk area itself (upper 20 regions), the majority of tests are passed (white color), indicating that the average mean between the areas is similar, or at least differences cannot be resolved with the chosen test settings. However, some of these regions on the left and lower edge show a higher failure rate, suggesting that there might be local changes in the areas themselves, which cannot be resolved with the chosen area size. The five lower areas fail the majority of the tests with significant accuracy (black color, compare Table S2), revealing a diverging mean Sr concentration in these areas compared to the central bulk reference region. Comparing the signal intensity in these areas with the reference, it becomes clear that these areas must contain less Sr, which is most probably due to the incipient complexion, for which we have shown before that it features much lower Sr concentrations than bulk LSM.[39]

This first analysis shows that nanoscale trends can be confirmed with Welch tests with significant certainty. However, small features like the oxide nucleation seeds found in the simulation require an even higher resolution. We thus compare one small region close to the complexion with potentially higher concentration to several bulk positions, in order to demonstrate the power of the conducted Welch test. Figure 6f gives an overview of the compared areas, with a close up of the reference area enclosed in red given in Figure 6f. With the new

hypothesis that the reference area has a higher concentration than the bulk areas, we can perform one-sided Welch test, which need less samples and do thus allow for a higher resolution. Note that, other than for the bulk Welch tests, here the random samples from compared areas are not re-binned, but the individual pixel values are taken. The area of such a random sample is thus only 1.95 Å^2. With an area containing only $6\times6=36$ of these, the resolution demonstrated here is 70.2 Å^2, which would correspond to a cluster containing only a few atoms in the xy dimensions.

As before, 1000 tests were performed. The percentage of passed tests is given in Figure 6h (see Table S3 in SI for numbers). The results of the tests suggest that the alternative hypothesis is accepted for all areas, stating that the mean concentration in the red area is significantly higher than in each of the ones marked in blue. These results demonstrate that the informative value of high resolution EDX measurements can be pushed to resolve concentrational deviations in areas down lower than the nanoscale. The selected combination of data post-processing methods demonstrated the resolution of minor changes in elemental distributions, and thus provides an indispensable tool for the detection of nucleation seeds. This now enables more detailed investigations of the complexion evolution over time and the linkage of concentration changes on its surface to cell deactivation.

The presented results render Sr segregation in SOCs a very probable reason for cell deactivation, in line with earlier findings at larger length scales. However, whether the segregated cations mainly lead to spatial blockage of the active site or to its loss via exsolution of the complexion, accompanied by the creation of voids and increasing porosity, needs yet to be determined at atomistic resolution. The proposed workflow provides a tool for an automated, robust, and fast analysis of EDX spectrum images necessary for such a detailed analysis of a large data stack, especially when the focus is on low-concentration elements such as strontium in the LSM perovskite studied here. This way, the cation agglomeration and nucleus growth can be tracked from early stages where only minute stoichiometric changes are anticipated. The flexible design of our routine based on multi-variate statistical analysis allows for easy and straightforward adaptation for the investigation of other materials. This is of high interest, especially for other electrode materials such as $La_xSr_{1-x}Co_yFe_{1-y}O_{3-\delta}$ (LSCF), for which high temperature environmental scanning electron microscopy spectra of the grain boundaries also hint at a Sr segregation pathway via a complexion.[80] However, further studies are needed to verify this conjecture and to establish the relevance of the proposed mechanism for other materials.

Surface Spectroscopy

In order to assess the potential enrichment of strontium at the surface, we have additionally conducted XPS measurements, as seen in Figure 7. In Figure 7a, the Sr 3d regions are plotted for two samples: one that has only been sintered at 1423 K for 1 h (pristine, blue), and one ('aged', orange) that has additionally

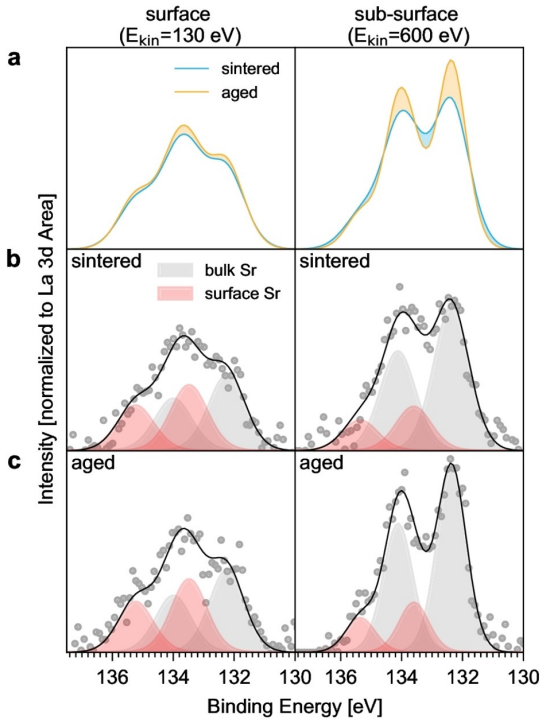

Figure 7. Sr 3d photoelectron spectra. (a) the surface (left) and sub-surface (right) spectra for the sintered and aged cells, normalized to the corresponding La 3d areas. During aging, the Sr/La ratio changes at the surface, see also Table 1. The blue and orange shaded regions illustrate regions where the sintered (blue) and aged (orange) spectra have higher intensities, respectively. In (b) and (c), peak fits of the Sr 3d region show that an additional component, shifted to higher binding energies compared to the bulk perovskite strontium, is present and seems to be accumulated at the surface, hence labeled as 'surface Sr'.

been aged thermally at temperatures up to 1173 K for 150 without polarization. The left panel contains the surface-sensitive spectra that have been acquired with a kinetic energy of 130 eV, and the sub-surface-sensitive data is in the right panel (600 eV). According to the TPP-2M equation,[81] the escape depths for these kinetic energies can be estimated to be $3\lambda=$ 1.6 nm for the surface, and $3\lambda=4$ nm for sub-surface spectra (with λ being the inelastic mean free path). All spectra are normalized to the respective total La 3d area in order to investigate the distribution of A-site elements in the perovskite (when considering the form ABO_3). In the aged sample, there is a slight accumulation of strontium at the surface. More specifically, an increase of the Sr/La ratio of 11.5 %, see also Table 1. This corresponds to an increase of 9.7 % in the nominal A site occupancy by Sr, which might also result from segregation of strontium oxide. In addition, the sub-surface seems to be enriched in Sr in the aged sample, which could be explained by a diffusional concentration gradient originating from the LSM bulk.

The peak shapes of the Sr 3d surface and sub-surface spectra appear to be significantly different. Thus, peak fitting was performed, as shown in Figure 7b and Figure 7c. This procedure reveals that, in addition to the expected Sr 3d

Table 1. The Sr/La ratio and fraction of Sr in the A site of the perovskite both increase upon thermal aging by 11.5% and 9.7%, respectively, while the fraction of surface Sr species ($Sr_{surf.}$) does not change significantly during the aging process.

condition	E_{kin} [eV]	Sr/La ratio	Sr in A site [at%]	$Sr_{surf.}$ [%]
sintered	130	0.169	14.5	46.5
sintered	600	0.212	17.5	23.4
aged	130	0.189	15.9	47.1
aged	600	0.224	18.3	21.1

doublet ($3d_{5/2}$ at a binding energy of 132.2 eV, colored gray in the plots), a second component is present in all spectra (red). This component is shifted to higher binding energies, with the $3d_{5/2}$ maximum at 133.6 eV and is more prominent in the surface spectra, where it makes up around 47% of the Sr 3d region for both samples, compared to just above 20% in the sub-surface. The main component thus seems to be the bulk oxide, which is in good agreement to literature values for perovskites,[82] and strontium oxide.[83]

The high-binding-energy component has been observed for other perovskites as well,[69] mostly being ascribed to carbonates.[83] Due to the generally very low amount of Sr in the sample (roughly 4 at% in LSM, accordingly less in the approximately 1:1 LSM/YSZ mixture), no distinct carbonate signal can be resolved in the C 1s spectra. Since it is thus not possible to clearly ascribe the component to a certain compound. We, thus, refer to it as'surface Sr', following the nomenclature recently used for lanthanum strontium ferrite.[69] In contrast to this system, the fraction of surface Sr species in LSM is, however, not increased after aging. Instead, the total amount of Sr is increased. As seen from Table 1, the fraction of bulk oxide species remains constant during aging. Thus, the observed Sr accumulation on the surface does not stem from the formation of secondary species, e.g. carbonate species, but from a general increase in Sr content towards the surface.

While it is impossible to draw the conclusion of where exactly the Sr agglomerations are located, i.e. at the complexion/vacuum interface or the LSM/vacuum interface, because XPS is a laterally integrative technique, the results seem to be in line with the simulation data in Figure 2. In order to further affirm this link, future experiments need to be performed on model systems with ultra-thin perovskite layers. That way, by means of synchrotron-based XPS depth profiling, the complexion can be probed directly and distinguished from the LSM/vacuum surface.

Conclusion

Combining MC and MD simulation, spatially resolved EDX-STEM mapping, and post-acquisition drift analysis, we could validate a predicted atomic scale Sr enrichment at the complexion/vacuum interface occurring on the LSM/YSZ side of SOECs after thermal aging up to 1073 K for 150 h. The results are complemented by surface-sensitive XPS measurements. In addition, simulations demonstrated increased diffusion rates in the complexion for both oxygen anions and cations, which has been corroborated by experimental observations. The formation of highly localized and atomically dispersed Sr enrichment at the complexion/vacuum interface which was found in the MC simulations could be validated by a newly developed, robust routine, which is based on STEM-EDX analysis, drift correction, NMF and Welch t-test. This automated data analysis is superior in spatial resolution and analysis times compared to standard evaluation procedures, while qualitatively similar results are obtained. This renders the outlined drift-corrected NMF analysis of large EDX stacks capable for high-throughput analysis to study the origins of compositional variations in SOECs down to the atomic scale. This will ultimately lead to improved structure-function correlations and a deepened understanding of deactivation processes.

Experimental and Methods Section

Theoretical methods

Monte Carlo Simulation

Two kinds of simulation cells were built and the preparational sintering process was simulated for 16 different doping realizations, each with the force-field based MC algorithm that has been described in previous work.[39] The cells that were obtained in this earlier work have been used to obtain ion diffusion coefficients across the interface using spatially restricted lag time mean square displacements.[48] For the surface simulations, a bigger cell containing a total of 21,330 atoms with lattice vectors measuring 22.4× 93.6×147.9 Å has been constructed in such a way, that a big hole cutting through the complexion between the two materials exposes two surfaces at the YSZ/LSM interface in the xz-plane (see SI Figure S1).

All cells have been aligned in the direction orthogonal to the complexion to match in the point of inflection of the fitted Mn elemental profiles across the complexion. Elemental profiles of MC-'sintered' cells with the described surface models were obtained from the projection of atom positions (up to ±7 Å from the complexion center in z direction) overlaid with Gaussian functions to the y dimension. In order to include both surfaces featured in the cell, the elemental profiles were folded around the z direction at the middle of the simulation cell, which is 3 nm from either surface.

Molecular Dynamics

Molecular Dynamic simulations have been conducted for 1 ns after an equilibration time of 10 ps with a time step of 1 fs for 6 different structures employing LAMMPS.[84] The force field is the same as in the MC simulations. Spatial resolution of the diffusion is achieved by calculating the lag time mean square displacement for all atoms that have not left the region ±5 Å around the specified point during the respective time periods.[48]

Sample preparation

The half cells, LSM||LSM+8YSZ||8YSZ, were prepared using yttria-stabilized zirconia (8YSZ, with 8 mol% Y_2O_3) electrolyte supports (Kerafol®, nominal diameter 20 mm and thickness

300 μm). Terpineol-based slurries were prepared with pure LSM ($(La_{0.8}Sr_{0.2})_{0.95}MnO_{3-\delta}$) powder (Fuel Cell Materials) and an LSM + YSZ (50/50) composite. First, an LSM + YSZ layer (thickness approximately 25 μm and diameter 8 mm) was symmetrically screen printed on both sides of the dense 8YSZ supports and after drying it at 353 K, an LSM layer (thickness about 25 μm, diameter 8 mm) was printed on both sides. The final sintering was performed at 1423 K for 1 h in air, with a heating rate of 2 $Kmin^{-1}$. One of the cells (labeled 'aged' throughout this manuscript) was further treated thermally for 150 h at temperatures of 1173 K in order to investigate the effects of thermal aging by means of EDX.

Specimens for electron microscopy were prepared by cutting the cells with a wire saw and subsequent polishing at an angle of 30 . From this oblique cross-section, a TEM lamella was prepared using an FEI Helios NanoLab G3 FIB-SEM Dualbeam system. Special care has been taken to avoid and remove re-deposited material at the interface of interest during the final low energy cleaning step.

For X-ray photoelectron spectroscopy (XPS) measurements, both cells (sintered and aged) were polished in plan-view, removing the LSM current collector layer (corresponding to the topmost 30 μm). Refer to Figure S2 for an optical microscopy image detailing one of these samples.

Electron microscopy and spectroscopy

STEM-EDX

TEM analysis – consisting of simultaneous image and EDX spectrum acquisition – was done in a ThermoFisher Scientific Talos F200X at 200 kV. The microscope was equipped with four silicon drift detectors (SDDs) in Super-X configuration, spanning a solid angle of 0.9 sr. A semi-convergence angle of 10.5 mrad was used with a beam current ranging between 50 to 450 pA. To improve the signal to noise ratio, multiple frames were acquired with the same parameters and summed up, applying an online drift correction based on cross correlation between each frame (Velox software, Thermo Fisher Scientific). Either raw data were used for further analysis, or background subtraction (empirical background model) was applied as well as prefiltering. For pre-filtering, the data were averaged over 4 (Figure 3) or 2 (Figure S3) next neighbor pixels, before EDX maps were extracted from the spectrum image data set. 4 pixels (Figure 3) relate to 3.5 nm and 2 pixels (Figure S3) relate to 328 pm. Pre-filtering reduces the spatial resolution. Note, the point resolution of the microscope is 160 pm. This is not the case for the data shown in Figure 5 (58 pm pixel size), in which the raw data (4D data stack, consisting of 175 frames, each including 3D spectrum image) is further analyzed.

Drift correction

While modern microscope acquisition software is equipped with real-time drift correction systems, there are cases where its performance is not sufficient, especially at high magnifications. Thus, we have developed an off-line, post-acquisition drift correction routine based on multiple template matching using scikit-image,[85] and subsequent outlier removal using random sample consensus (RANSAC).[78] In total, *N* templates (typically 100) are selected, with a few of them being placed manually and the rest of them randomly chosen. As shown in Figure S4, a region can be defined inside which all randomly assigned templates need to be located. Then, these templates are extracted from all image types acquired along with the SI spectrum image to make the procedure more robust to small changes in contrast (bright field images are especially prone to this). In our case, bright field (BF), dark field (DF) and high-angle annular dark field (HAADF) are obtained, thus increasing the number of available templates for the template matching by a factor of 3. These templates are matched for every frame in the spectrum image time series, after a Gaussian filter with $\sigma = 2$ px (corresponding to 0.639 nm) has been applied to both the templates and the images in order to avoid potential issues arising from the loss of atomic resolution due to focal changes. Instead of fitting a Euclidean transformation model to all 3*N* data, the robustness of the shift detection is improved by applying a RANSAC algorithm to the template match results, removing all outliers. By outsourcing the parameters to an external configuration file (in the YAML format), rapid screening of the optimal settings is possible in parallel. Afterwards, the drift correction is applied to the spectrum image stack.

Non-Negative Matrix Factorization

Each individual spatially resolved spectrum is convolved with a moving average with a window width of 100 eV. In order to increase the signal while still getting sufficient spatial resolution, spatial binning of the spectra with a bin size of 3 in x and 2 in y direction was performed. A Non-Negative Matrix Factorization (NMF) (employing the scikit-learn routine[86]) of the measured spectrum is used to identify the elemental composition at each measured spatial point. The initial component guess was based on experimental spectra originating from YSZ and LSM regions, far off the interface. Therefore, single element components (Y, Zr, La, Sr, Mn) were extracted from the experimental LSM and YSZ spectra using a home-made fitting routine, which combines serial and simultaneously Gauss peak fitting (Figure S5). These fitted components, together with a vector featuring the fitted background (Velox) and constructed spectra of other identified elements served as initial component guess.

Statistical Analysis

The mean concentrations at different areas with high resolution were investigated with Welch t-tests[79] performed on the elemental intensities obtained from the NMF. For two-sided Welch tests comparing solely the bulk regions, the 5.85 nm^2 areas were divided into 30 19.5 $Å^2$ sized samples, each containing 2×5 pixels of the maps obtained from NMF. The pixels in each sample are then aggregated into one value. 15 samples were drawn randomly with replacement from each investigated area. For the high resolution one-sided Welch tests, the investigated 70.2 $Å^2$ areas were divided into 36 of the 1.95 $Å^2$ NMF pixels and used directly in the test. 24 random samples were drawn from each area for each test. All tests were performed with a confidence interval of $\alpha = 0.95$ and without assumption of equal variances. Illustrations and further details on the execution of the tests are given in the respective results section.

X-ray photoelectron spectroscopy (XPS)

X-ray photoelectron spectra were acquired at the ISISS-PGM beam line at BESSY II for planpolished samples (see above). The setup consists of a Specs Phoibos 150 near-ambient pressure hemispherical sector analyzer and the measurements were performed in high vacuum at kinetic energies of 130 eV and 600 eV in order to achieve surface- and sub-surface-sensitivity. Spectral analysis was done in CasaXPS. Charge-induced drift was corrected for by using the C 1s region (adventitious carbon) and the valence band maximum. Shirley-type backgrounds were employed and for all fitted components, Pseudo-Voigt shapes with 30% Lorentzian character were used. For quantification, the peak areas were

corrected for the beamline flux (separately measured using a gold foil) and the respective cross sections.[87]

Acknowledgements

This work was supported by the Deutsche Forschungsgemeinschaft (DFG, German Research Foundation) under the priority programme SPP 2080 DynaKat. T. Götsch, F.-P. Schmidt, and T. Lunkenbein acknowledge support from the Federal Ministry of Education and Research in the framework of the project Catlab (03EW0015A). Moreover, this work was partially funded by the Deutsche Forschungsgemeinschaft (DFG, German Research Foundation) under Germany's Excellence Strategy – EXC 2089/1 – 390776260. The authors acknowledge the Helmholtz Zentrum Berlin für Materialien und Energie for allocating beam time within proposal number 221-10744CR. Additionally, the authors thank V. Vibhu for preparation of the electrodes. Open Access funding enabled and organized by Projekt DEAL.

Conflict of Interest

The authors declare no conflict of interest.

Data Availability Statement

The data that support the findings of this study are available from the corresponding author upon reasonable request.

Keywords: complexion · electron microscopy · interfaces · molecular modeling · segregation

[1] R. M. Ormerod, *Chem. Soc. Rev.* **2003**, *32*, 17–28.
[2] E. D. Wachsman, K. T. Lee, *Science* **2011**, *334*, 935–939.
[3] A. S. Brouwer, M. van den Broek, A. Seebregts, A. Faaij, *Renewable Sustainable Energy Rev.* **2014**, *33*, 443–466.
[4] S. R. Foit, I. C. Vinke, L. G. J. de Haart, R.-A. Eichel, *Angew. Chem. Int. Ed.* **2017**, *56*, 5402–5411; *Angew. Chem.* **2017**, *129*, 5488–5498.
[5] M. S. Sohal, J. E. O'Brien, C. M. Stoots, V. I. Sharma, B. Yildiz, A. Virkar, *J. Fuel Cell Sci. Tech.* **2012**, *9*, 011017.
[6] A. Atkinson, S. Barnett, R. J. Gorte, J. T. S. Irvine, A. J. McEvoy, M. Mogensen, S. C. Singhal, J. Vohs, *Nat. Mater.* **2004**, *3*, 17–27.
[7] S. He, S. P. Jiang, *Prog. Nat. Sci.* **2021**, *31*, 341–372.
[8] A. J. Jacobson, *Chem. Mater.* **2010**, *22*, 660.
[9] M. S. Khan, X. Xu, R. Knibbe, Z. Zhu, *Renewable Sustainable Energy Rev.* **2021**, *143*, 110918.
[10] A. Momma, T. Kato, Y. Kaga, S. Nagata, *J. Ceram. Soc. Jpn.* **1997**, *105*, 369–373.
[11] K. Chen, S. P. Jiang, *Int. J. Hydrogen Energy* **2011**, *36*, 10541–10549.
[12] S. N. Rashkeev, M. V. Glazoff, *Int. J. Hydrogen Energy* **2012**, *37*, 1280–1291.
[13] M. A. Laguna-Bercero, R. Campana, A. Larrea, J. A. Kilner, V. M. Orera, *J. Power Sources* **2011**, *196*, 8942–8947.
[14] J. A. Labrincha, J. R. Frade, F. M. Marques, *J. Mater. Sci.* **1993**, *28*, 3809.
[15] K. Yang, J. H. Shen, K. Y. Yang, I. M. Hung, K. Z. Fung, M. C. Wang, *J. Power Sources* **2006**, *159*, 63.
[16] Y. Huang, J. M. Vohs, R. J. Gorte, *J. Electrochem. Soc.* **2006**, *153*, A951.
[17] A. Chen, J. R. Smith, K. L. Duncan, R. T. DeHoff, K. S. Jones, E. D. Wachsman, *J. Electrochem. Soc.* **2010**, *157*, B1624.
[18] M. Keane, M. K. Mahapatra, A. Verma, P. Singh, *Int. J. Hydrogen Energy* **2012**, *37*, 16776–16785.
[19] K. Chen, S. P. Jiang, *J. Electrochem. Soc.* **2016**, *163*, F3070–F3083.
[20] J. Kim, H. I. Ji, H. P. Dasari, D. Shin, H. Song, J. H. Lee, B. K. Kim, H. J. Je, H. W. Lee, K. J. Yoon, *Int. J. Hydrogen Energy* **2013**, *38*, 1225–1235.
[21] H. Kumigashira, K. Horiba, H. Ohguchi, K. Ono, M. Oshima, N. Nakagawa, M. Lippmaa, M. Kawasaki, H. Koinuma, *Appl. Phys. Lett.* **2003**, *82*, 3430–3432.
[22] K. Katsiev, B. Yildiz, K. Balasubramaniam, P. A. Salvador, *Appl. Phys. Lett.* **2009**, *95*, 4–7.
[23] A. K. Huber, M. Falk, M. Rohnke, B. Luerssen, M. Amati, L. Gregoratti, D. Hesse, J. Janek, *J. Catal.* **2012**, *294*, 79–88.
[24] W. Lee, J. W. Han, Y. Chen, Z. Cai, B. Yildiz, *J. Am. Chem. Soc.* **2013**, *135*, 7909–7925.
[25] S. P. Jiang, J. G. Love, *Solid State Ion.* **2001**, *138*, 183–190.
[26] N. Caillol, M. Pijolat, E. Siebert, *Appl. Surf. Sci.* **2007**, *253*, 4641–4648.
[27] X. Yang, J. Hardy, C. A. Coyle, J. F. Bonnett, S. M. Mahseredjian, J. W. Stevenson, *J. Electrochem. Soc.* **2022**, *169*, 024512.
[28] H. P. Buchkremer, U. Dieckmann, D. Stöver, in *Second European Solid Oxide Fuel Cell Forum*, Proceedings Vol. 1 (Ed.: Ulf Bossel), Oslo, **1996**, p. 221.
[29] V. A. Haanappel, J. Mertens, D. Rutenbeck, C. Tropartz, W. Herzhof, D. Sebold, F. Tietz, *J. Power Sources* **2005**, *141*, 216–226.
[30] S. P. Jiang, *J. Mater. Sci.* **2008**, *43*, 6799–6833.
[31] G. Chen, Y. Gao, Y. Luo, R. Guo, *Ceram. Int.* **2017**, *43*, 1304–1309.
[32] J. Liu, Y. Yu, T. Yang, O. Ozmen, H. Finklea, E. M. Sabolsky, H. Abernathy, P. R. Ohodnicki, G. A. Hackett, *ECS Trans.* **2017**, *78*, 689.
[33] Y. Song, X. Zhang, Y. Zhou, Q. Jiang, F. Guan, H. Lv, G. Wang, X. Bao, *Energy Storage Mater.* **2018**, *13*, 207–214.
[34] T. Wu, W. Zhang, Y. Li, Y. Zheng, B. Yu, J. Chen, X. Sun, *Adv. Energy Mater.* **2018**, *8*, 1–7.
[35] M. S. Khan, X. Xu, J. Zhao, R. Knibbe, Z. Zhu, *J. Power Sources* **2017**, *359*, 104–110.
[36] Y. Wang, W. Li, L. Ma, W. Li, X. Liu, *J. Mater. Sci. Technol.* **2020**, *55*, 35–55.
[37] B. Koo, K. Kim, J. K. Kim, H. Kwon, J. W. Han, W. C. Jung, *Joule* **2018**, *2*, 1476–1499.
[38] K. Chen, S. P. Jiang, *Electrochem. Energy Rev.* **2020**, *3*, 730–765.
[39] H. Türk, F.-P. Schmidt, T. Götsch, F. Girgsdies, A. Hammud, D. Ivanov, I. C. Vinke, L. De Haart, R.-A. Eichel, K. Reuter, R. Schlögl, A. Knop-Gericke, C. Scheurer, T. Lunkenbein, *Adv. Mater. Interfaces* **2021**, *8*, 2100967.
[40] T. Götsch, H. Türk, F.-P. Schmidt, I. C. Vinke, L. De Haart, R. Schlögl, K. Reuter, R.-A. Eichel, A. Knop-Gericke, C. Scheurer, T. Lunkenbein, *ECS Trans.* **2021**, *103*, 1331–1337.
[41] S. J. Dillon, M. Tang, W. C. Carter, M. P. Harmer, *Acta Mater.* **2007**, *55*, 6208–6218.
[42] P. R. Cantwell, M. Tang, S. J. Dillon, J. Luo, G. S. Rohrer, M. P. Harmer, *Acta Mater.* **2014**, *62*, 1–48.
[43] A. Kundu, K. M. Asl, J. Luo, M. P. Harmer, *Scr. Mater.* **2013**, *68*, 146–149.
[44] A. R. Krause, P. R. Cantwell, C. J. Marvel, C. Compson, J. M. Rickman, M. P. Harmer, *J. Am. Ceram. Soc.* **2018**, *102*, 778–800.
[45] P. Xu, W. Rheinheimer, S. N. Shuvo, Z. Qi, O. Levit, H. Wang, Y. Ein-Eli, L. A. Stanciu, *ChemElectroChem* **2019**, *6*, 4576–4585.
[46] J. Luo, *Energy Storage Mater.* **2019**, *21*, 50–60.
[47] J. Timmermann, F. Kraushofer, N. Resch, P. Li, Y. Wang, Z. Mao, M. Riva, Y. Lee, C. Staacke, M. Schmid, C. Scheurer, G. S. Parkinson, U. Diebold, K. Reuter, *Phys. Rev. Lett.* **2020**, *125*, 206101.
[48] S. Stegmaier, R. Schierholz, I. Povstugar, J. Barthel, S. P. Rittmeyer, S. Yu, S. Wengert, S. Rostami, H. Kungl, K. Reuter, R. A. Eichel, C. Scheurer, *Adv. Energy Mater.* **2021**, *11*, 2100707.
[49] L. Masliuk, F.-P. Schmidt, W. Hetaba, M. Plodinec, G. Auffermann, K. Hermann, D. Teschner, F. Girgsdies, A. Trunschke, R. Schlögl, T. Lunkenbein, *J. Phys. Chem. C* **2020**, *124*, 23069–23077.
[50] K. Reuter, *Catal. Lett.* **2016**, *146*, 541–563.
[51] P. Potapov, A. Lubk, *Micron* **2021**, *145*, 103068.
[52] N. Braidy, R. Gosselin, *Sci. Rep.* **2019**, *9*, 18797.
[53] S. Cacovich, F. Matteocci, M. Abdi-Jalebi, S. D. Stranks, A. Di Carlo, C. Ducati, G. Divitini, *ACS Appl. Energ. Mater.* **2018**, *1*, 7174–7181.
[54] P. Potapov, P. Longo, E. Okunishi, *Micron* **2017**, *96*, 29–37.
[55] J. Titchmarsh, *Micron* **1999**, *30*, 159–171.
[56] J. Titchmarsh, S. Dumbill, *J. Microsc.* **1996**, *184*, 195–207.
[57] M. Shiga, K. Tatsumi, S. Muto, K. Tsuda, Y. Yamamoto, T. Mori, T. Tanji, *Ultramicroscopy* **2016**, *170*, 43–59.
[58] B. R. Jany, A. Janas, F. Krok, *Nano Lett.* **2017**, *17*, 6520–6525.

[59] N. H. Timm, in *Applied Multivariate Analysis*, Springer-Verlag New York, **2004**.
[60] W. K. Härdle, L. Simar, in *Applied Multivariate Statistical Analysis*, 3rd ed., Springer-Verlag Berlin Heidelberg, **2012**.
[61] K. Devarajan, *PLoS Comput. Biol.* **2008**, *4*, e1000029.
[62] A. R. McIntosh, B. Mišić, *Annu. Rev. Psychol.* **2013**, *64*, 499–525.
[63] M. Chang, in *Modern Issues and Methods in Biostatistics*, Springer Science + Business Media, **2019**.
[64] P. Potapov, P. Longo, E. Okunishi, *Micron* **2017**, *96*, 29–37.
[65] P. Potapov, A. Lubk, *Adv. Struct. Chem. Imaging* **2019**, *5*, 4.
[66] G. Lucas, P. Burdet, M. Cantoni, C. Hébert, *Micron* **2013**, *52–53*, 49–56.
[67] N. Dobigeon, N. Brun, *Ultramicroscopy* **2012**, *120*, 25–34.
[68] P. Cao, P. Tang, M. F. Bekheet, H. Du, L. Yang, L. Haug, A. Gili, B. Bischoff, A. Gurlo, M. Kunz, R. E. Dunin-Borkowski, S. Penner, M. Heggen, *J. Phys. Chem. C* **2022**, *126*, 786–796.
[69] Đ. Tripković, J. Wang, R. Küngas, M. B. Mogensen, B. Yildiz, P. V. Hendriksen, *Chem. Mater.* **2022**, *34*, 1722–1736.
[70] J. M. Polfus, B. Yildiz, H. L. Tuller, *Phys. Chem. Chem. Phys.* **2018**, *20*, 19142–19150.
[71] M. P. De Jong, I. Bergenti, V. A. Dediu, M. Fahlman, M. Marsi, C. Taliani, *Phys. Rev. B* **2005**, *71*, 2–5.
[72] M. Backhaus-Ricoult, K. Adib, T. St. Clair, B. Luerssen, L. Gregoratti, A. Barinov, *Solid State Ion.* **2008**, *179*, 891–895.
[73] M. Rohnke, K. Schaepe, A. K. Bachmann, M. Laenger, J. Janek, *Appl. Surf. Sci.* **2017**, *422*, 817–827.
[74] Q. H. Wu, M. Liu, W. Jaegermann, *Mater. Lett.* **2005**, *59*, 1980–1983.
[75] T. T. Fister, D. D. Fong, J. A. Eastman, P. M. Baldo, M. J. Highland, P. H. Fuoss, K. R. Balasubramaniam, J. C. Meador, P. A. Salvador, *Appl. Phys. Lett.* **2008**, *93*, 1–4.
[76] D. Kim, R. Bliem, F. Hess, J. J. Gallet, B. Yildiz, *J. Am. Chem. Soc.* **2020**, *142*, 3548–3563.
[77] F. Hess, B. Yildiz, *J. Chem. Phys.* **2021**, *154*, 064702.
[78] M. A. Fischler, R. C. Bolles, *Commun. ACM* **1981**, *24*, 381–395.
[79] J. Hedderich, L. Sachs, *Angewandte Statistik*, 16th ed., Springer-Verlag GmbH Deutschland, **2018**, pp. 445–470.
[80] M. A. Niania, R. Podor, T. B. Britton, S. J. Skinner, J. A. Kilner, *Microsc. Microanal.* **2016**, *22*, 10–11.
[81] S. Tanuma, C. J. Powell, D. R. Penn, *Surf. Interface Anal.* **2003**, *35*, 268–275.
[82] R. Vasquez, *J. Electron Spectrosc. Relat. Phenom.* **1991**, *56*, 217–240.
[83] M. I. Sosulnikov, Y. A. Teterin, *Doklady AN SSSR* **1991**, *317*, 418.
[84] S. Plimpton, *J. Comput. Phys.* **1995**, *117*, 1–19.
[85] S. van der Walt, J. L. Schönberger, J. Nunez-Iglesias, F. Boulogne, J. D. Warner, N. Yager, E. Gouillart, T. Yu, *PeerJ* **2014**, *2*, e453.
[86] F. Pedregosa, G. Varoquaux, A. Gramfort, V. Michel, B. Thirion, O. Grisel, M. Blondel, P. Prettenhofer, R. Weiss, V. Dubourg, J. Vanderplas, A. Passos, D. Cournapeau, M. Brucher, M. Perrot, E. Duchesnay, *J. Mach. Learn. Res.* **2011**, *12*, 2825–2830.
[87] J. J. Yeh, I. Lindau, *At. Data Nucl. Data Tables* **1985**, *32*, 1–155.

Manuscript received: March 1, 2022
Revised manuscript received: July 5, 2022
Accepted manuscript online: July 8, 2022
Version of record online: August 1, 2022

Paper 3

Assessing Deep Generative Models in Chemical Composition Space

Hanna Türk*, Elisabetta Landini*, Christian Kunkel*, Johannes Margraf, and Karsten Reuter

Chem. Mater. **2022**, *34*, 9455.

*These authors contributed equally to the work.

CHEMISTRY OF MATERIALS

pubs.acs.org/cm

Article

Assessing Deep Generative Models in Chemical Composition Space

Hanna Türk,[§] Elisabetta Landini,[§] Christian Kunkel,[§] Johannes T. Margraf,* and Karsten Reuter

Cite This: *Chem. Mater.* 2022, 34, 9455−9467

Read Online

ACCESS | Metrics & More | Article Recommendations | Supporting Information

ABSTRACT: The computational discovery of novel materials has been one of the main motivations behind research in theoretical chemistry for several decades. Despite much effort, this is far from a solved problem, however. Among other reasons, this is due to the enormous space of possible structures and compositions that could potentially be of interest. In the case of inorganic materials, this is exacerbated by the combinatorics of the periodic table since even a single-crystal structure can in principle display millions of compositions. Consequently, there is a need for tools that enable a more guided exploration of the materials design space. Here, generative machine learning models have recently emerged as a promising technology. In this work, we assess the performance of a range of deep generative models based on reinforcement learning, variational autoencoders, and generative adversarial networks for the prototypical case of designing Elpasolite compositions with low formation energies. By relying on the fully enumerated space of 2 million main-group Elpasolites, the precision, coverage, and diversity of the generated materials are rigorously assessed. Additionally, a hyperparameter selection scheme for generative models in chemical composition space is developed.

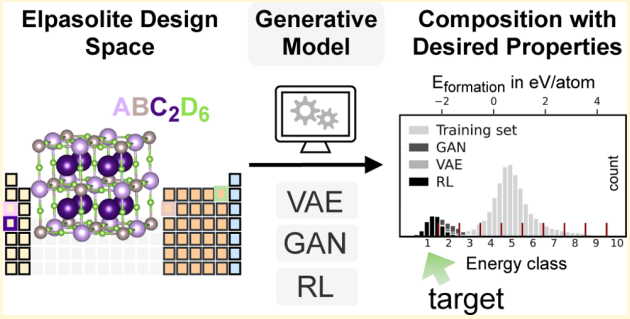

1. INTRODUCTION

Generative machine learning (ML) models are increasingly used for the targeted generation of images,[1] video sequences,[2] text,[3] or music.[4] This can be achieved by approximately representing the underlying data distribution as inferred from a provided data set and sampling from this distribution. Alternatively, the underlying "construction rules" of a dataset can be learned from examples without taking the underlying distribution into account explicitly. Ultimately, both approaches provide access to the novel but realistic examples, which incorporate the decisive features of the training data.

In the context of organic chemistry, such ML models have already been successfully applied for the inverse design of novel molecular candidates.[5,6] Rather than using an explicit set of rules that link molecular fragments to new molecules, the underlying wealth of construction principles is captured from data in the training phase,[7−9] often using existing (public) libraries of organic molecules presented to the model. The generation process then allows for overcoming the limitations of the initially presented molecular library[10−14] by accessing molecules with a wide variety of chemical functionalities that are still consistent with the training examples.

Beyond merely proposing realistic molecules, molecular design typically additionally demands the focused generation of candidates with desired properties. This can be achieved[15] by enhancing generative approaches via transfer learning,[16−20] semisupervised learning,[21,22] conditional generation,[21−26] reinforcement learning,[27−30] or by carrying out optimization in a well-structured (latent) representation space.[31−33]

In essence, this molecular design toolbox can equally be applied to the proposition of novel and useful inorganic materials for catalysis, energy conversion, or other applications. However, inorganic materials present notable challenges in this regard. This is because, on the one hand, a suitable (i.e., invertible) material representation that respects the symmetry and the periodicity of a three-dimensional crystal and is (ideally) independent of the number of atoms in the unit cell is not trivial to define.[34] On the other hand, a much larger variety of chemical compositions are possible for inorganic systems. The current paper will focus on the latter aspect.

In the prevailing data scarcity, inverse design of inorganic materials has usually focused more on structural prediction in limited composition spaces[35−40] or compositional optimization with fixed structural prototypes.[41−43] However, even if trained on a limited subset of structure types, it has been shown that these models are able to generalize to new structure types that were not included in the training process.[34]

Deep generative frameworks employing neural networks (NNs) have proven to be an invaluable tool in this context.[44] Notably, these comprise a large zoo of approaches, including variational autoencoders (VAEs),[34−36,39,42,45−47] generative

Received: June 22, 2022
Revised: October 5, 2022
Published: October 19, 2022

adversarial networks (GANs),[37,38,41−43,48,49] and reinforcement learning (RL).[50,51] Given this wide range of approaches, it is a priori difficult to decide which method should be used for a new inverse design task.

While different ML models can be compared objectively by checking their predictive accuracy on an unseen test set for regression or classification tasks, this is much less straightforward for generative models, where each model generates new data independently. Here, one must instead evaluate to what extent the new data covers the underlying distribution of the training set and how well it generalizes to new samples that are unlike the training examples.[11−13,52] Furthermore, in the context of targeted materials design, an important question is whether the proposed candidates reliably display the desired properties.

Due to these questions, comparative studies which have been performed for organic molecule generation[11−14,52,53] and (less frequently) inorganic materials,[54] are particularly valuable. Aiming to establish deeper insight into the advantages and disadvantages of the variety of generative frameworks for inorganic materials design, we here embark on such a comparative study. Specifically, we use the targeted search for novel, stable compositions within a fixed structural prototype as a suitable benchmark for comparing the performance of three prevalent generative ML approaches (VAE, GAN, and RL).

To this end, we rely on a well-established computational data set of Elpasolite structures reported by Faber et al.,[55] which has previously served as a benchmark for regression models.[56−60] This set comprises the fully enumerated space of nearly 2 million systems, which can be derived by the main-group elemental exchange on the pristine quaternary Elpasolite mineral $AlNaK_2F_6$. Notably, this mineral is part of the quaternary double-perovskite prototype ABC_2D_6, which is of significant technological interest.

Relying on the distribution provided by this fully enumerated chemical composition space, we demonstrate that straightforward realizations of different generative frameworks using simple NN architectures can reliably generate promising material candidates. Noting the plethora of algorithmic ramifications and subtleties in hyperparameter settings in each generative model class, we define general performance metrics with regard to the diversity, coverage, and fitness of the proposed materials. With this, we hope to establish a well-defined and representative benchmark problem for future assessment and tailoring of generative models.

2. METHODS

2.1. Dataset and Material Representation. The prototypical Elpasolite mineral ABC_2D_6 is reproduced in Figure 1a. The complete Elpasolite material space considered herein then emerges from all possible combinations of main-group elements (from H to Bi, 39 overall) on the four lattice sites (A, B, C, and D), leading to 1,974,024 possible structures. In ref 55, formation energies $E_{\text{formation}}^{\text{DFT}}$ computed at the PBE level are reported for a subset of 10,590 structures (assuming perfect cubic symmetry). Additionally, that work also provides accurate estimates of $E_{\text{formation}}^{\text{regression}}$ for the remaining structures, predicted by a kernel ridge regression (KRR) model with a mean absolute error of 0.1 eV; see Figure 1e,f. In the following, we use DFT values to train the conditional generative models, while estimated values from the KRR model are used to gauge the quality of generated samples. All formation energies are given per atom.

To represent different Elpasolites, we employ a simplified version of the bag-of-atoms[42] representation, closely following Faber et al.[55]

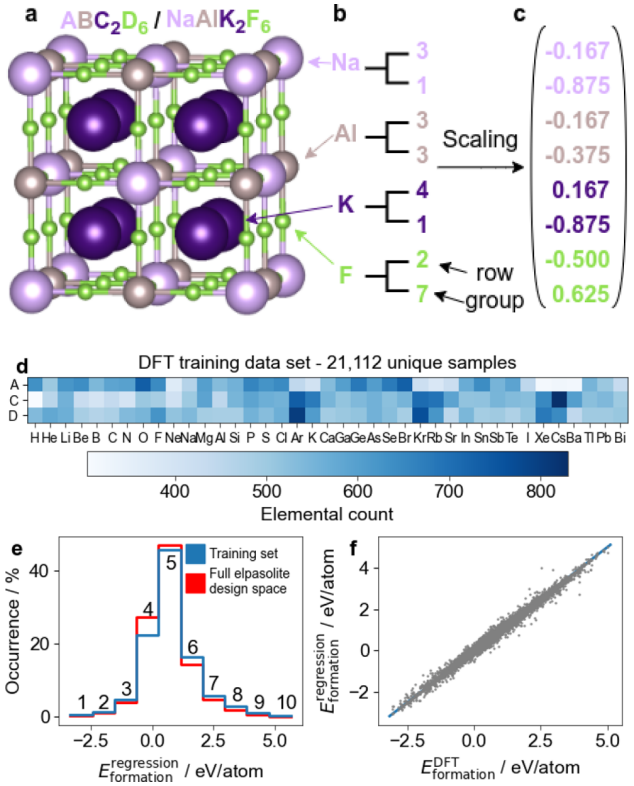

Figure 1. (a) Prototypical Elpasolite structure ABC_2D_6. (b) 8D representation of the Elpasolite elemental composition by row and main group number in the periodic table exemplified for $AlNaK_2F_6$. (c) Scaling of the 8D representation by eq 1. (d) Elemental distribution of the training dataset. (e) Formation energy distribution of DFT training and the full reference data set from ref 55, split into 10 equal-range energy classes, see text. (f) Formation energy of the DFT data vs the predicted one from the regression model.

In this way, each composition is represented by an eight-dimensional vector x_{8D}. As illustrated in Figure 1b, its entries correspond to the row number n_{row} (ranging from 1 to 6) and the main-group number n_{group} (ranging from 1 to 8) of each of the four sites in the structure. The different absolute ranges of the row and main-group entries in the vector are thereby normalized to the common interval (−1,1) by rescaling to

$$x_{8D,\text{scaled}} = \frac{2x_{8D} - 1}{n_{\text{row/group}}} - 1 \quad (1)$$

Note that this representation also encodes structures with nonexistent elements (e.g., first-row elements of group number 2−7) or structures with repeated elements. The generative models can therefore in principle also generate such invalid structures. However, as structure generation is not a time-limiting factor and the proportion of invalid compositions is generally low, we simply disregard invalid samples, rather than fixing this shortcoming of the compositional representation.

It should further be noted that the A and B sites are equivalent in the Elpasolite structure, so that structure ABC_2D_6 should have the same formation energy as BAC_2D_6. This permutational symmetry is not exploited in the DFT training set of ref 55. Indeed, there are only 34 occurrences where both structures are contained (with slightly different DFT formation energies deviating on average by 2.3 meV/atom). As part of our data curation, we augmented the DFT training set by consistently adding all A/B permutations, obtaining a final DFT training set size of 21,112 structures.

Figure 1d depicts the elemental distribution of the final training set. The corresponding DFT formation energies range from −3.07 to

https://doi.org/10.1021/acs.chemmater.2c01860
Chem. Mater. 2022, 34, 9455−9467

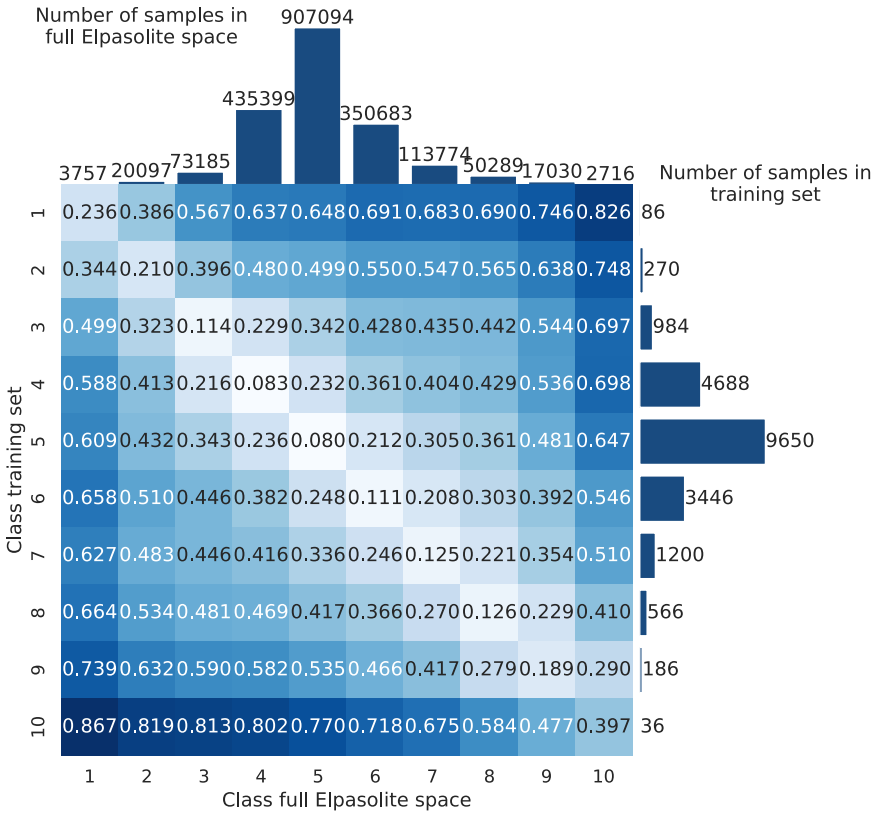

Figure 2. Reference JS distances between the training set and the full Elpasolite space.

5.02 eV/atom, with a negative value indicating stability with respect to elemental decomposition. In order to conditionally generate samples in given stability ranges, the training data was split into 10 classes, each containing an equal span of 0.81 eV/atom on the $E_{\text{formation}}^{\text{DFT}}$ scale. Class 1 spans the lowest formation energies and thus the most stable Elpasolite compositions, while class 10 spans the highest formation energies and thus the least stable compositions. When necessary for conditional training, these classes are encoded into a 10-dimensional one-hot vector, which is concatenated to the structural representation discussed above. Note that this division into classes is mainly performed in order to simplify the subsequent analysis of the models. It would also be possible to directly condition the models on the formation energy.

During training, batches are formed by randomly sampling training compositions with a probability that is the inverse of the frequency with which the corresponding energetic class appears in the DFT training set. This weighted sampling allows us to mitigate the class imbalance in the DFT training set, that is, the fact that, for example, much fewer samples are in class 1 than in class 5 as apparent in Figure 1e. Note that all cost functions below are defined for a single training example, for notational convenience. Extension to batch-based training is straightforward. For practical implementation, a common interface to the data set is provided by a custom data loader. This code implements the described preprocessing steps and handles the balanced sampling of batches during the training of the generative models. For reference and further benchmarks, the Python code is freely available at https://gitlab.mpcdf.mpg.de/fhi-theory/elpasolite_generative_model_assessment.

2.2. Performance Metrics. Using the DFT training set, we build deep generative models for the inverse design of Elpasolite compositions. Ideally, these models should (i) propose compositions in a targeted energy class with high *precision*, (ii) yield a high *diversity* among the proposed compositions, and (iii) display high *coverage* of the chemical composition space. While the first of these is directly enforced by the conditional generation (and in the RL reward), diversity and coverage are more subtle factors. Indeed, so-called mode- or posterior collapse is commonly observed in GAN[61] or VAE models,[62,63] ultimately resulting in a limited number of samples that the models can generate.

To assess these factors, we exploit the fact that the full Elpasolite composition space is known from the prior work of Faber et al.[55] We thus know the total number of N_{class} of compositions in each class (see Figure 1e) and the elemental distributions on the four sites (A, B, C, and D) in each class. Based on this, we define the following quantitative performance metrics:

(1) Precision (right class) measures the model's ability to generate samples in the desired class. To this end, the fraction of generated compositions that actually fall into the desired class is computed

$$\text{precision (right class)} = \frac{N_{\text{class}}^{\text{gen}}}{N^{\text{gen}}} \tag{2}$$

where N^{gen} is the total number of generated samples and $N_{\text{class}}^{\text{gen}}$ is the number of generated samples which belong to the desired class. This means that high precision is achieved if the model reliably produces samples in the desired class. Note however that this can also be achieved from only a few repetitively produced samples (or even by memorizing the training set).

(2) Precision (neighboring class) analogously measures the fraction of samples falling into the classes just above or below the requested class

$$\text{precision (neigh. class)} = \frac{N_{\text{class}-1}^{\text{gen}} + N_{\text{class}+1}^{\text{gen}}}{N^{\text{gen}}} \tag{3}$$

This allows capturing the tails of the predicted formation energy distributions. Since the models are trained on DFT data but evaluated using the approximate KRR energetics for the full Elpasolite space, this metric captures the residual uncertainty in the definition of the energy classes.

(3) Coverage (right class) measures the fraction of unique compositions in the desired class that could be generated by the model

https://doi.org/10.1021/acs.chemmater.2c01860
Chem. Mater. 2022, 34, 9455−9467

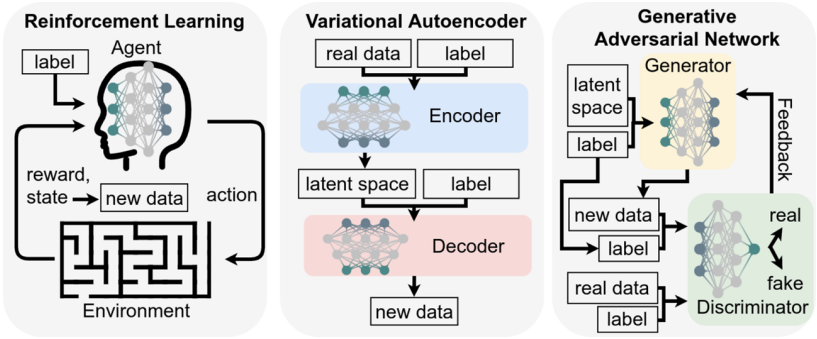

Figure 3. Schematic overview of the generative frameworks compared in this study.

$$\text{coverage (right class)} = \frac{N^{\text{gen}}_{\text{class,un.}}}{N_{\text{class}}} \tag{4}$$

where $N^{\text{gen}}_{\text{class,un.}}$ is the number of unique compositions generated in the desired class.

(4) Coverage (neighboring class) analogously measures the fraction of unique compositions in the classes just above or below the requested class

$$\text{coverage (neigh. class)} = \frac{N^{\text{gen}}_{\text{class}-1,\text{un.}} + N^{\text{gen}}_{\text{class}+1,\text{un.}}}{N_{\text{class}-1,\text{un.}} + N_{\text{class}+1,\text{un.}}} \tag{5}$$

(5) The Jensen−Shannon (JS) distance measures how strongly the elemental distribution in the generated examples differs from the corresponding distribution in the full Elpasolite composition space (for a given class). Specifically, we consider probabilities $p(Z|S)$ of finding element Z on site S in a given dataset. To compare two such probability distributions, we use the JS distance d_{JS}, which provides intuitively interpretable values between 0 and 1 (with 0 indicating that the distributions are identical and 1 indicating no overlap at all). For two elemental distributions p and q, this is calculated as

$$d_{\text{JS}}(p||q) = \frac{1}{4}\sum_S \sum_Z \left[\frac{1}{2}p(Z|S)\log_2\left(\frac{p(Z|S)}{m(Z|S)}\right) + \frac{1}{2}q(Z|S)\log_2\left(\frac{q(Z|S)}{m(Z|S)}\right)\right]^{1/2} \tag{6}$$

where the first sum runs over all sites A, B, C, and D, the second sum runs over all elements in the Elpasolite dataset, and $m(Z|S) = 1/2[p(Z|S) + q(Z|S)]$.

To provide some reference values for the JS distance, we compare the elemental distributions corresponding to different classes in the training set and the full Elpasolite space in Figure 2. This shows that identical classes have low JS distances between training and full sets, while different classes have high distances. Unsurprisingly, the distance for identical classes is lower when many examples are included in the training set (i.e., for class 5). Furthermore, the distances change smoothly across the classes, so the distance between class 1 and class 2 is lower than the distance between class 1 and class 5. Overall, values of 0.25 or lower can be considered as a good agreement between the distributions.

2.3. Generative Frameworks. Our comparative study specifically covers the three deep generative frameworks shown in Figure 3. The ideas behind the three models differ fundamentally. In RL, an *agent* constructs the materials in a step-wise procedure. During training, the agent receives feedback about the quality of the samples (i.e., whether they fall into the desired class) and thus improves its decision-making *policy*. In contrast, VAEs and GANs are both trained to generate data similar to the training examples when sampling from a low-dimensional latent space. Both models therefore effectively learn a (conditional) probability distribution of material compositions. However, the way this is achieved differs markedly. On the one hand, the VAE consists of an *encoder* network, which maps training samples to latent space, and a *decoder* network, which reconstructs them back. On the other hand, the GAN uses an adversarial principle. A *generator* network is trained to translate random samples from latent space to realistic material representations. In parallel, a *discriminator* is trained to distinguish the "fake" samples from the generator and the "real" samples from the training set. Through a feedback process, the generator ultimately learns to fool the discriminator.

To implement the three models, we employ fully connected multilayered artificial NNs. This is the simplest and most general NN architecture, and it is not specifically tailored to the problems at hand. The corresponding generative models therefore serve to establish simple baselines, while specifically tailored architectures may display even better performance. All models are implemented using PyTorch (v1.9.0) and executed with Python (v3.8.8).

As a nonlinearity after every hidden layer, the commonly used LeakyReLU[64] function is used with a negative slope of 0.2. Based on the model-dependent cost function, the free parameters (weights and biases) of these networks are updated by gradient descent using the Adam optimizer[65] and gradients obtained through backpropagation. While some of the illustrations below are based on one representative model fit, all reported performance metrics are obtained from 50 separate model initializations, unless otherwise stated.

As is always the case for deep learning models, a variety of additional hyperparameters must be set to determine the NN architecture (e.g., the number of hidden layers and neurons per layer) and training procedure (e.g., the learning rate and batch size). We optimize these model- and training hyperparameters with respect to two objective functions, which can be cheaply computed against the training set: (1) the model's ability to reproduce the elemental distribution occurring in the targeted lowest formation energy class of the training set (practically measured by the JS distance[12]) and (2) the model's ability to generate an overall large number of unique new samples not contained in the training set. To identify suitable combinations of hyperparameters, a simple random search[66] was performed. See Table S4 for a listing of all searched parameters and their ranges. Figure S4 and Tables S5−S7 fully detail the procedure.

2.3.1. Variational Autoencoder. The generation of high-dimensional data with VAEs[67,68] proceeds as follows: a low-dimensional latent space vector $\mathbf{z}$ is drawn from a predefined probability distribution and mapped to a realistic data point $\tilde{\mathbf{x}}$ by a NN P_ϕ called the *decoder* (with trainable parameters ϕ).

$$\tilde{\mathbf{x}} = P_\phi(\mathbf{z}) \tag{7}$$

During training, the decoder is paired with a second trainable NN—the *encoder*Q_θ (with trainable parameters θ). The encoder takes a sample $\mathbf{x}_i$ from the training set and produces a representation of this data point in the latent space. Importantly, VAEs use a probabilistic mapping for this purpose: each input sample $\mathbf{x}_i$ is mapped to a multivariate normal distribution N in latent space so that the output of the encoder is a vector of means $\boldsymbol{\mu}(\mathbf{x}_i)$ and variances $\boldsymbol{\sigma}^2(\mathbf{x}_i)$. The corresponding probability distribution $q_\theta(\mathbf{z}|\mathbf{x}_i)$ in latent space is thus defined as

https://doi.org/10.1021/acs.chemmater.2c01860
Chem. Mater. 2022, 34, 9455−9467

$$q_\theta(\mathbf{z}|\mathbf{x}_i) = \mathcal{N}(\boldsymbol{\mu}(\mathbf{x}_i), \boldsymbol{\sigma}^2(\mathbf{x}_i)) \tag{8}$$

Here, the subscript θ indicates that this probability distribution depends on the trainable parameters of the encoder Q_θ.

Ideally, the decoder should be able to reconstruct $\mathbf{x}_i$ as accurately as possible, given a random sample $\mathbf{z}_\epsilon$ from the distribution $q_\theta(\mathbf{z}|\mathbf{x}_i)$. Furthermore, the probabilistic mapping of the training data should be smooth and continuous in latent space to obtain an effective generative model. This is achieved by training the VAE with a combined cost function $J(\phi, \theta)$, defined as

$$J(\mathbf{x}_i|\phi, \theta) = \underbrace{(\mathbf{x}_i - P_\phi(\mathbf{z}_\epsilon))^2}_{\text{reconstruction}} + \underbrace{\lambda D_{\mathrm{KL}}(q_\theta(\mathbf{z}|\mathbf{x}_i)||\mathcal{N}(0,1))}_{\text{regularization}} \tag{9}$$

Here, the reconstruction term is simply the squared deviation between the original and reconstructed input. The regularization term is given by the Kullback−Leibler divergence[69] D_{KL}, which quantifies the statistical distance between the learned distribution $q_\theta(\mathbf{z}|\mathbf{x}_i)$ and a multivariate normal distribution with zero means and unit variances.

Minimizing this combined cost function during training requires finding a trade-off between reconstruction and regularization. Intuition about this process can be gained from looking at the two terms separately. If only the reconstruction term was included, the model would be very accurate in reproducing the training set, but its generalization capability toward novel compositions would suffer. Similarly, if the regularization prevails and only the Kullback−Leibler divergence is minimized, the decoder would resort to generating very few unique samples and instead output an average representation of the training set (since all inputs $\mathbf{x}_i$ would be mapped to the same latent space distribution). This latter problem is known as posterior collapse.[63,70] To balance between these extremes, the regularization parameter λ in the loss can be adjusted.

As described so far, the VAE would simply propose materials from the full chemical composition space. For a targeted generation of materials with specific properties, we operate the VAE as a conditional model.[71,72] Such class-conditional learning can easily be incorporated while keeping a similar training procedure. To this end, both the encoder and the decoder receive the class label of each training sample, which is concatenated with their respective inputs. After training, the decoder can then generate new samples from a specific class when provided with a random latent space vector and the desired class label.

Following the hyperparameter search described above, the final VAE models used below are constructed as follows: the class-conditional input $x_{18\mathrm{D}}$ is encoded to an eight-dimensional latent space, and decoded into the scaled eight-dimensional representation of the composition. Both the encoder and decoder NNs have 2 hidden layers with 256 nodes. Layer normalization[73] is employed. The final output function of the decoder is a hyperbolic tangent that returns values between −1 and 1. All models were trained for 10,000 network updates on batches of 500 samples each, using the Adam optimizer with a learning rate of 0.001. The regularization parameter λ in the loss is fixed at 0.1.[62]

2.3.2. Generative Adversarial Network. Similar to the VAE, the GAN[74] framework uses a generator model G_θ (with trainable parameters θ), which is trained to generate realistic synthetic samples $\tilde{\mathbf{x}} = G_\theta(\mathbf{z})$ from a random latent space vector $\mathbf{z}_\epsilon$. Training of G_θ thereby follows an adversarial approach, which can be understood as a contest between G_θ and a discriminator model D_ϕ (with trainable parameters ϕ). The role of D_ϕ is to discriminate between real samples from the training set and the synthetic samples created by G_θ. The feedback from D_ϕ is in turn used to maximize the ability of G_θ to generate increasingly realistic samples, essentially trying to fool D_ϕ into misclassification. Over the course of this competition, both models successively improve.

While this idea is highly intuitive, successfully training a GAN can be challenging. For example, a commonly observed problem[61] is the so-called mode collapse—where G_θ resorts to fooling D_ϕ by repetitively generating the same highly convincing samples. Intensive research has therefore been devoted to improving the training procedure of GANs. This has led to a series of different proposed cost functions and modified NN architectures that improve training stability[75] or generative performance.[76] We here rely on the Wasserstein GAN[77] with a gradient-penalty[78] term (WGAN-GP). In this framework, D_ϕ is usually referred to as a "critic" and returns a scalar value that represents the sample quality, instead of a mere binary classification of data as real or fake.

As for the VAE, D_ϕ and G_θ are represented by fully connected NNs herein, whose parameters are optimized during the adversarial training by gradient descent. Due to the adversarial nature of the GAN, two separate cost functions J_{D} and J_{G} are used for the discriminator and generator, respectively. The former is defined as

$$J_{\mathrm{D}}(\mathbf{x}_i|\phi, \theta) = \underbrace{-D_\phi(\mathbf{x}_i)}_{\text{real}} + \underbrace{D_\phi(G_\theta(\mathbf{z}_\epsilon))}_{\text{fake}} + \underbrace{\lambda \mathcal{P}(\mathbf{x}_i, G_\theta(\mathbf{z}_\epsilon))}_{\text{gradient penalty}} \tag{10}$$

Here, the first and second terms reward high scores for real and low scores for fake samples, respectively. Sparing the details,[78] the gradient-penalty term represents a practical solution to enforce a well-behaved critic function. Its evaluation depends on linearly interpolated data points between the real and fake data points. The recommended penalty coefficient $\lambda = 10$ is used throughout.[78]

Meanwhile, the cost function of the generator is simply

$$J_{\mathrm{G}}(\phi, \theta) = -D_\phi(G_\theta(\mathbf{z}_\epsilon)) \tag{11}$$

that is, it tries to maximize the score that D_ϕ assigns to the generated samples.

In analogy to the VAE, our model operates as a conditional GAN,[79,80] with sample class-conditional information provided to G_θ and D_ϕ alongside the input during training. After training, this again allows us to query the generator network for samples from the desired class.

Note that to achieve stable training, the parameters of D_ϕ are updated five times as frequently as θ_{G}.[78] Based on the hyperparameter optimization, the final models use one hidden layer with 512 nodes each for G_θ and D_ϕ. An eight-dimensional latent space vector is passed to G_θ and decoded to the structural representation $x_{8\mathrm{D,\ scaled}}$, again employing a hyperbolic tangent output layer. The networks are trained for 200,000 update steps on batches of 100 samples with a learning rate of 0.00001.

2.3.3. Reinforcement Learning. In RL an agent makes goal-oriented decisions in a successively evolving environment. To this end, a reward function is defined, which provides feedback about whether the actions of the agent lead to the desired outcomes. Because of this focus on acting in a complex environment, the classic fields of application of RL are the control of robots or other autonomous agents (e.g., in games). Nonetheless, RL has also been applied to the design of molecules and materials.[28,30,81−84]

In this case, the agent sequentially adds atoms or functional groups to a system. The main challenge associated with this is that the reward (e.g., as a measure of stability or the desired property) can only be determined for the complete system. It is therefore not straightforward to judge the quality of actions taken early on in the generation process (the so-called "credit assignment" or "sparse reward" problem). In this sense, designing a material is similar to a game of chess, where the reward (win/loose/draw) can only be determined at the end of the game.

In the context of this paper, a RL agent makes sequential decisions about the elemental composition of an Elpasolite, with the goal of the final formation energy being in the desired range. This step-wise process is illustrated for the composition of $KMgXe_2O_6$ (where the scaling of eq 1 is omitted for clarity)

https://doi.org/10.1021/acs.chemmater.2c01860
Chem. Mater. 2022, 34, 9455−9467

$$\underbrace{(\_\ \_\ \_\ \_\ \_\ \_\ \_\ \_)}_{\text{state 0}} \xrightarrow{\text{action 0}} \underbrace{(4\ \_\ \_\ \_\ \_\ \_\ \_\ \_)}_{\text{state 1}}$$

$$\underbrace{(4\ \_\ \_\ \_\ \_\ \_\ \_\ \_)}_{\text{state 1}} \xrightarrow{\text{action 1}} \underbrace{(4\ 1\ \_\ \_\ \_\ \_\ \_\ \_)}_{\text{state 2}}$$

$$\vdots$$

$$\underbrace{(4\ 1\ 3\ 2\ 5\ 8\ 2\ \_)}_{\text{state 7}} \xrightarrow{\text{action 7}} \underbrace{(4\ 1\ 3\ 2\ 5\ 8\ 2\ 6)}_{\text{state 8}}$$

The agent thus starts from an empty composition vector and chooses the row of the element at site A of the Elpasolite structure (see Figure 1). This leads to an updated composition vector and a new decision to make, namely, what the group of element A should be. In RL terminology, the composition vector defines the state s of the environment and each decision the agent makes is an action a, which leads to a new state s'. The generation process can thus be described as a sequence of state-action pairs $(s_0, a_0, s_1, a_1, ..., s_7, a_7, s_8)$, with a final state s_8. Such a structure generation sequence is called an *episode* (e) in the following.

During training, the agent receives a reward r after each action, which is based on the formation energy of the new state s', according to the classes introduced above. Specifically

$$r(s, a) = \begin{cases} 0 & \text{if } s' \text{ non-final} \\ 1 & \text{if } s' \text{final and in desired class} \\ -1 & \text{if } s' \text{final and not in desired class} \end{cases} \quad (12)$$

The key component of any RL model is the policy π, which is the algorithm used to decide on the next action of the agent based on the current state of the environment. Importantly, to overcome the sparse reward problem the policy cannot simply maximize the immediate reward for the current action. Indeed, this would be completely ineffective for the task at hand since the reward for most actions is zero. Instead, the ideal policy maximizes the sum of the current and all future rewards. This optimal long-term reward Q_* for a given state-action pair (s, a) is formalized by the Bellman equation

$$Q_*(s, a) = r(s, a) + \gamma \max_{a'} Q_*(s', a') \quad (13)$$

The optimal long-term reward $Q_*(s, a)$ (referred to as the *state-action value*) is thus recursively defined as a sum of the immediate reward $r(s, a)$ and the state-action value $Q_*(s', a')$, where a' is the action that maximizes $Q_*(s', a')$. The discount factor γ takes the potentially diminishing relevance of recursively included future actions into account. Specifically, by choosing $\gamma = 1$, all future rewards are weighted equally, whereas $\gamma \leq 1$ leads to a reduced impact of rewards that are acquired much after the action a.

Clearly, the state-action value Q_* in principle provides a sound basis for guiding the actions of an agent. However, it is generally only computable by exhaustively exploring all possible actions into the future, which would defeat the purpose of RL. The Q-learning approach[85] provides a way out of this problem as it allows the iterative approximation of Q_*. In the original Q-learning approach, this is achieved via a table of Q-values for all possible state-action combinations. This Q-table is iteratively updated as the agent explores the state space, according to

$$Q(s, a) = (1 - \alpha)Q(s, a) + \alpha(r(s, a) + \gamma \max_{a'} Q(s', a')) \quad (14)$$

where α is a learning rate. Although the Q-table is initialized with arbitrary values, this algorithm eventually converges to the true state-action values.

Relying on a Q-table is impractical for high-dimensional settings (such as materials design), however, because enumerating all possible states is in general not possible in this case. To overcome this limitation, the deep-Q network (DQN) approach was developed.[86] Here, the discrete Q-table is replaced by a NN Q_θ (with trainable parameters θ). This function takes any state s as an input and predicts the corresponding Q-values for all possible actions a.

To train this network, the cost function $J(\theta)$ defines a least-squares regression with eq 13 as the target value[85]

$$J(e_i, \theta) = \sum_{s,a \in e_i} [\underbrace{Q_\theta(s, a)}_{\text{prediction}} - \underbrace{r(s, a) + \gamma \max_{a'} Q_\theta(s', a')}_{\text{target}}]^2 \quad (15)$$

This function sums over the state-action pairs (s, a) of a given training episode e_i. Here, a peculiarity of DQNs compared to other deep learning methods is that both the prediction and the target value in the loss depend on Q_θ. This is directly analogous to conventional Q-learning, where the Q-values are updated based on the immediate reward $r(s, a)$ and other (randomly initialized) Q-values in the table. This works because the information about the reward $r(s, a)$ obtained at the end of each episode propagates to earlier state-action pairs as the training progresses.

It should be noted that the above description refers to the "batch" or "offline" RL setting,[87] which assumes a fixed training set of episodes which are collected independently from the model itself. In principle, "active" or "online" learning training schemes are also possible, which use the model itself to explore the action space and thus construct the training set. In the present context, this would require performing DFT calculations on-the-fly during training.

The interdependence of predictions and targets in eq 15 causes some stability problems when training DQN models.[88] To mitigate this, we use the double deep Q-learning[89] approach, in which two different versions of Q_θ are used during training. The first of these is the *policy network* which is used to make the predictions in the first term of eq 15 and whose weights are updated at every training step. The second is the *target network*, which is used to obtain the Q-values in the target term of eq 15 and whose parameters are synchronized with the policy network in regular intervals. This breaks the direct dependence of prediction and target in the loss function and thus stabilizes training.

Once the training is completed, Q_θ can be used to estimate the long-term reward of any action a given a state s. To construct a generative model based on this, we must finally specify the policy π, that is, the algorithm according to which the next action a is selected. Here, a greedy algorithm which simply selects the action with the highest $Q_\theta(s, a)$ would be possible, but this would obviously not lead to a diverse sample of materials. For a better balance between exploration and exploitation, we therefore sample actions according to probabilities $p(s, a)$, which are obtained from $Q_\theta(s, a)$ with the softmax function

$$p(s, a) = \frac{\exp(\beta Q_\theta(s, a))}{\sum_{a'} \exp(\beta Q_\theta(s, a'))} \quad (16)$$

Here, the sum in the denominator is over all possible actions (including a) and the hyperparameter β behaves like an inverse temperature. These state-action probabilities can thus be tuned from uniform random sampling (for $\beta = 0$) to a fully greedy policy (for $\beta \to \infty$). In practice, we found a value of $\beta = 5$ to be optimal (see Figure S7 in the Supporting Information).

From the hyperparameter search, we obtained a network architecture with five hidden layers with 512 nodes each (with layer normalization[73]). The RL model was trained for 800,000 network updates with a batch size of 250 and a learning rate of 0.00001. Following common practice in the DQN literature, a discount factor $\gamma = 0.999$ is used and the target network is synchronized every 10 steps.

3. RESULTS AND DISCUSSION

3.1. Targeted Generation in a Minority Class. As discussed above, the goal of inverse materials design is to generate promising sample candidates from a large design space. Importantly, these promising candidates are typically exceedingly rare. In the Elpasolite dataset, this challenge can be emulated by attempting the targeted generation of composi-

https://doi.org/10.1021/acs.chemmater.2c01860
Chem. Mater. 2022, 34, 9455−9467

tions in the lowest energy class 1. As shown in Figure 1e, this class is one of the least populated and contains only 86 samples, corresponding to 0.4% of the total training set. This imbalance is equally present in the full Elpasolite space, with only 3757 compositions amounting to 0.2% of all possible ones falling into this *minority class*. For comparison, the neighboring class 2 already amounts to 20,097 compositions (1.0% of the full Elpasolite space).

Figure 4 illustrates the performance of a representative GAN model conditioned on the minority class 1 for the first 250,000

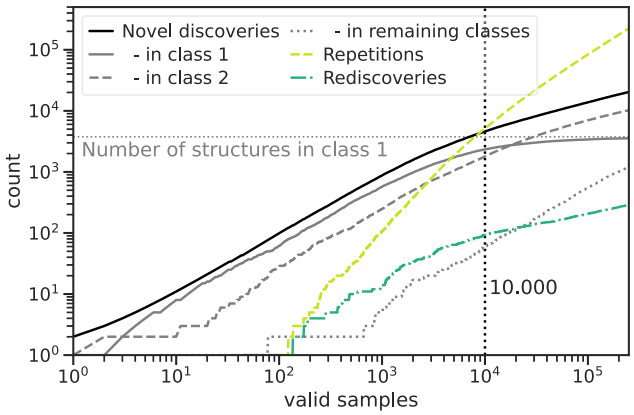

Figure 4. Performance of a representative GAN model for the first 250,000 generated valid samples when conditioned on the minority class 1. Repetitions are previously generated samples. Rediscoveries correspond to known training compositions. Novel discoveries are further discerned by the classes they belong to (in gray).

generated samples. Here, we distinguish between "novel discoveries" (unknown compositions proposed for the first time), "repetitions" (compositions which have previously been generated by this model), and "rediscoveries" (compositions which are part of the training set). The novel discoveries are further discerned according to their class.

This reveals that the model initially displays a high degree of novel discoveries in the target class, which saturates after ca. 10,000 generated samples. At this point, the number of repetitions begins to dominate the generation process, although some novel materials from class 2 are still discovered. Meanwhile, the numbers of rediscoveries and novel discoveries from other classes remain very low. Similar plots can be obtained for the VAE and RL models; see the Supporting Information.

This behavior can be understood from the fact that the generative models essentially learn a conditional probability distribution. When sampling from this distribution, initially mostly unique, high-probability samples are drawn. However, upon continued sampling, there is an increased likelihood that lower-probability samples are generated or that high-probability samples are repeated. This explains the fact that the number of unique class 2 samples eventually overtakes the number of unique class 1 samples. While they are considered to be less probable candidates by the model, there are simply many more unique class 2 compositions to discover in the dataset. Importantly, very few compositions from class 3 and beyond are generated, however, even though these make up the bulk of the Elpasolite composition space. The model thus correctly assigns very low probabilities to these compositions.

For all models generated in this work, the curve for the number of novel discoveries eventually flattens. In other words, the models display a limited capacity for generating unique samples, which is unsurprising since the number of possible Elpasolites is also limited. Notably, the rediscoveries constitute a low share throughout so the model clearly does more than mere training-set memorization. Since repetitions begin to dominate the generation procedure after 10,000 samples, we terminate the generation procedure at this point for the following analyses of minority class generation.

Figure 5 shows the formation energy distributions of the unique compositions produced by representative VAE, GAN,

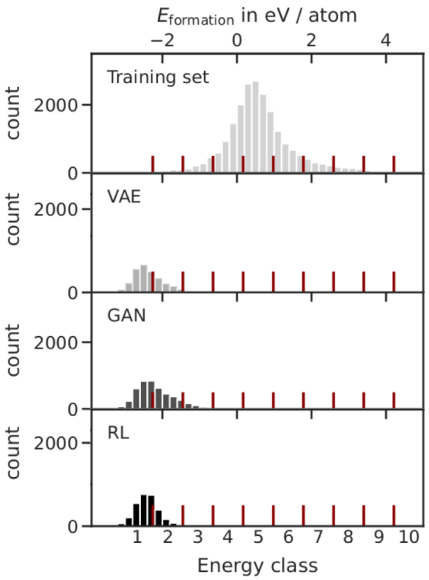

Figure 5. Formation energy distribution (in 0.2 eV/atom bins) of the unique class 1 conditioned compositions proposed by the three generative models (VAE, GAN, and RL) over 10,000 valid samples. Additionally shown is the corresponding distribution over the entire training set of 21,112 compositions.

and RL models. All three models obviously achieve conditional generation in the minority class 1 with great success. Specifically, they produce sample distributions with low formation energies, completely unlike the formation energy distribution of the original training set.

This plot also illustrates from how little class 1 data the models are able to learn. On this scale, the 87 class 1 samples in the training set are not even visible. Nonetheless, all three models generate over 1000 unique new compositions in this class. It can also be seen how the formation energy distributions decay into the neighboring class, generating a negligible amount of samples in higher-energy classes.

For a more quantitative comparison of the generative frameworks considered herein, average performance metrics obtained from 50 model initializations are summarized in Table 1. These metrics confirm the relatively high precision with which all three models generate compositions in the target minority class 1. Given the discrete class boundaries and the larger size of the neighboring class 2, it is not surprising that the generated distributions tail into it. Essentially, all unique samples (>94%) produced by the models therefore jointly fall into these two classes. All three models can thus capture the underlying building principles that lead to stable

https://doi.org/10.1021/acs.chemmater.2c01860
Chem. Mater. 2022, 34, 9455−9467

Table 1. Performance Metrics for the Three Generative Models Conditioned to Generate Minority Class 1 Compositions after 10,000 Valid Samples[a]

	RL	VAE	GAN
precision (right class)	69 ± 8%	83 ± 1%	66 ± 2%
Precision (neigh. class)	30 ± 7%	16 ± 1%	28 ± 1%
coverage (right class)	53 ± 3%	54 ± 2%	62 ± 1%
coverage (neigh. class)	4 ± 1%	5 ± 0%	10 ± 1%
JS distance	0.20 ± 0.03	0.16 ± 0.01	0.16 ± 0.01

[a]Shown are averages over 50 model fits together with the standard deviation.

Elpasolite compositions while covering at least half of the full class 1 composition space.

Notably, both VAE and GAN models display a very low standard deviation for these metrics, indicating that essentially every model fit robustly yields this high precision. There also seems to be a slight trade-off between precision and coverage between VAE and GAN, with the GAN yielding higher coverage but lower precision. In contrast, the RL models display somewhat higher variance.

As indicated by the JS distance, all models accurately reproduce the elemental distribution of the targeted class, with comparatively small values of 0.16 for VAE and GAN and a slightly larger distance of 0.2 for RL. Notably, these distances are actually closer to the target distribution than the training set (0.236, see Figure 2). A more detailed illustration of the elemental distributions is given in Figure 6. A prominent feature of all elemental distributions is the overwhelmingly dominant occupation of site D by fluorine, likely due to its high electronegativity and reactivity. Other sites also exhibit preferences for certain element types, for example, alkali metals and alkaline earth on site C, although this tendency is less pronounced. The generative models thus develop a useful chemical intuition for how to construct stable Elpasolites.

To put these metrics into perspective, simple baseline models based on the prevalence of element combinations in class 1 were also developed (see the Supporting Information). The deep generative models discussed herein display higher coverage and precision by at least a factor of 2, as well as significantly lower JS distances. Since the choice of terminating the generation after 10,000 samples is rather arbitrary, the same analysis was also performed for 3500 samples (see Table S2). This reveals that precision and JS distance are unaffected by the number of samples, whereas (unsurprisingly) the coverage is somewhat lower when fewer samples are generated.

3.2. Targeted Generation in the Majority Class. Complementary to the generation in class 1, we can also consider conditional generation in the majority class 5. This is particularly interesting with respect to the capacity of the generative models. With 907,094 compositions, class 5 spans

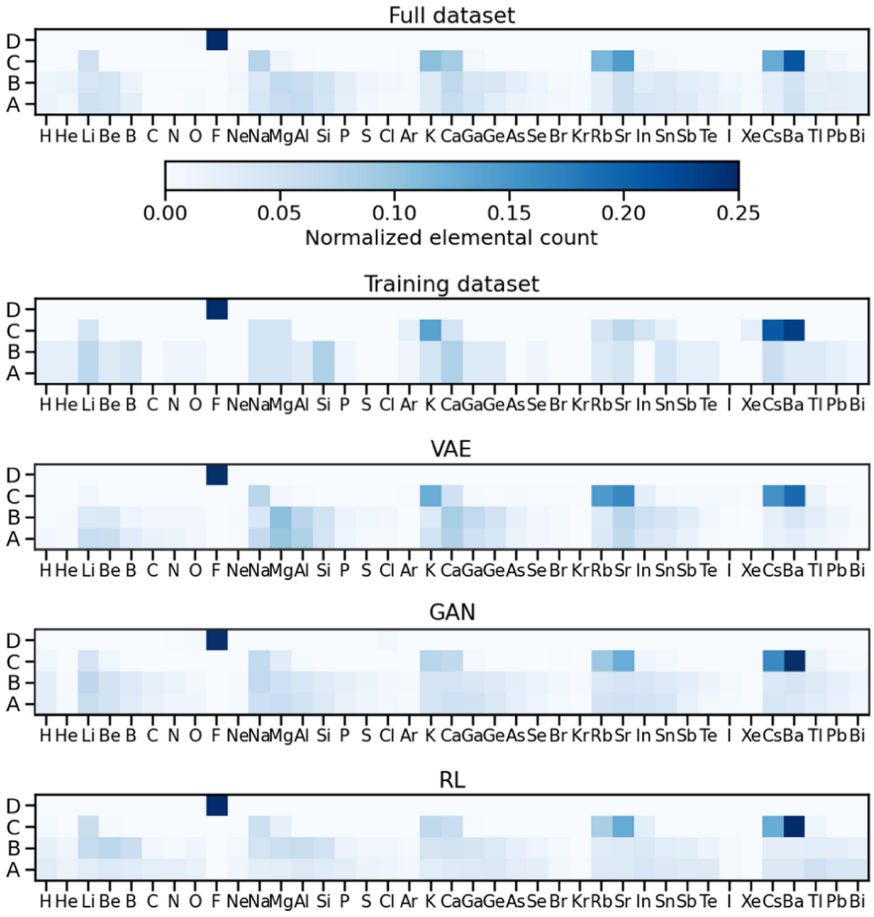

Figure 6. Comparison of the normalized elemental distributions $p(Z|S)$ in class 1 over the four sites (A, B, C, and D) for the full Elpasolite space, the training set, and datasets conditionally generated by the three models (VAE, GAN, and RL). The color scale is chosen to depict the details of the overall distribution. The value of fluorine on lattice site D surpasses its limits, exceeding 0.997 in all cases.

https://doi.org/10.1021/acs.chemmater.2c01860
Chem. Mater. 2022, 34, 9455−9467

46% of the entire Elpasolite composition space and is thus by far the dominant majority class. Taken together, its neighboring classes 4 and 6 account for another 39.9% of the entire Elpasolite design space. The dominance of class 5 is also reflected in the DFT training set, which contains 9650 such compositions, a much larger number than the 86 compositions of class 1. However, compared to the total size of the class 5 composition space, this only amounts to 1%. In relative terms, the coverage of training data in the class 5 composition space is thus even worse than for the minority class 1 (2%, see above).

Analyzing the generation run of a representative GAN model for the majority class (Figure 7) reveals largely analogous

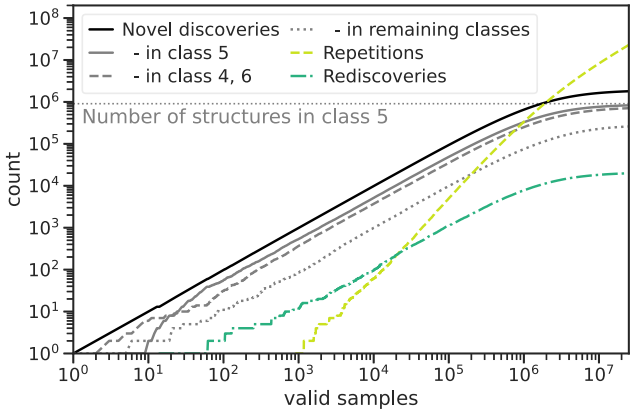

Figure 7. Same as Figure 4, but for a GAN model conditioned on the majority class 5. Note the much larger number of samples required to saturate the number of unique novel discoveries generated, reflecting the much larger composition space covered by class 5.

behavior to the minority class case shown in Figure 4. The rediscovery rate of training examples is again low throughout the run. With continued sampling, the number of repetitions rises steeply, overtaking the novel generations after around 2.5 million samples. The number of novel discoveries is fully converged after 25 million valid samples. Comparable findings are obtained for VAE and RL (see the Supporting Information) so that we evaluate the performance metrics for the majority class after 25 million valid samples in the following.

Table 2 collects the respective metrics. Both GAN and VAE achieve average class coverages of 86% or higher, with precisions between 50 and 60%. In contrast, the RL models achieve significantly higher precision (87% on average) but lower coverages (typically <50%). We observe such trade-offs between precision and coverage frequently, and they should not be strictly attributed to a fundamental difference between the RL and VAE/GAN frameworks. For example, the RL agents could in principle achieve higher coverage at the expense of lower precision by decreasing the inverse temperature β in eq 16. Similarly, different network architectures in the random hyperparameter search form a Pareto front with respect to the number of unique discoveries (coverage) and the JS distance to the training set (precision) (see Figure S4). As above, a similar analysis was performed for a smaller number of generated samples (2.5 million, see Table S3). Again, the precision and JS distance are unaffected by this choice, whereas the coverage decreases.

Table 2. Performance Metrics for the Three Generative Models Conditioned to Generate Majority Class 5 Compositions after 25 Million Valid Samples[a]

	RL	VAE	GAN
precision (right class)	87 ± 7%	58 ± 1%	54 ± 1%
Precision (neigh. classes)	13 ± 7%	34 ± 1%	36 ± 1%
coverage (right class)	44 ± 15%	86 ± 9%	89 ± 2%
coverage (neigh. class)	9 ± 4%	82 ± 11%	85 ± 3%
JS distance	0.49 ± 0.14	0.21 ± 0.01	0.16 ± 0.01

[a]Shown are averages over 50 model fits together with the standard deviation.

We do see fundamental differences between RL and VAE/GAN-based models with respect to the elemental distributions, however. This can be seen from the substantially larger JS distance of the RL-generated data with respect to the target distribution (on average 0.49 for RL vs 0.21/0.16 for VAE/GAN). By analyzing the corresponding elemental distributions in detail (see Figure S3), we find that VAE and GAN sample elements are relatively evenly across the periodic table, in fairly good agreement with the reference data. In contrast, RL models display a much more selective elemental distribution. Indeed, we find that differently initialized RL models converge to different local minima, each with its own characteristic elemental fingerprints. This is also reflected by the fact that RL displays a much higher number of repetitions in the generation process. Overall, this indicates that the distribution learners (GAN and VAE) are better suited for representing large composition spaces than agent-based RL models. However, the latter may also be improved in this respect by using more sophisticated reward functions.

3.3. Influence of Training Data. The generative frameworks discussed herein thus display promising performance for inverse materials design, in particular for minority classes. However, this capability does not come for free as it relies on an extensive training set of labeled compositions (for which DFT calculations are required). The size of this training set amounts to ∼1.0% of the full Elpasolite design space that spans nearly 2 million compositions. At first sight, this seems like impressively little data.

However, it should be noted that in a materials discovery setting additional DFT calculations would be required to verify the formation energies of all unique generated samples. Taking the example of the GAN, this would mean around 4,500 additional calculations, leading to the discovery of 2329 class 1 materials (and 2009 class 2 materials). For comparison, to discover a similar number of class 1 materials through brute-force random screening, would require a factor of 50 more DFT calculations. Since the bulk of the DFT calculations for the generative models is spent on training data generation, decreasing the size of the training sets would thus be an appealing route to further boost the computational efficiency of this approach.

To explore this possibility, we assessed the performance metrics for minority class generation when training with randomly selected subsets of the full training set, keeping all other settings fixed. As in the original training set, we again account for the permutational symmetry of the A and B sites in each subset so that the total number of DFT calculations required for each subset is $\frac{N_{\text{train}}}{2}$. These results are summarized in Figure 8. For comparison, we also include the results for

https://doi.org/10.1021/acs.chemmater.2c01860
Chem. Mater. 2022, 34, 9455−9467

models trained with the original training set reported by Faber et al. (*without* permutational symmetry).

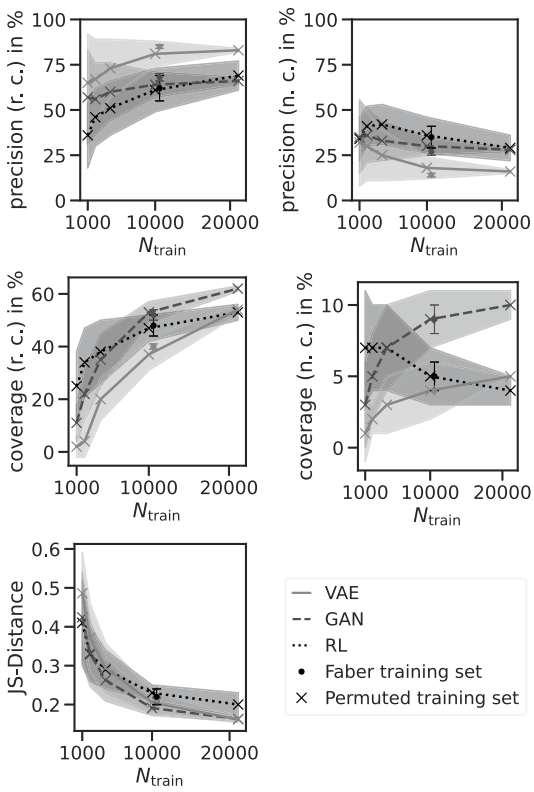

Figure 8. Influence of training set size on the performance metrics of VAE, GAN, and RL models for minority class generation after 10,000 generated samples. Shown are averages over 50 model fits employing 50 different random training subsets. Shaded areas represent the corresponding standard deviations.

This reveals that our data augmentation approach works very well. Models trained on 10,000 data points (including permutations) reach the same performance as models trained on the original set while reducing the number of required DFT calculations by a factor of two. In general, we find that both precision and (particularly) coverage for the target class decrease when the training set decreases. Similarly, the JS distance between generated and target distribution increases. Here, the RL models are somewhat less sensitive, retaining higher coverages for the smallest training sets.

Nonetheless, even reduced training sets yield models capable of discovering a significant number of new materials. Again, taking the GAN as an example, even at the smallest training set size of 1000 compositions, on average, 11% (>410 samples) of all possible class 1 compositions are discovered, easily surpassing the 86 examples found in the original training set. Given a precision of around 50% for this class, this means that roughly 1000 further DFT calculations would be required to obtain the formation energies of all generated samples. With random sampling, finding the same number of class 1 materials would require 220,000 DFT calculations (i.e., a factor of 100 more).

Importantly, these estimates are somewhat conservative. For one, all model hyperparameters were kept fixed, although small datasets often lead to different optimal network architectures. Furthermore, random sampling is a fairly strong baseline in this example due to the limited size of the Elpasolite composition space. In reality, chemical space is practically unlimited and brute-force random search is not a viable strategy at all.

4. CONCLUSIONS

We herein assessed the performance of three deep generative ML frameworks (VAE, GAN, and RL) for the exploration of a large chemical composition space. To this end, we relied on the fully enumerated space of Elpasolite minerals (ABC_2D_6) as a target, which allowed us to quantitatively assess the generative models in terms of precision, coverage, and elemental distributions. In our view, this is highly valuable as evaluating and comparing generative ML models is notoriously difficult.

Despite being built from simple NN architectures, all studied models are capable of reliably generating candidates within the desired formation energy classes. This shows that reasonable model hyperparameters could be determined by an automated procedure while accommodating a reasonable trade-off between coverage and precision in a conditional generation.

Nonetheless, there are a number of notable differences between the approaches. The RL models showed greater robustness toward small datasets but also greater variability between differently initialized models (i.e., a tendency to converge to distinct local minima). In contrast, the VAE and GAN approaches usually produced models that more faithfully reproduced the target elemental distributions, as quantified by the JS-distance.

From a technical perspective, the RL models were trained to generate samples from a given class. We therefore had to train completely new models (with a different reward function) for the majority class generation. In contrast, the VAE and GAN models directly capture class-conditional probability distributions so that a single model can generate all classes. Among these, the VAE showed slightly higher precision and was (subjectively) somewhat easier to train than the GAN. From this perspective, the VAE appears to us to be overall best suited for large-scale materials discovery, although this certainly depends on the application. Indeed, high coverage and faithful reproduction of the target distribution are not always necessary. If the objective is simply to generate a limited number of high-quality samples, a goal-oriented RL model may be the better choice. RL furthermore has the advantage that the reward function can easily be modified to accommodate more complex design targets.

It should be noted that ML-based regression models remain a powerful alternative to generative models for materials discovery, particularly in relatively small design spaces such as the one considered herein. The question of whether a generative or regression model is more appropriate for a given task thus remains interesting. In previous work on organic semiconductors, we found that regression models are not well suited for discovering exceptional materials since these are by definition strongly underrepresented in the training set.[90] The excellent performance of the generative models for minority class generation is highly promising in this context.

We hope that the present work provides a sound basis for the development of deep generative models for materials discovery in chemical composition space. To this end, the establishment of quantitative performance metrics is of paramount importance. In future work, we aim to generalize the current models beyond a single crystal prototype.

https://doi.org/10.1021/acs.chemmater.2c01860
Chem. Mater. 2022, 34, 9455−9467

■ ASSOCIATED CONTENT

Supporting Information

The Supporting Information is available free of charge at https://pubs.acs.org/doi/10.1021/acs.chemmater.2c01860.

Additional generation plots for VAE and RL, elemental distributions for majority class generation, additional details for the hyperparameter search procedure, and GAN generation plots with smaller training sets (PDF)

■ AUTHOR INFORMATION

Corresponding Author

Johannes T. Margraf − *Fritz-Haber-Institut der Max-Planck-Gesellschaft, D-14195 Berlin, Germany;* orcid.org/0000-0002-0862-5289; Email: margraf@fhi.mpg.de

Authors

Hanna Türk − *Fritz-Haber-Institut der Max-Planck-Gesellschaft, D-14195 Berlin, Germany; Chair for Theoretical Chemistry and Catalysis Research Center, Department of Chemistry, Technische Universität München, 85748 Garching, Germany;* orcid.org/0000-0002-9858-7019

Elisabetta Landini − *Fritz-Haber-Institut der Max-Planck-Gesellschaft, D-14195 Berlin, Germany; Chair for Theoretical Chemistry and Catalysis Research Center, Department of Chemistry, Technische Universität München, 85748 Garching, Germany*

Christian Kunkel − *Fritz-Haber-Institut der Max-Planck-Gesellschaft, D-14195 Berlin, Germany*

Karsten Reuter − *Fritz-Haber-Institut der Max-Planck-Gesellschaft, D-14195 Berlin, Germany*

Complete contact information is available at: https://pubs.acs.org/10.1021/acs.chemmater.2c01860

Author Contributions

§H.T., E.L., and C.K. contributed equally.

Funding

Open access funded by Max Planck Society.

Notes

The authors declare no competing financial interest.

■ ACKNOWLEDGMENTS

E.L. and K.R. gratefully acknowledge funding by the Deutsche Forschungsgemeinschaft (DFG, German Research Foundation) under the priority program SPP 2196. H.T. was supported by the DFG under the priority program SPP 2080 DynaKat.

■ REFERENCES

(1) Brock, A.; Donahue, J.; Simonyan, K.Large Scale GAN Training for High Fidelity Natural Image Synthesis. **2019**. arXiv preprint arXiv:1809.11096

(2) Clark, A.; Donahue, J.; Simonyan, K.Adversarial Video Generation on Complex Datasets. **2019**. arXiv preprint arXiv:1907.06571

(3) Nie, W.; Narodytska, N.; Patel, A.RelGAN: Relational Generative Adversarial Networks for Text Generation. *International Conference on Learning Representations*, 2019.

(4) Dong, H.-W.; Hsiao, W.-Y.; Yang, L.-C.; Yang, Y.-H.MuseGAN: Multi-track Sequential Generative Adversarial Networks for Symbolic Music Generation and Accompaniment. *Proceedings of the Annual AAAI Conference on Artificial Intelligence*, 2018.

(5) Merk, D.; Friedrich, L.; Grisoni, F.; Schneider, G. De Novo Design of Bioactive Small Molecules by Artificial Intelligence. *Mol. Inform.* **2018**, *37*, 1700153.

(6) Zhavoronkov, A.; et al. Deep learning e rapid identification of potent DDR1 kinase inhibitors. *Nat. Biotechnol.* **2019**, *37*, 1038−1040.

(7) Sanchez-Lengeling, B.; Aspuru-Guzik, A. Inverse molecular design using machine learning: Generative models for matter engineering. *Science* **2018**, *361*, 360−365.

(8) Elton, D. C.; Boukouvalas, Z.; Fuge, M. D.; Chung, P. W. Deep learning for molecular design-a review of the state of the art. *Mol. Syst. Des. Eng.* **2019**, *4*, 828−849.

(9) Merz, K. M.; De Fabritiis, G.; Wei, G.-W. Generative Models for Molecular Design. *J. Chem. Inf. Model.* **2020**, *60*, 5635−5636.

(10) Arús-Pous, J.; Blaschke, T.; Ulander, S.; Reymond, J.-L.; Chen, H.; Engkvist, O. Exploring the GDB-13 chemical space using deep generative models. *J. Cheminf.* **2019**, *11*, 20.

(11) Brown, N.; Fiscato, M.; Segler, M. H.; Vaucher, A. C. GuacaMol: Benchmarking Models for de Novo Molecular Design. *J. Chem. Inf. Model.* **2019**, *59*, 1096−1108.

(12) Polykovskiy, D.; et al. Molecular Sets (MOSES): A Benchmarking Platform for Molecular Generation Models. *Front. Pharmacol.* **2020**, *11*, 565644.

(13) Zhang, J.; Mercado, R.; Engkvist, O.; Chen, H. Comparative Study of Deep Generative Models on Chemical Space Coverage. *J. Chem. Inf. Model.* **2021**, *61*, 2572−2581.

(14) Flam-Shepherd, D.; Zhu, K.; Aspuru-Guzik, A.Keeping it Simple: Language Models can learn Complex Molecular Distributions. **2021**. arXiv preprint arXiv:2112.03041

(15) Sousa, T.; Correia, J.; Pereira, V.; Rocha, M. Generative Deep Learning for Targeted Compound Design. *J. Chem. Inf. Model.* **2021**, *61*, 5343−5361.

(16) Gupta, A.; Müller, A. T.; Huisman, B. J. H.; Fuchs, J. A.; Schneider, P.; Schneider, G. Generative Recurrent Networks for De Novo Drug Design. *Mol. Inform.* **2018**, *37*, 1700111.

(17) Segler, M. H. S.; Kogej, T.; Tyrchan, C.; Waller, M. P. Generating Focused Molecule Libraries for Drug Discovery with Recurrent Neural Networks. *ACS Cent. Sci.* **2018**, *4*, 120−131.

(18) Amabilino, S.; Pogány, P.; Pickett, S. D.; Green, D. V. S. Guidelines for Recurrent Neural Network Transfer Learning-Based Molecular Generation of Focused Libraries. *J. Chem. Inf. Model.* **2020**, *60*, 5699−5713.

(19) Cai, C.; Wang, S.; Xu, Y.; Zhang, W.; Tang, K.; Ouyang, Q.; Lai, L.; Pei, J. Transfer Learning for Drug Discovery. *J. Med. Chem.* **2020**, *63*, 8683−8694.

(20) Moret, M.; Friedrich, L.; Grisoni, F.; Merk, D.; Schneider, G. Generative molecular design in low data regimes. *Nat. Mach. Intell.* **2020**, *2*, 171−180.

(21) Kang, S.; Cho, K. Conditional Molecular Design with Deep Generative Models. *J. Chem. Inf. Model.* **2019**, *59*, 43−52.

(22) Lim, J.; Hwang, S.-Y.; Moon, S.; Kim, S.; Kim, W. Y. Scaffold-based molecular design with a graph generative model. *Chem. Sci.* **2020**, *11*, 1153−1164.

(23) Li, Y.; Zhang, L.; Liu, Z. Multi-objective de novo drug design with conditional graph generative model. *J. Cheminf.* **2018**, *10*, 33.

(24) Kotsias, P.-C.; Arús-Pous, J.; Chen, H.; Engkvist, O.; Tyrchan, C.; Bjerrum, E. J. Direct steering of de novo molecular generation with descriptor conditional recurrent neural networks. *Nat. Mach. Intell.* **2020**, *2*, 254−265.

(25) Gebauer, N. W. A.; Gastegger, M.; Hessmann, S. S. P.; Müller, K.-R.; Schütt, K. T. Inverse design of 3d molecular structures with conditional generative neural networks. *Nat. Commun.* **2022**, *13*, 973.

(26) Lim, J.; Ryu, S.; Kim, J. W.; Kim, W. Y. Molecular generative model based on conditional variational autoencoder for de novo molecular design. *J. Cheminf.* **2018**, *10*, 31.

(27) Guimaraes, G. L.; Sanchez-Lengeling, B.; Outeiral, C.; Farias, P. L. C.; Aspuru-Guzik, A.Objective-Reinforced Generative Adversarial Networks (ORGAN) for Sequence Generation Models. **2017**. arXiv preprint arXiv:1705.10843

(28) Popova, M.; Isayev, O.; Tropsha, A. Deep reinforcement learning for de novo drug design. *Sci. Adv.* **2018**, *4*, No. eaap7885.
(29) Olivecrona, M.; Blaschke, T.; Engkvist, O.; Chen, H. Molecular de-novo design through deep reinforcement learning. *J. Cheminf.* **2017**, *9*, 48.
(30) Blaschke, T.; Arús-Pous, J.; Chen, H.; Margreitter, C.; Tyrchan, C.; Engkvist, O.; Papadopoulos, K.; Patronov, A. REINVENT 2.0: An AI Tool for de Novo Drug Design. *J. Chem. Inf. Model.* **2020**, *60*, 5918−5922.
(31) Gómez-Bombarelli, R.; Wei, J. N.; Duvenaud, D.; Hernández-Lobato, J. M.; Sánchez-Lengeling, B.; Sheberla, D.; Aguilera-Iparraguirre, J.; Hirzel, T. D.; Adams, R. P.; Aspuru-Guzik, A. Automatic chemical design using a data-driven continuous representation of molecules. *ACS Cent. Sci.* **2018**, *4*, 268−276.
(32) Jin, W.; Barzilay, R.; Jaakkola, T.Junction Tree Variational Autoencoder for Molecular Graph Generation. **2019**. arXiv preprint arXiv:1802.04364
(33) Griffiths, R.-R.; Hernández-Lobato, J. M. Constrained Bayesian optimization for automatic chemical design using variational autoencoders. *Chem. Sci.* **2020**, *11*, 577−586.
(34) Court, C. J.; Yildirim, B.; Jain, A.; Cole, J. M. 3-D inorganic crystal structure generation and property prediction via representation learning. *J. Chem. Inf. Model.* **2020**, *60*, 4518−4535.
(35) Noh, J.; Kim, J.; Stein, H. S.; Sanchez-Lengeling, B.; Gregoire, J. M.; Aspuru-Guzik, A.; Jung, Y. Inverse Design of Solid-State Materials via a Continuous Representation. *Matter* **2019**, *1*, 1370−1384.
(36) Lee, I.-H.; Chang, K. J. Crystal structure prediction in a continuous representative space. *Comput. Mater. Sci.* **2021**, *194*, 110436.
(37) Long, T.; Fortunato, N. M.; Opahle, I.; Zhang, Y.; Samathrakis, I.; Shen, C.; Gutfleisch, O.; Zhang, H. Constrained crystals deep convolutional generative adversarial network for the inverse design of crystal structures. *npj Comput. Mater.* **2021**, *7*, 66.
(38) Kim, S.; Noh, J.; Gu, G. H.; Aspuru-Guzik, A.; Jung, Y. Generative Adversarial Networks for Crystal Structure Prediction. *ACS Cent. Sci.* **2020**, *6*, 1412−1420.
(39) Yao, Z.; Sánchez-Lengeling, B.; Bobbitt, N. S.; Bucior, B. J.; Kumar, S. G. H.; Collins, S. P.; Burns, T.; Woo, T. K.; Farha, O. K.; Snurr, R. Q.; Aspuru-Guzik, A. Inverse design of nanoporous crystalline reticular materials with deep generative models. *Nat. Mach. Intell.* **2021**, *3*, 76−86.
(40) Dong, Y.; Li, D.; Zhang, C.; Wu, C.; Wang, H.; Xin, M.; Cheng, J.; Lin, J. Inverse design of two-dimensional graphene/h-BN hybrids by a regressional and conditional GAN. *Carbon* **2020**, *169*, 9−16.
(41) Dan, Y.; Zhao, Y.; Li, X.; Li, S.; Hu, M.; Hu, J. Generative adversarial networks (GAN) based efficient sampling of chemical composition space for inverse design of inorganic materials. *npj Comput. Mater.* **2020**, *6*, 84.
(42) Pathak, Y.; Juneja, K. S.; Varma, G.; Ehara, M.; Priyakumar, U. D. Deep learning enabled inorganic material generator. *Phys. Chem. Chem. Phys.* **2020**, *22*, 26935−26943.
(43) Zhao, Y.; Al-Fahdi, M.; Hu, M.; Siriwardane, E. M.; Song, Y.; Nasiri, A.; Hu, J. High-Throughput Discovery of Novel Cubic Crystal Materials Using Deep Generative Neural Networks. *Adv. Sci.* **2021**, *8*, 2100566.
(44) Chen, L.; Zhang, W.; Nie, Z.; Li, S.; Pan, F. Generative models for inverse design of inorganic solid materials. *J. Mater. Inf.* **2021**, *1*, 4.
(45) Hoffmann, J.; Maestrati, L.; Sawada, Y.; Tang, J.; Sellier, J. M.; Bengio, Y.Data-driven approach to encoding and decoding 3-d crystal structures. **2019**. arXiv preprint arXiv:1909.00949
(46) Ren, Z.; et al. An invertible crystallographic representation for general inverse design of inorganic crystals with targeted properties. *Matter* **2022**, *5*, 314−335.
(47) Korolev, V.; Mitrofanov, A.; Eliseev, A.; Tkachenko, V. Machine-learning-assisted search for functional materials over extended chemical space. *Mater. Horiz.* **2020**, *7*, 2710−2718.
(48) Nouira, A.; Sokolovska, N.; Crivello, J.-C.CrystalGAN: Learning to Discover Crystallographic Structures with Generative Adversarial Networks. **2019**. arXiv preprint arXiv:1810.11203
(49) Debnath, A.; Krajewski, A. M.; Sun, H.; Lin, S.; Ahn, M.; Li, W.; Priya, S.; Singh, J.; Shang, S.; Beese, A. M., et al.Generative deep learning as a tool for inverse design of high-entropy refractory alloys. **2021**. arXiv preprint arXiv:2108.12019
(50) Sajedian, I.; Badloe, T.; Rho, J. Optimisation of colour generation from dielectric nanostructures using reinforcement learning. *Opt. Express* **2019**, *27*, 5874.
(51) Luo, C.; Ning, S.; Liu, Z.; Zhuang, Z. Interactive inverse design of layered phononic crystals based on reinforcement learning. *Extrem. Mech. Lett.* **2020**, *36*, 100651.
(52) Renz, P.; Van Rompaey, D.; Wegner, J. K.; Hochreiter, S.; Klambauer, G. On failure modes in molecule generation and optimization. *Drug Discovery Today: Technol.* **2019**, *32-33*, 55−63.
(53) Skinnider, M. A.; Stacey, R. G.; Wishart, D. S.; Foster, L. J. Chemical language models enable navigation in sparsely populated chemical space. *Nat. Mach. Intell.* **2021**, *3*, 759−770.
(54) Sawada, Y.; Morikawa, K.; Fujii, M.Study of deep generative models for inorganic chemical compositions. **2019**. arXiv preprint arXiv:1910.11499
(55) Faber, F. A.; Lindmaa, A.; von Lilienfeld, O. A.; Armiento, R. Machine Learning Energies of 2 Million Elpasolite(ABC2D6)Crystals. *Phys. Rev. Lett.* **2016**, *117*, 135502.
(56) Zheng, X.; Zheng, P.; Zheng, L.; Zhang, Y.; Zhang, R. Z. Multi-channel convolutional neural networks for materials properties prediction. *Comput. Mater. Sci.* **2020**, *173*, 109436.
(57) Tshitoyan, V.; Dagdelen, J.; Weston, L.; Dunn, A.; Rong, Z.; Kononova, O.; Persson, K. A.; Ceder, G.; Jain, A. Unsupervised word embeddings capture latent knowledge from materials science literature. *Nature* **2019**, *571*, 95−98.
(58) Huo, H.; Rupp, M.Unified Representation of Molecules and Crystals for Machine Learning. **2017**. arXiv preprint arXiv:1704.06439
(59) Willatt, M. J.; Musil, F.; Ceriotti, M. Feature optimization for atomistic machine learning yields a data-driven construction of the periodic table of the elements. *Phys. Chem. Chem. Phys.* **2018**, *20*, 29661−29668.
(60) Zhou, Q.; Tang, P.; Liu, S.; Pan, J.; Yan, Q.; Zhang, S. C. Learning atoms for materials discovery. *Proc. Natl. Acad. Sci. U.S.A.* **2018**, *115*, E6411−E6417.
(61) Metz, L.; Poole, B.; Pfau, D.; Sohl-Dickstein, J.Unrolled Generative Adversarial Networks. **2017**. arXiv preprint arXiv:1611.02163
(62) Yan, C.; Wang, S.; Yang, J.; Xu, T.; Huang, J.Re-balancing variational autoencoder loss for molecule sequence generation. *Proceedings of the 11th ACM International Conference on Bioinformatics, Computational Biology and Health Informatics*, 2020; pp 1−7.
(63) Lucas, J.; Tucker, G.; Grosse, R. B.; Norouzi, M.*Understanding Posterior Collapse in Generative Latent Variable Models*; DGS@ICLR, 2019.
(64) Maas, A. L.; Hannun, A.; Ng, A.Rectifier Nonlinearities Improve Neural Network Acoustic Models. *Proceedings of the 30th International Conference on Machine Learning*, 2013.
(65) Kingma, D. P.; Ba, J.Adam: A Method for Stochastic Optimization. **2017**. arXiv preprint arXiv:1412.6980
(66) Bergstra, J.; Bengio, Y. Random Search for Hyper-Parameter Optimization. *J. Mach. Learn. Res.* **2012**, *13*, 281−305.
(67) Kingma, D. P.; Welling, M.Auto-encoding variational bayes. **2013**. arXiv preprint arXiv:1312.6114
(68) Rezende, D. J.; Mohamed, S.; Wierstra, D.Stochastic back-propagation and approximate inference in deep generative models. *Proceedings of the 31st International Conference on Machine Learning*, 2014; pp 1278−1286.
(69) Kullback, S.; Leibler, R. A. On information and sufficiency. *Ann. Math. Stat.* **1951**, *22*, 79−86.
(70) Kusner, M. J.; Paige, B.; Hernández-Lobato, J. M.*Grammar Variational Autoencoder. International Conference on Machine Learning*, 2017; pp 1945−1954.

https://doi.org/10.1021/acs.chemmater.2c01860
Chem. Mater. 2022, 34, 9455−9467

(71) Sohn, K.; Lee, H.; Yan, X.Learning Structured Output Representation using Deep Conditional Generative Models. *Advances in Neural Information Processing Systems*, 2015.
(72) Karanasou, P.; Karlapati, S.; Moinet, A.; Joly, A.; Abbas, A.; Slangen, S.; Trueba, J. L.; Drugman, T.A learned conditional prior for the VAE acoustic space of a TTS system. **2021**. arXiv preprint arXiv:2106.10229
(73) Ba, J. L.; Kiros, J. R.; Hinton, G. E.Layer Normalization. **2016**. arXiv preprint arXiv:1607.06450
(74) Goodfellow, I. J.; Pouget-Abadie, J.; Mirza, M.; Xu, B.; Warde-Farley, D.; Ozair, S.; Courville, A.; Bengio, Y.Generative Adversarial Networks. **2014**. arXiv preprint arXiv:1406.2661
(75) Salimans, T.; Goodfellow, I.; Zaremba, W.; Cheung, V.; Radford, A.; Chen, X.Improved Techniques for Training GANs. **2016**. arXiv preprint arXiv:1606.03498
(76) Gui, J.; Sun, Z.; Wen, Y.; Tao, D.; Ye, J.A Review on Generative Adversarial Networks: Algorithms, Theory, and Applications. **2020**. arXiv preprint arXiv:2001.06937
(77) Arjovsky, M.; Chintala, S.; Bottou, L.; Wasserstein GAN. **2017**. arXiv preprint arXiv:1701.07875
(78) Gulrajani, I.; Ahmed, F.; Arjovsky, M.; Dumoulin, V.; Courville, A.Improved Training of Wasserstein GANs. **2017**. arXiv preprint arXiv:1704.00028
(79) Mirza, M.; Osindero, S.Conditional Generative Adversarial Nets. **2014**. arXiv preprint arXiv:1411.1784
(80) Gauthier, J.Conditional generative adversarial nets for convolutional face generation. *Class Project for Stanford CS231N: Convolutional Neural Networks for Visual Recognition, Winter semester*2014; Vol. *2014*, p 2.
(81) Simm, G. N.; Pinsler, R.; Hernández-Lobato, J. M.Reinforcement learning for molecular design guided by quantum mechanics. *37th International Conference on Machine Learning. ICML 2020*, 2020; PartF168147-12, pp 8906−8916.
(82) Blaschke, T.; Engkvist, O.; Bajorath, J.; Chen, H. Memory-assisted reinforcement learning for diverse molecular de novo design. *J. Cheminf.* **2020**, *12*, 68.
(83) Meldgaard, S. A.; Köhler, J.; Mortensen, H. L.; Christiansen, M.-P. V.; Noé, F.; Hammer, B.Generating stable molecules using imitation and reinforcement learning. **2021**. arXiv preprint arXiv:2107.05007
(84) Thiede, L. A.; Krenn, M.Curiosity in exploring chemical space : Intrinsic rewards for deep molecular reinforcement learning. **2020**. arXiv preprint arXiv:2012.11293
(85) Sutton, R.; Barto, A.*Reinforcement Learning: An Introduction*; The MIT Press, 2014.
(86) Mnih, V.; Kavukcuoglu, K.; Silver, D.; Graves, A.; Antonoglou, I.; Wierstra, D.; Riedmiller, M.Playing Atari with Deep Reinforcement Learning. **2013**. arXiv preprint arXiv:1312.5602
(87) Mousavi, S. S.; Schukat, M.; Howley, E. Deep Reinforcement Learning: An Overview. *Lect. Notes Networks Syst.* **2018**, *16*, 426−440.
(88) Hessel, M.; Modayil, J.; Van Hasselt, H.; Schaul, T.; Ostrovski, G.; Dabney, W.; Horgan, D.; Piot, B.; Azar, M.; Silver, D.Rainbow: Combining improvements in deep reinforcement learning. *32nd AAAI Conference on Artificial Intelligence AAAI 2018*, 2018; pp 3215−3222.
(89) Van Hasselt, H.; Guez, A.; Silver, D.Deep reinforcement learning with double Q-Learning. *30th AAAI Conference on Artificial Intelligence AAAI 2016*, 2016; pp 2094−2100.
(90) Chen, K.; Kunkel, C.; Reuter, K.; Margraf, J. T. Reorganization energies of flexible organic molecules as a challenging target for machine learning enhanced virtual screening. *Digi. Discovery* **2022**, *1*, 147−157.

https://doi.org/10.1021/acs.chemmater.2c01860
Chem. Mater. 2022, 34, 9455−9467